A [C II] and [N II] study of the interstellar medium in $z = 4.5$ submillimetre galaxies

Pascale Heather Desmet

Physics

Department of Physics

Lancaster University

August 22, 2024

A thesis submitted to Lancaster University for the degree of Doctor of Philosophy in the Faculty of Science and Technology

Supervised by Dr Julie Wardlow

Abstract

Submillimetre galaxies (SMGs) are an enigmatic population, playing host to some of the highest star formation rates (SFRs) seen in the Universe. They are known to be an important population at their peak around $z \sim 2$ but have a tail out to redshift > 5 where they are more poorly studied. Far-infrared (IR) emission lines are regularly used to study galaxies such as SMGs, with [C II] 158 μm often being used due to its brightness which enables observations at high redshifts. This has lead to its increased use across a range of galaxy types for studies of the interstellar medium (ISM) of galaxies at high redshift. To investigate the properties of high redshift SMGs, and assess the use of [C II] as a tracer of gas and star formation requires additional complimentary data. The [N II] 205 μm line is the ideal candidate to enable more meaning to be deduced from the [C II] line, as it allows the amount of [C II] originating from different regions of the ISM to be determined. In this thesis we present new ALMA observations of 12 SMGs targeting the [C II] 158 μm and [N II] 205 μm emission lines. The data were taken as follow up to untargeted detections from previous studies of SMGs. We write a custom data reduction process for these observations, using CASA to tailor different data products to the varied science goals presented here. We first process the data to optimise recovered flux, implementing a custom region finding algorithm to create extraction regions that account for the disturbed (i.e. non-elliptical) morphologies that are present in some of the SMGs. We detect [C II] and [N II] in six of the targeted galaxies, and one additional source that is within the field of view of the observations, bringing the total to seven. We use these seven galaxies to investigate

the [C II] deficit, a phenomenon whereby galaxies with high IR luminosities have a lower [C II] to far-IR luminosity ratio than expected, based on lower IR luminosity galaxies. There is a moderate deficit in 3–4 of our sources (depending on which relation the deficit is measured from), consistent with other observations of high redshift SMGs. We then assess the amount of [C II] that originates from the ionised ISM vs photodissociation regions (PDRs) using the ratio of the [C II] and [N II] luminosities. The [C II] emission in the $z \sim 4.5$ SMGs is mostly originating from PDRs (70–95% from PDRs) in our galaxies. We find a correlation (Spearman's rank correlation coefficient = 0.64) between the amount of [C II] originating from the ionised ISM and the strength of the [C II] deficit. We use this correlation to calibrate a correction to the observed [C II] luminosity using the [N II] luminosity. This corrects for the effect of the deficit on calculated SFR from the [C II] line. The equation to perform the correction is as follows,

$$[CII]_C = B([CII]_O^2/[NII])^a \quad (1)$$

where $[CII]_C$ is the corrected [C II] luminosity, $[CII]_O$ is the observed [C II] luminosity and [N II] is the observed [N II] 205 μm luminosity. We measure $\log(B) = 1.43 \pm 0.16$ and $a = -0.701 \pm 0.13$, and $\log(B) = 1.49 \pm 0.17$ and $a = -0.719 \pm 0.14$ for two different calibrations of [C II]-SFR. We next use data that has been reprocessed to higher resolution and perform a study of the gas and dust in the same seven sources. We measure [C II] and Band 7 continuum sizes that are consistent with studies of SMGs at lower redshifts, and find that on average the size of the [C II] emission is 1.47 ± 0.13 times larger than the Band 7 continuum, and the [N II] is 1.38 ± 0.27 times larger than Band 7 continuum, supporting theories of the star formation being more compact than the gas in SMGs. We measure values of gas mass fraction and depletion timescales that are consistent with lower redshift SMGs. A kinematic analysis of the [C II] finds four rotating gas disks in our sources. We conclude that the prevalence of rotating gas

disks suggests that the sources are unlikely to be late stage mergers. We provide evidence that $z \sim 4.5$ SMGs are consistent with being the progenitors of $z \sim 2$ massive elliptical galaxies, through their number densities, mass-size relationships and gas depletion timescales.

I dedicate this thesis to my Nana, Irene, the woman in science whose career inspired mine.

Acknowledgements

First of all I would like to thank my supervisor, Julie, for having me as a masters student *and then* agreeing to take me on for my PhD. Thank you for all the late nights in the lead up to proposal deadlines, for your determination to find the best way to support each of your students as an individual and for making this thesis possible. I couldn't have wished for a better supervisor.

The Observational Astrophysics group at Lancaster University has instilled me with a sense of community from my days as an undergraduate attending the 'Meet the Astros' conference during my MPhys year. Starting my PhD during lockdown was difficult but the support and social scene in the group (namely the Teams Christmas parties) made me feel a part of the family regardless. To all the staff, thank you for your kindness and guidance and to my office mates, thank you for your friendship, I will miss working with all of you dearly. A particular shoutout goes to Tom, Heather and Rahul (a.k.a. the Julie crew) for your companionship and shared knowledge in group meetings.

To Louis (Brother), thank you for keeping me grounded to life outside of studies, for reminding me that "physics isn't real" and sending me pictures of whatever cool sea creature you've been observing. They have been welcome breaks to the screaming involved with this process.

I wouldn't be here without my Mum and Dad giving me all the opportunities to pursue my dreams, supporting me to achieve the best I could, dragging me out to lunch at regular intervals, and loving me the whole time. You've made this possible.

To all my friends, both new friends that I've made in Lancaster and and old who've stuck around to see this through, thank you for listening to me complain (especially those of you who are doing your own

PhDs) and for your continued friendship. It means more than I can express.

Finally, to James. You are my best friend, constant supporter, and my love. I owe you more than I can say, and I hope you know that. Thank you for believing in the best in me, for putting up with my research-related meltdowns and for encouraging me to chase my dreams. I can't imagine going through the last four years with anyone else as my partner, and I can't wait to reap the rewards together. I love you.

I also acknowledge funding from STFC and Lancaster University, which has made this thesis possible.

Declaration

This thesis is my own work and no portion of the work referred to in this thesis has been submitted in support of an application for another degree or qualification at this or any other institute of learning.

"When you have eliminated the impossible, whatever remains, however improbable, must be the truth"

— Sir Arthur Conan Doyle (The Sign of the Four, 1890)

Contents

List of Figures

List of Tables

Relevant Publications by the Author

Chapter 2 and 3

- "The origin of [C II] emission from high redshift galaxies: a [C II] and [N II] study of $z \sim 4.5$ submillimetre galaxies"; **Desmet, P** (**in prep.**)

Chapter 2 and 4

- "The resolved properties of [C II]158 μm and [N II]205 μm in $z = 4.5$ submillimetre galaxies"; **Desmet, P** (**in prep.**)

Chapter 1

Introduction

1.1 The Big Bang and composition of the Universe

Our current best model for describing the Universe is the Λ Cold Dark Matter (ΛCDM) model. It exists to describe the contribution of the different components of the Universe to the behaviour and properties of the Universe that we observe at present. Following the Big Bang, where the known Universe began, the Universe has been expanding, evidenced by the correlation between observed recessional velocities of galaxies and their distance from us (Hubble, 1929; Freedman et al., 2001). Recent observations have shown the rate at which the Universe is expanding is accelerating (Riess et al., 1998; Perlmutter et al., 1999; Hinshaw et al., 2013; Planck Collaboration et al., 2020), and so the dark energy component was implemented to explain this acceleration. However, it is the expansion that happened 10^{-36} s after the Big Bang that is influential for the formation of structure in the Universe, and hence galaxy formation. This period, known as 'inflation' caused early quantum fluctuations to expand into the initial density pertubations from which large scale structure forms (Guth, 1981).

The CDM part of the ΛCDM model is cold dark matter. "Cold" dark matter refers the speed at which the particles move, where cold particles move slowly.

Simulations in which dark matter is cold are able to reproduce observations of the density fluctuations across the Universe that exist in the present day (Navarro et al., 1996; Springel et al., 2005). As the Universe continued to expand at a more steady rate following the inflationary period, matter cooled and followed gravity to trace 'nodes' and 'filaments' of dark matter. In these regions of high density, the gravitational collapse of gas occurred, igniting the first stars. These first stars are theorised to be massive and thus short-lived (Bromm et al., 2002).

Regions of high density in the 'nodes' lead to the formation of dark matter haloes. Within these haloes, galaxies form, and their properties change as the Universe progresses. For example, haloes at high redshift have higher accretion and merger rates, meaning that they build up their mass very rapidly. As the Universe progresses and gravity continues to act on each individual halo, their size shrinks and thus their density increases. The properties of a dark matter halo can affect the properties of any galaxy that resides within it (e.g. White & Rees 1978; White & Frenk 1991; Lacey & Cole 1993; Bower et al. 2006; Vogelsberger et al. 2014).

1.2 Galaxies in the local Universe

Galaxies, broadly defined, are a gravitationally bound collection of stars, dust, gas and dark matter, with a central supermassive black hole. While the constituent parts of a galaxy are consistent, the quantities in which each component is present, and the way in which these components are arranged varies greatly, even within the local Universe. When describing galaxies, it is useful to group them into classifications with similar properties. There are different ways of doing this, the most common methods of which are described in this section.

1.2.1 Morphological classifications

The morphology of a galaxy describes its apparent shape in the sky, and these were famously described by Edwin Hubble who classified galaxies in the local Universe into morphological groups based on a number of aspects such as the

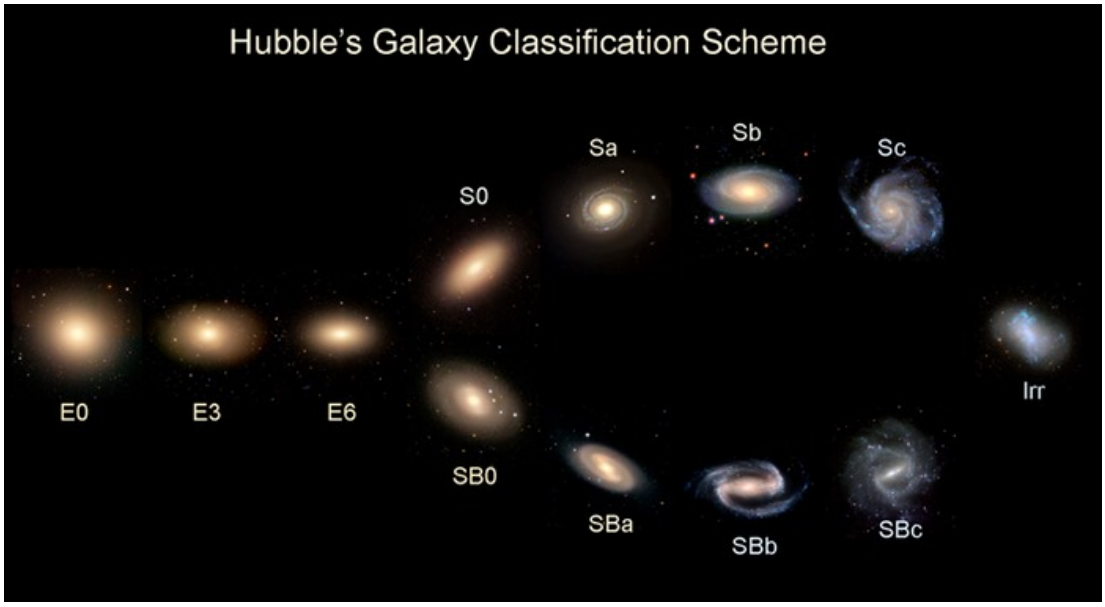

Figure 1.1: The Hubble tuning fork diagram originally devised in (Hubble, 1926). Galaxies on the left are 'early type' ellipticals (E) and are classified based on ellipticity. On the right are 'late type' spirals which are classified based on the presence of bars (SB, lower branch) or not (S, upper branch) and the tightness of the spiralling of their arms. Separating the populations are the lenticular galaxies. Irregular galaxies are those which do not fit into any of the pre-defined categories. Image from https://blog.galaxyzoo.org/2010/05/12/types-of-galaxies/

presence of spiral arms, bars, the tightness of spiralling or lack of any of these features. From this he created the 'tuning fork' diagram (Hubble, 1926), shown in Figure 1.1.

The diagram starts with ellipticals which typically have a red colour and show little structure. These are classified by their ellipticity $e = 1 - b/a$ where b/a is the ratio of the minor to major axis observed for the galaxy, starting with circular E0 ($e = 0$) galaxies on the left and going to the more elliptical galaxies (E9) on the right side of the elliptical segment.

On the right-hand side of the tuning fork are the spirals (S) and barred spirals (SB) which are arranged in order of the tightness of their spiral arms and appear more blue in colour. The spirals and ellipticals are separated in the middle by the lenticular galaxies (S0), which possess both a central bulge and a disk like component, but no spiral arms. The ordering of the tuning fork diagram is what

led to the traditional naming convention of ellipticals being 'early type' galaxies and spirals being 'late types', i.e. ellipticals appearing early in the tuning fork sequence and spirals appearing later. We now know that galaxies begin as disky galaxies and lose their structure over time due to a variety of effects discussed in Section 1.3 (Cole et al., 2000; Bell et al., 2004; Thomas et al., 2005; Bower et al., 2006; Dekel et al., 2009; Martig et al., 2009). This order also explains the observed colour difference as spiral galaxies are usually sites of ongoing star formation and as such host many hot young O and B stars, giving them their blue colour. In contrast, elliptical galaxies host the cooler longer lived stars that have out-survived the O and B's leaving the elliptical galaxies with a redder colour.

The population of stars within a galaxy are not all that contribute to the galaxies perceived colour. For example, the presence of large dust reservoirs can hide the presence of O and B stars when observed at optical wavelengths, artificially causing them to appear red as described in Section 1.5.

Finally, the last category in Figure 1.1 are the irregular galaxies. These are galaxies that don't fit into any of the pre-defined categories described above. They are much more common in the high-redshift Universe, becoming the most populous galaxy type at $z \gtrsim 1.5$ (Willett et al., 2017; Salvador et al., 2024) owing to a lack of ordered rotation having been established at very early times (White & Frenk, 1991; Springel et al., 2005; Ono et al., 2023) and high merger rates until $z \sim 2$. (Conselice, 2014; Shibuya et al., 2024)

Galaxies with disk like structures are generally 'rotation supported' i.e. the ordered rotation of the stars and gas in their spiral arms or disks outweighs the random motion of the stars, or 'velocity dispersion' and this is how they maintain their disk like morphology (Mo et al., 1998; Cappellari et al., 2007). Examples of local rotationally supported spiral galaxies are shown in Figure 1.2.

Galaxies that are 'dispersion dominated' e.g. ellipticals and many irregulars have their morphologies supported by the random motion of gas and stars within them (Cappellari et al., 2007; Martig et al., 2009). Situations such as this can arise following a galaxy merger event for example, which has caused the breakdown of ordered rotation (Cox et al., 2006; Hopkins et al., 2008a) and may then go on to produce a passive (quiescent) elliptical galaxy. This process is discussed further in Section 1.2.2.

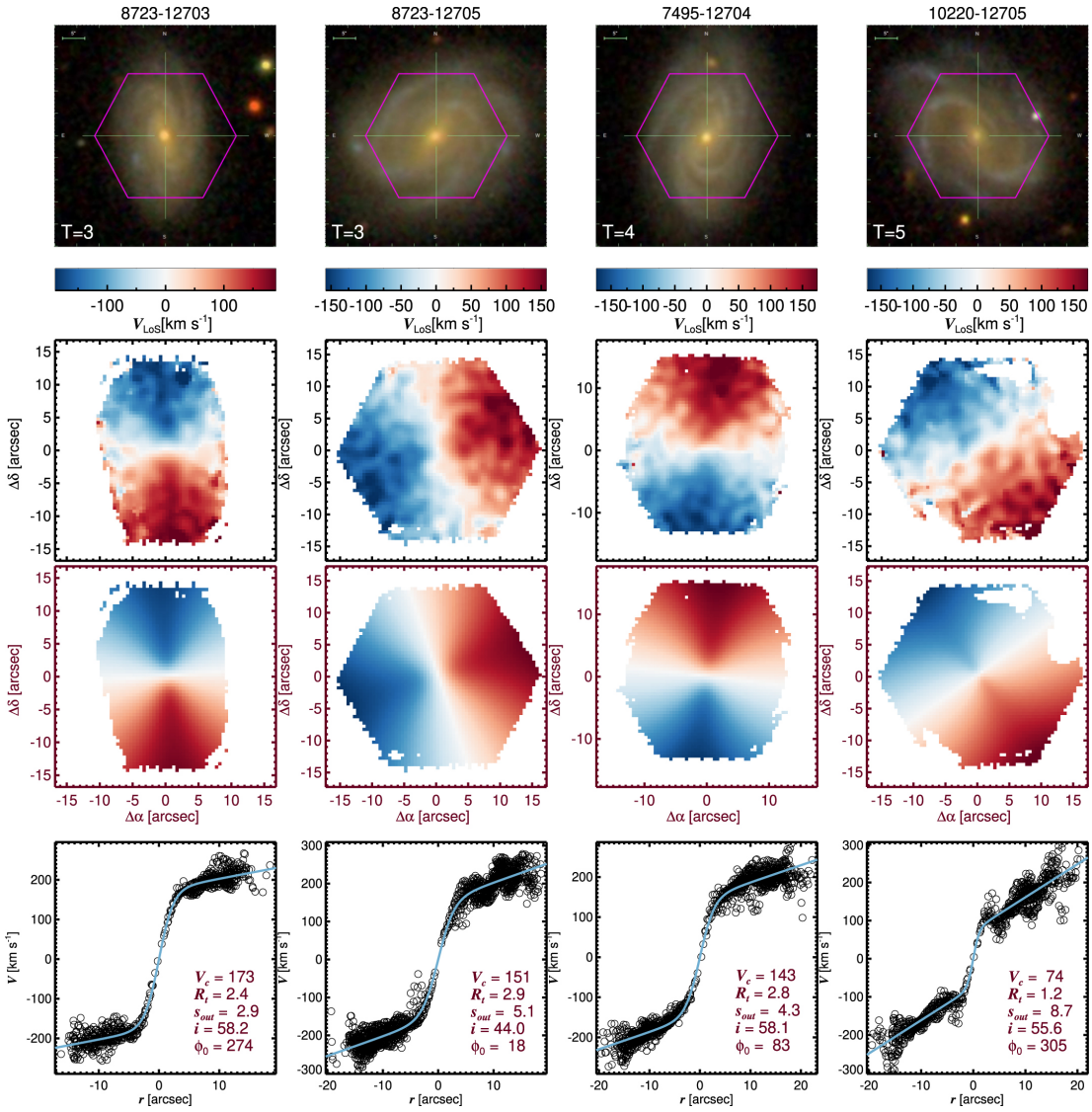

Figure 1.2: Rotation curves of local spiral galaxies observed as part of the MANGA survey (Bundy et al., 2015; Drory et al., 2015; Yan et al., 2016; Wake et al., 2017). The top row shows SDSS colour images overlaid with the integral field unit (IFU; pink hexagon). The second row shows 2D line-of-sight velocity maps. The third row shows the best fit velocity maps to the row two data. The bottom row shows the 1D velocity profiles, with circles showing measurements taken at a distance r from the centre of rotation, and fitted with the solid line (Yoon et al., 2021).

1.2.2 Star formation classifications

Quiescent galaxies are those that are not forming stars. The elliptical galaxies described in Section 1.2 are usually found to be quiescent (Hopkins et al., 2008a; Martig et al., 2009), hence their red colour caused by only containing older cooler stars which have outlived the hotter bluer stars after the cessation of star formation. This is the result of a galaxy using up its gas reservoirs, or otherwise having its star formation quenched (e.g. by gas heating). The transition to quiescence, and methods by which it occurs, are ongoing areas of study (e.g. Valentino et al. 2020; Xie et al. 2024). Quiescence itself is not necessarily permanent, and galaxies are seen to transition into and out of queiscence (Houston et al., 2023).

Under one theory, illustrated in Figure 1.3 (Hopkins et al., 2008a), elliptical galaxies, specifically massive ellipticals in galaxy clusters, are the result of mergers between similarly sized galaxies. The process for this being that when two galaxies coalesce, gas flows into the centre of the galaxy and is compressed, triggering a phase of rapid star formation, as well as feeding the galaxy's central supermassive black hole. Subsequently, feedback from the accreting black hole and supernova winds from the rapid star formation work to eject gas from the galaxies as well as heating it, making it unavailable for continued star formation. Thus, the resulting galaxy becomes quenched, reddens, and a passive early type galaxy remains.

Conversely, starburst galaxies are undergoing a period of extremely rapid star formation. Starburst galaxies have a range of morphologies and are found across a wide range of redshifts (e.g. spiral, irregular Meurer et al. 1995; Calzetti 1997; Ju et al. 2024; Sugahara et al. 2024). They are often defined as having a star formation rate (SFR) to stellar mass (M_*) ratio greater than 4× above the star-formation main sequence, as shown in Figure 1.4 (*bottom*). The definition is somewhat debated since, as Fig. 1.4 shows, there is no clear bimodality in the star forming and star bursting populations, and large variation is seen in the star-forming population alone as galaxies transition to and from a starburst phase (Puglisi et al., 2019).

The trigger for entering into this phase can be one of many (e.g. mergers, disk instabilities, secular gas accretion), depending on the galaxy morphology and the epoch. Triggering mechanisms are discussed further in Section 1.5.

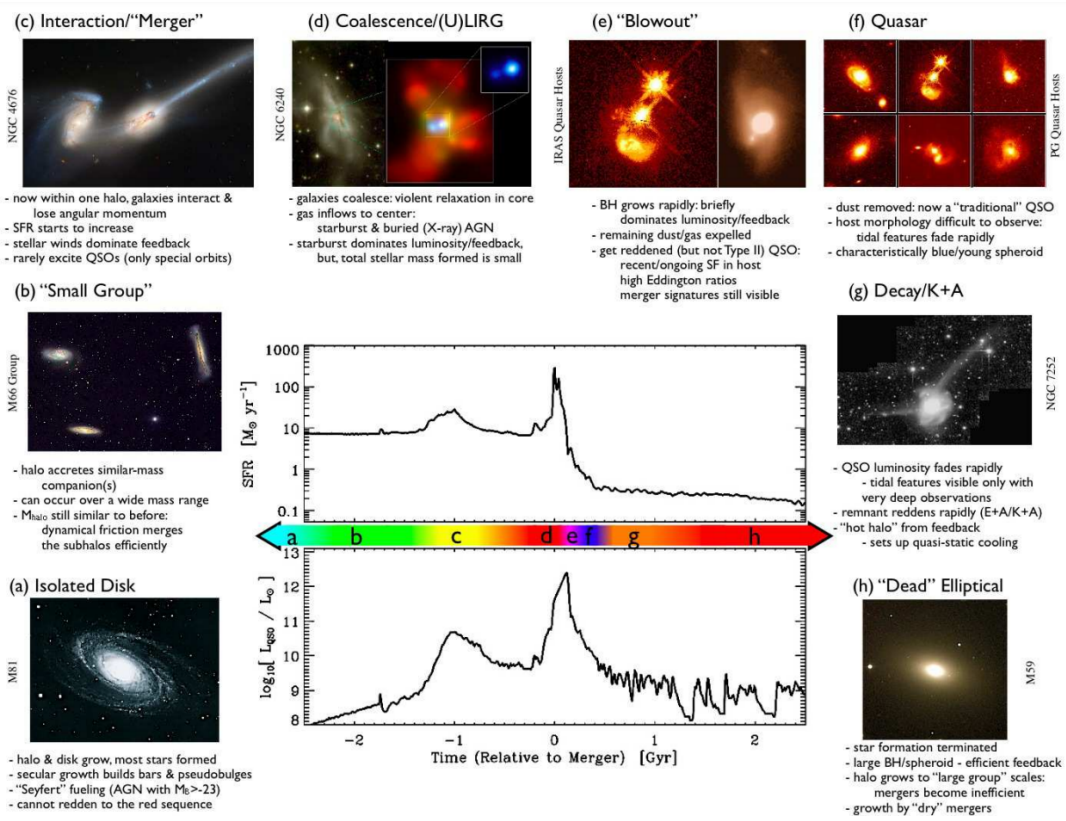

Figure 1.3: Proposed model for elliptical galaxy formation illustrated with how the galaxy might appear at each stage. The central image shows the evolution in the galaxy's SFR (*top*) and luminosity of the central black hole (now a quasar). (*bottom*). From (Hopkins et al., 2008a).

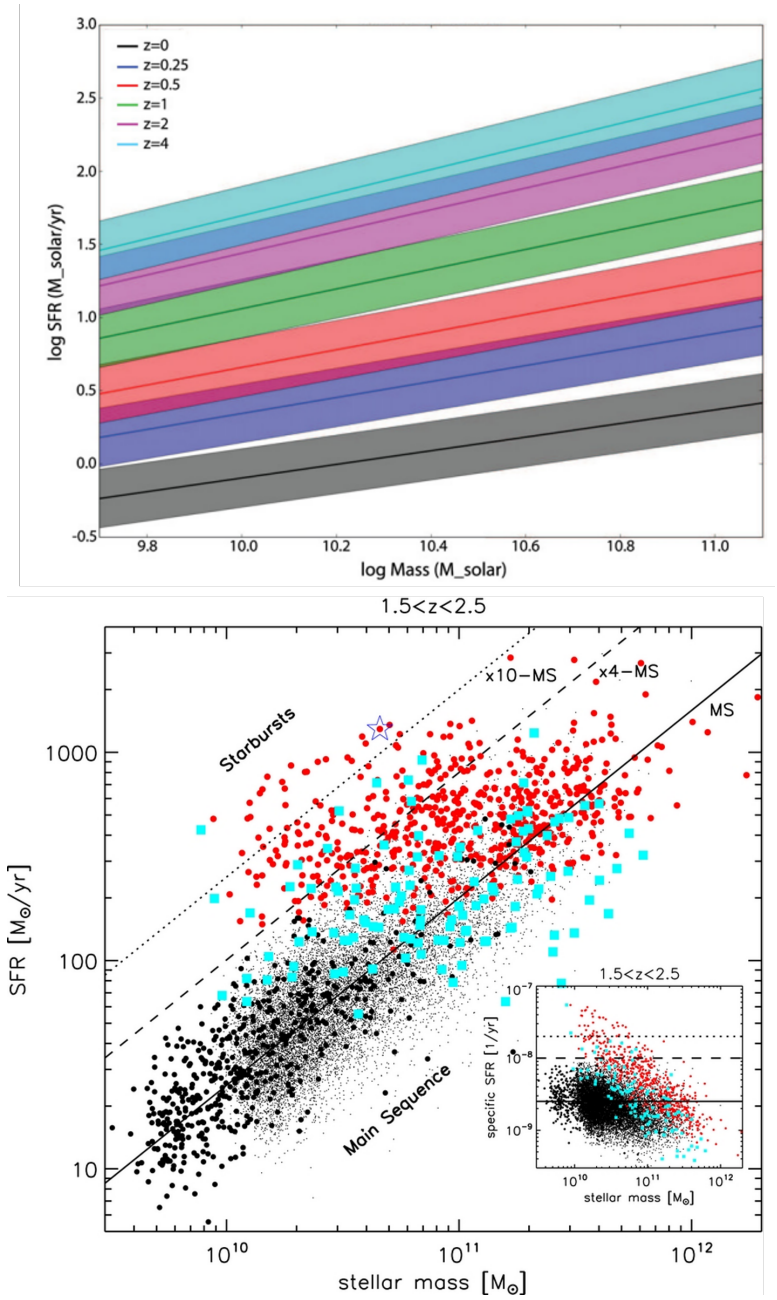

Figure 1.4: *Top:* Evolution of the star-formation main sequence with cosmic time showing that at earlier epochs, 'normal' galaxies were more active than at present times (Speagle et al., 2014). *Bottom:* Example of the distribution of galaxies on the star formation main sequence at $1.5 < z < 2.5$ showing the smooth transition between star forming and starbursting populations (Rodighiero et al., 2011).

1.3 Galaxy evolution

It is well observed that galaxies in the early Universe do not exhibit the same ordered structures that exist locally. Indeed, observations of early galaxies show that they are 'clumpy' with clouds of gas and patches of star formation seemingly randomly located within a galaxy (Springel et al., 2005; Ono et al., 2023; Salvador et al., 2024). The journey that galaxies take from these primordial objects to the structures we see reflected in the Hubble tuning fork is what the field of galaxy evolution aims to piece together. Outside of the local Universe, the Hubble tuning fork becomes less relevant, as we know that the classification of a galaxy involves more than just its morphology. Properties of galaxies vary greatly within a single morphological classification (e.g. quenched spirals Cui et al. 2024). The composition and activity of a galaxy is often more informative than its apparent shape. As such, in this Section we will explore how various aspects of galaxies evolve over the course of the Universe and what this can tell us about the general evolutionary path of galaxies from the early to the local Universe.

1.3.1 Evolution of the cosmic star formation rate density

As seen in Section 1.2 different galaxy types are host to different populations of stars affecting their apparent colour. The presence of the hot O and B stars, usually seen in late type galaxies is indicative of ongoing star formation, since they have short lifetimes. The star formation rate (SFR) is a measure of how rapidly a galaxy is forming stars and is affected by a number of factors from both the galaxy's environment and its internal properties, such as its central supermassive black hole (e.g. Lemaux et al. 2014).

The cosmic star formation rate density (SFRD) quantifies the history of star formation across the whole Universe. Measuring the SFRD as a function of cosmic time provides insight into when the majority of the stellar mass in the Universe was created (Madau et al., 1998; Santini et al., 2009; Madau & Dickinson, 2014). Figure 1.5 shows the variation of SFRD with cosmic time (Madau & Dickinson, 2014).

SFR can be measured in a number of ways. The first is by directly observing the stellar light via UV and optical light. For this method, it is ideal to observe galaxies in the UV at 1500 Å as it efficiently selects for galaxies in which star formation is ongoing (within the last 100 Myr) (Conroy et al., 2009). This is due UV light being produced primarily by O type stars. It is also less sensitive to dust attenuation than at shorter wavelengths. This UV luminosity can be converted to SFR using a conversion factor which will be sensitive to the choice of initial mass function (IMF), the metallicity of the stars (Z) and recent star formation history of the galaxy (Kennicutt, 1998; Conroy et al., 2009; Madau & Dickinson, 2014).

Infrared emission can also be used to measure SFR, and is interpreted as the UV and optical light emitted by O and B stars that has been absorbed by dust within the galaxy. Dust is produced in supernovae (SNe), and so where star formation is ongoing and rapid, so too are the occurance of SNe explosions leading to a rapid build-up of dust in star-forming systems. This dust is consequently heated and re-emits the radiation thermally, which is observed in the IR and submillimetre regime. The total infrared luminosity ($L_{\rm IR}$, defined as the integrated luminosity between 8–1000 μm) can then be converted to an SFR via a calibration e.g. Kennicutt (1998), assuming star formation is ongoing and there is no contribution to the IR flux by active galactic nuclei (AGN). In order to measure the $L_{\rm IR}$ a model mist be fitted to photometric points distributed across the 8–1000 μm range. The dust is typically modelled by a modified black-body for which the dust temperature and slopes on both sides of the dust peak can be controlled, but templates are also used where little photometric data is available. The SFR calculated will be sensitive to the choice of model used to fit the modified black body curve created by dust emission, and specifically the temperature of the dust which determines the peak wavelength of the black body curve.

Finally, UV/optical or far-IR emission lines such as Lyα, Hα, [N II] and [O III] which are emitted from the regions of ionised gas surrounding hot young stars can be observed and converted to an SFR via conversion factors which are calibrated from observed sources with known SFRs, usually calculated by one of the above methods (e.g. Calzetti 2013; Ramos Padilla et al. 2023).

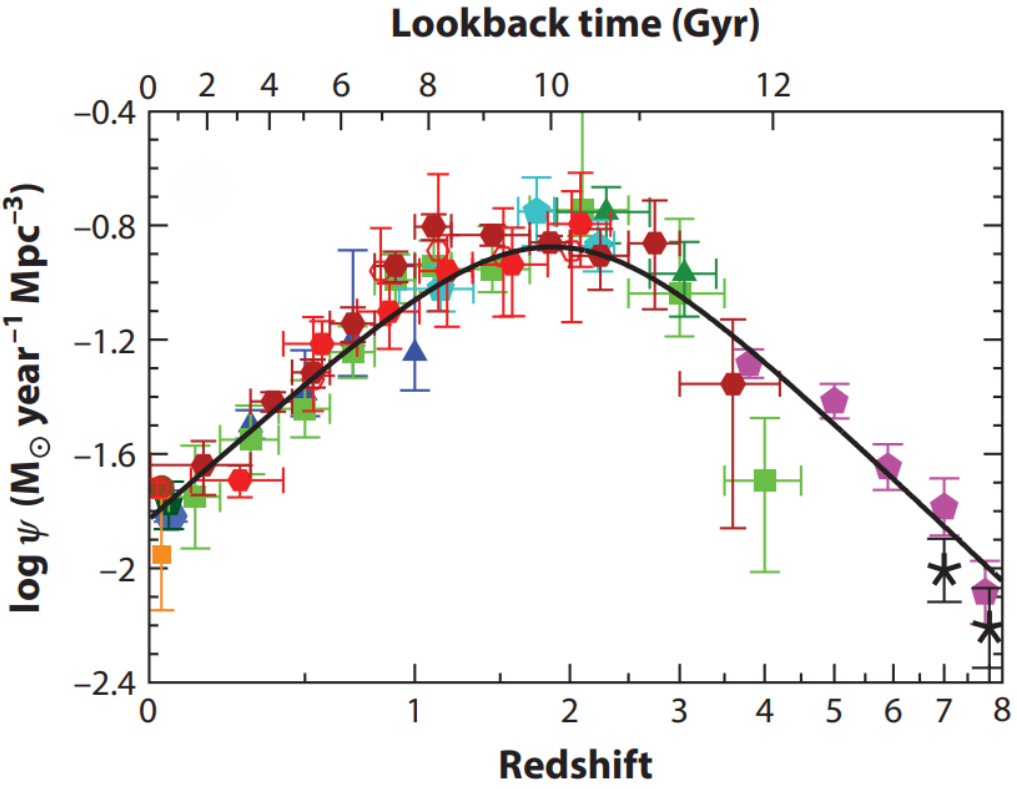

Figure 1.5: Cosmic star formation rate density throughout the Universe from Madau & Dickinson (2014) The green, blue, cyan and magenta points are measurements from the UV, while the points in orange, red and brown measured from IR luminosities.

The SFRD is observed to rise steadily from the beginning of the Universe to a peak at $z \sim 1-3$ after which it falls exponentially (Figure 1.5; Madau & Dickinson 2014). The period at which the SFRD peaks is known as 'cosmic noon'. The existence of an evolving SFRD triggers a number of questions about the Universe, including why star formation peaked at cosmic noon.

The observed trends on a Universal scale are a result of the behaviour of individual galaxies changing across populations at each epoch. In order for the star formation to be increasing from early times, gas within a galaxy must be replenished at a rate at least equal to the rate of star formation within galaxies plus the rate at which gas is removed from a galaxy by e.g. SN winds.

There are multiple methods proposed which can achieve this, for example 'supershells' are the result of gas being shock heated and compressed by SN explosions and stellar winds. Theories suggest that the surface of a supershell is efficient at cooling gas, and that the compression of gas that they cause can fuel star formation in new areas of the galaxy, on timescales comparable to the lifespan of a supershell (Hopkins et al., 2008b; Ntormousi et al., 2011).

An alternate and more widespread theory is one of accretion of gas from the intergalactic medium (IGM; Kereš et al. 2005; Melso et al. 2019; Li et al. 2023) which is explained fully in Section 1.3.2. Results of observations show that the rate of gas accretion onto galaxies is enough to sustain star formation at least in the range $0 < z < 2$ (Schaye et al., 2010).

The shape of the SFRD at early times is constrained by the buildup of massive haloes i.e. at early times, smaller galaxies dominate the SFRD but at later times with the rising merger fractions (Conselice et al., 2008; Hopkins et al., 2008a) allow for the buildup of bigger and richer haloes (Vogelsberger et al., 2014; Rafieferantsoa et al., 2015). Contributions from massive galaxies become dominant around cosmic noon where the SFRD peaks (Schaye et al., 2010; Vogelsberger et al., 2014).

Alongside the growth of SFR and mass in a galaxy, the central black hole is also seen to grow at a comparable rate, leading to theories of co-evolution between the black hole and its host galaxy (Granato et al., 2004; Croton et al., 2006; Kormendy & Ho, 2013; Lemaux et al., 2014). At times when the galaxy is rapidly accreting mass, it is often undergoing periods of intense star formation

(explored further in Section 1.3.2) and the central black hole is also able to rapidly accrete mass, becoming an AGN (e.g. Figure 1.3; Hopkins et al. 2008a). It is at this point that powerful jets are formed which are able to expel gas from galaxies. AGN are also able to heat gas through the intense X-ray radiation they produce. Both the kinetic (jets) and radiative (X-rays) modes of feedback are able to remove gas from the reservoir available for star formation, either by physically removing it from the galaxy or by heating it. Jets such as these often need to be invoked in models in order to reproduce the rapid quenching of star formation that is seen at $z < 1$. The combination of feedback from AGN, supernovae and increased gas consumption by star formation is theorised to cause the downturn in star formation activity observed in the local Universe (Heckman et al., 1990; Schaye et al., 2010; Lemaux et al., 2014; Vogelsberger et al., 2014; Perrotta et al., 2023).

1.3.2 Gas evolution

Cold gas is the fuel for star formation. The gas within a galaxy is in constant flux, heating and cooling, becoming ionised and recombining, inflowing and outflowing. Gas can be introduced to a galaxy by smooth accretion from the surrounding intergalactic medium (IGM) and via mergers with other galaxies. This cycle of gas flow in a galaxy and the different spatial scales affected are shown in Figure 1.6 (Walter et al., 2020). Conversely, gas can be lost through accretion into active galactic neuclei, or expulsion through jets from AGN or powerful winds from supernovae. Gas can also be heated by intense radiation fields from AGN and young stars, disabling it from forming new stars (Heckman et al., 1990; Croton et al., 2006; Perrotta et al., 2023). Thus having enough gas available for star formation (both physically present and cool enough to collapse) is the result of an equilibrium between these processes.

Figure 1.7 shows how the mass density of different gas phases associated with a galaxy change through cosmic time (Walter et al., 2020). The simple hypothesis painted by Figure 1.7 and detailed in Walter et al. (2020), is that for a secularly evolving galaxy, cool gas flows into a galaxy from the IGM and circumgalactic medium (CGM). Thus, the initially high amount of atomic hydrogen (H I) within

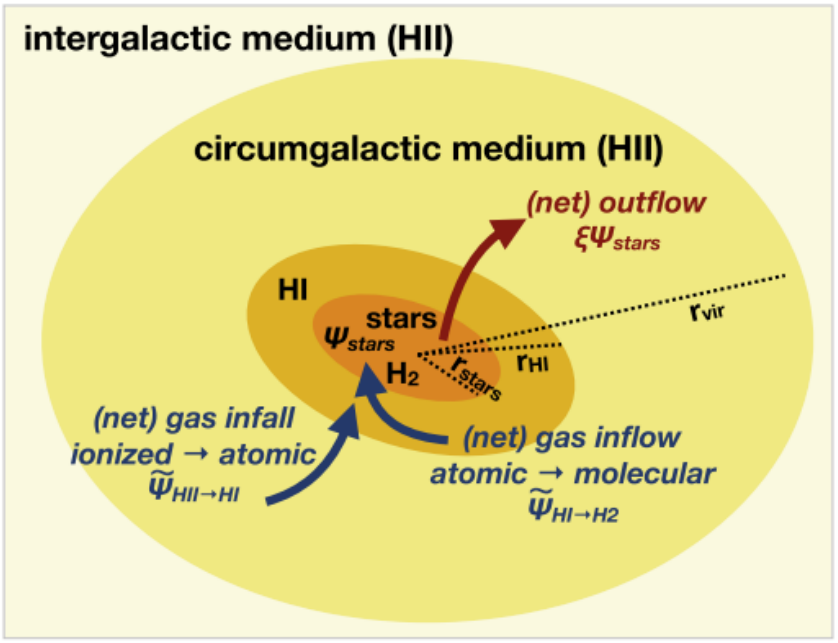

Figure 1.6: Schematic showing the different areas in and around a galaxy which are involved with the baryon cycle with inflows and outflows of gas between these areas indicated. (Walter et al., 2020)

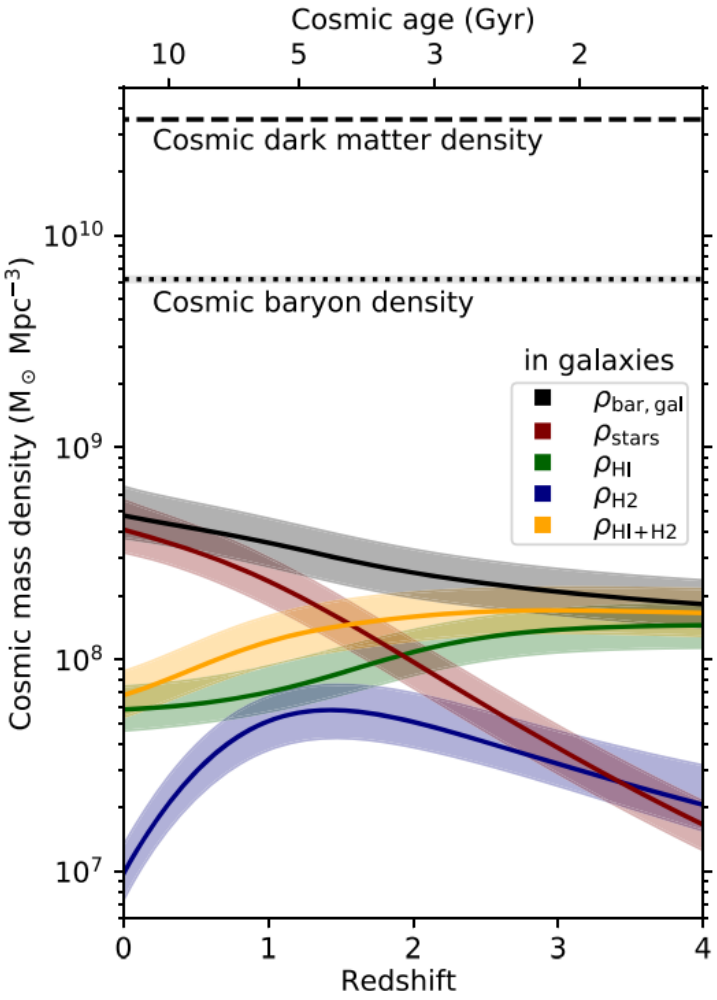

Figure 1.7: The variation of the mass density of different components in and around a secularly evolving galaxy with cosmic time, where the blue line represents molecular hydrogen, green is atomic hydrogen, yellow is the sum of the molecular and atomic hydrogen, red is the stellar mass and black is the total baryonic mass in the galaxy. The dotted line shows the total baryon density for the galaxy, with the large discrepancy between it and the black line being due to a large portion of the baryon mass existing outside the galaxy in the IGM and CGM. The dashed line shows the dark matter density for the galaxy. (Walter et al., 2020)

the galaxy flows inwards building up the molecular hydrogen (H_2) reservoir and itself being replenished by ionised hydrogen (H II) from the CGM. As the H_2 mass builds up, so then star formation rate follows, given by the mirrored shapes of the H_2 curve in Figure 1.7 and the SFRD in Figure 1.5. Then, as star formation peaks at $z \sim 2$ and supernova explosions become more prevalent, some molecular gas becomes ionised by the strong UV fields produced by O and B stars, some gas is expelled back to the CGM and some is accreted by AGN (which grow alongside the stellar mass of the galaxy) (e.g. Granato et al. 2004; Croton et al. 2006; Kormendy & Ho 2013) causing the decline in the H_2 mass density and thus the SFRD. There is, however, no one size fits all approach to the onset and cessation of star formation within any particular galaxy. Factors such as the strength of SN winds and AGN jets vary and have been seen to both enhance and suppress star formation depending on how they are modelled (discussed in Section 1.3.1). Additionally, interactions between galaxies can disrupt the baryon cycle described here, having profound effects on the fate of the galaxy (Cox et al., 2006; Hopkins et al., 2013; Rafieferantsoa et al., 2015).

1.3.3 The star-formation main sequence

For star-forming galaxies, a strong correlation between their SFR and stellar mass (M_*) has been observed (e.g. Brinchmann et al. 2004; Daddi et al. 2007; Speagle et al. 2014). This relationship is known as the 'star-formation main sequence' as shown in Figure 1.4 and is of the form

$$\log(\mathrm{SFR}) = \alpha \log(M_*) + \beta \tag{1.1}$$

where α and β are free parameters. The relationship is tight with scatter of ~ 0.2 dex; (Speagle et al., 2014) and spans $\sim 4-5$ orders of magnitude of mass (Santini et al., 2009). Some studies define 'normal' star forming galaxies as those that lie on the main sequence at a given epoch.

Correlations exist between other galaxy properties and distance from the main sequence, with galaxies lying close to the relation displaying exponential disk like morphologies (Wuyts et al., 2011) and having higher gas fractions than those that

lie below it (Tacconi et al., 2013). Additionally, elliptical and lenticular galaxies tend to fall below the main sequence (González Delgado et al., 2016) along with galaxies with a larger black hole mass (Davé et al., 2019).

In galaxies that are spatially resolved, the radial averages can be placed on the main sequence to assess star formation activity within different regions of a galaxy. This analysis shows that in disky galaxies the central regions are less star forming than the disks (González Delgado et al., 2016), providing evidence for 'inside out' quenching where the surpression of star formation is linked to the growth of a galaxy's central bulge and star formation becomes quenched in these regions first (e.g. Perez et al. 2013; Sánchez et al. 2014; González Delgado et al. 2016).

The main sequence itself evolves out to at least $z \sim 4$ (Karim et al., 2011; Speagle et al., 2014) as shown in Figure 1.4. The increasing normalisation of the main sequence at increasing redshifts (i.e. increasing β in Equation 1.1) indicates that 'normal' galaxies at higher redshifts have higher SFRs than galaxies of the same mass that are observed locally (Speagle et al., 2014). An evolving star formation main sequence has implications for the definitions of galaxies that do not conform to the SF main sequence. For example, starburst galaxies are defined as being $> 4\times$ higher than the main sequence as described in Section 1.2.2 (Rodighiero et al., 2011) and so become even more extreme in the early Universe.

1.3.4 Mass, SFR and Luminosity Functions

Another way of tracking the general properties of galaxies across the Universe is by measuring the number density of galaxies in bins of various properties. i.e. the number density of galaxies with certain masses, star formation rates or luminosities, these are known as mass, SFR and luminosity functions, respectively (e.g. Gallego et al., 1995; Dunne et al., 2000; Jenkins et al., 2001; Faber et al., 2007) By fitting these observations and modelling them in simulations we are able to predict how many galaxies of a certain type we expect to see at any given point in the Universe and identify trends. Alternatively we can study observational trends directly. Each function is plotted and fit at a given redshift and the parameters describing it may change with redshift. Functions such as

this are usually described by a Schechter function (Schechter, 1976) which have three parameters describing the slope at the faint or low mass end (α), the point at which the turnover occurs between the two slopes (L^*, M^* or equivalent), known as the 'knee' and the normalisation (Φ^*). Equation 1.2 shows an example of the Schechter function set up to measure a luminosity function, where L is the observed luminosity.

$$\Phi \, \mathrm{d}L = \left(\frac{\Phi^*}{L^*}\right) \left(\frac{L}{L^*}\right)^{\alpha} e^{-\frac{L}{L^*}} \mathrm{d}L \tag{1.2}$$

If we take for example an SFR function and assume it to follow the evolutionary path seen in Figure 1.5, then the integral under the SFR function measured at redshift ~ 2 would be larger than one measured at redshifts $\ll 2$ or $\gg 2$ indicating that at redshift ~ 2 there is a greater density of galaxies with high SFRs compared to other points in the Universe before or after that (e.g. Sobral et al., 2014). Thus differences in these Schechter functions can be indicative of an evolution of that property throughout the Universe, but it is important to be aware that this evolution is not always linear.

1.4 Observing the ISM

Observing and tracing the state of the gas, dust and stars within a galaxy is essential to understanding the star formation occurring within it. In some cases (e.g. IR observations of dust) we can directly observe components of the interstellar medium (ISM). However, other components can be more difficult to observe directly, with the availability of observational tools changing with source redshift. As such, numerous 'tracers' have been identified from which we infer the presence of other components. These accompany observational techniques that allow us to have a fuller picture of the ISM of any galaxy while being observationally efficient.

1.4.1 Photometry and SEDs

As established in Section 1.3.1 observing galaxies at different wavelengths targets different components of a galaxy, e.g. UV and optical light generally tracing the

stars and IR tracing dust. Each measurement in isolation can be combined with scaling relations to try to deduce more about the galaxy, but this is often subject to assumptions and systematics from the calibration of the relation. Ideally when observing a galaxy, photometric measurements are taken across the whole electromagnetic spectrum from which a spectral energy distribution (SED) can be fit. This is a measure of the galaxies flux as a function of wavelength (or frequency).

A galaxy's SED is dependent on a variety of factors; its star formation history (SFH), initial mass function (IMF), star formation rate, dust content (and temperature), AGN presence etc. (e.g. Conroy 2013). In order to extract these properties from an SED it is often easiest to work in reverse. For example, MAGPHYS (da Cunha et al., 2015) works by creating a table of SEDs based off a set of galaxy parameter combinations. It then finds the best fit SED to the provided observed photometry and reports back the galaxy properties that went into producing the best fit SED, as the observed galaxy is likely to have similar properties. In this way, many more galaxy properties can be derived than from any one photometric measurement in isolation.

Care must be taken, however, as different SED fitting codes are optimised for either different parts of the electromagnetic spectrum or certain galaxy types. MAGPHYS, for example, does not account for an AGN component and so will not take this into consideration when presenting galaxy properties. As such careful consideration is needed to understand the implicit biases of the fitting code before attempting to fit an SED.

1.4.2 Gas tracers

Ionised hydrogen can be observed directly in dust-free galaxies via emission lines caused by electrons transitioning between different energy levels, such as the Hα line (mentioned in Section 1.3.1). The challenge with Hα is that it is sensitive to dust attenuation and is prone to underpredicting the gas mass and SFR when not corrected for dust (Kewley et al., 2002; Kennicutt & Evans, 2012). Other optical tracers of ionised gas include Hβ and the [N II] 6585 μm, [S II] 6716 μm and [O III] 5007 μm optical doublets. These lines are useful beyond their being

a tracer of ionised gas as their flux ratios can indicate the presence of AGN via a Baldwin, Terlevich and Philips (BPT; Baldwin et al. 1981) diagram. In galaxies where dust is present, it is possible to correct optical and UV lines for dust attenuation, but this requires measurements of Hα/Hβ and is sensitive to models of dust attenuation (e.g. Calzetti et al. 2000). Alternatively, ionised gas tracers that are not affected by attenuation can be helpful. These include the far-IR lines [N II] 122 μm and 205 μm, [O III] 88 μm and 52 μm (e.g. Hodge & da Cunha 2020; Ramos Padilla et al. 2023).

Atomic and neutral hydrogen are harder to observe, with the only available line to directly observe atomic hydrogen being the 21 cm line, a result of the electron changing its spin state. Neutral hydrogen only occurs away from sites of ionising radiation and is not observed directly, instead we use gas tracers to infer its presence. These include molecules such as carbon-monoxide (CO) which is the most widely used tracer of molecular gas (e.g. Carilli & Walter 2013). [C II] 158 μm has been used increasingly as a tracer of molecular gas and SFR (e.g. De Looze et al. 2014; Carniani et al. 2020; Harikane et al. 2020; Schaerer et al. 2020; Mitsuhashi et al. 2021) but its complex nature must be carefully accounted for during analysis, explored further in Section 1.4.3 and Chapter 3.

Far-infrared observations are also now increasingly being used to study other high-redshift galaxy populations, particularly those selected at optical and near-infrared wavelengths, such as Lyman break galaxies (LBGs) (e.g. Maiolino et al. 2015; Smit et al. 2018; Hashimoto et al. 2019; Bowler et al. 2022; Fudamoto et al. 2022; Fujimoto et al. 2024). Understanding the limitations of such data, and the similarities and differences between high-redshift populations selected in the far-infrared/submillimetre and at shorter wavelengths is important for interpreting the observations and comparing derived physical parameters with galaxy evolution models (e.g. Shen et al. 2022; Lower et al. 2024).

1.4.3 [C II] 158 μm

The bright [C II] 158 μm line is the main ISM cooling line and it can emit up to 1% of a galaxy's far-infrared luminosity (e.g. Stacey et al. 1991; Brauher et al. 2008; Graciá-Carpio et al. 2011). For galaxies at $z \gtrsim 4$ [C II] is redshifted into ALMA

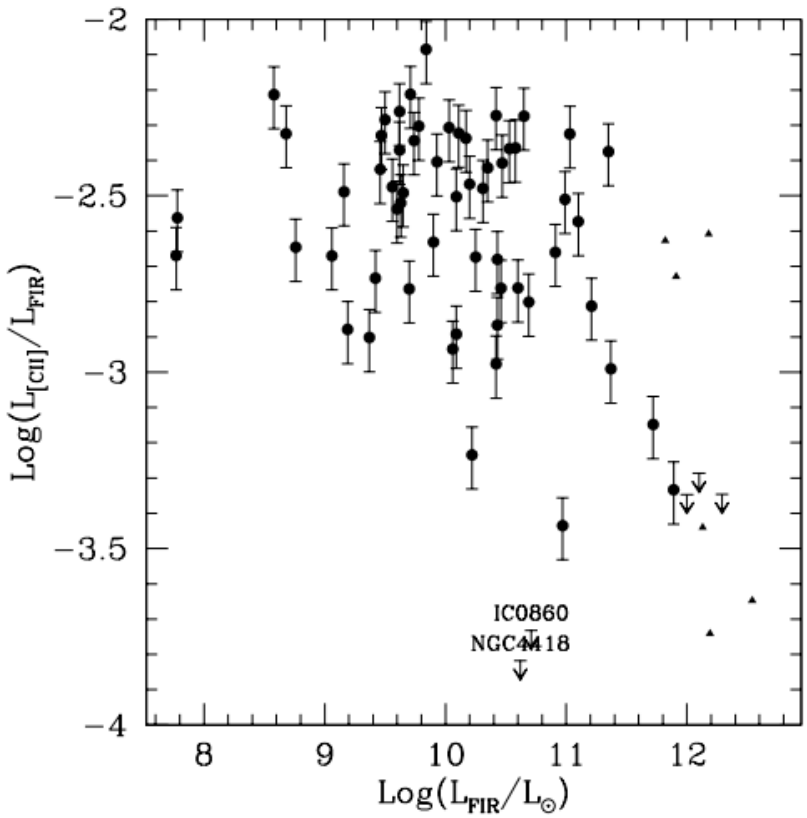

Figure 1.8: The [C II] deficit as observed in local galaxies where the ratio of $L_{[CII]}/L_{IR}$ decreases with increasing L_{IR}. (Malhotra et al., 2001).

bands 7–3, which benefit from minimal atmospheric absorption, making [C II] a particularly accessible far-infrared line for high-redshift galaxies. In the nearby Universe [C II] luminosity is observed to correlate with infrared luminosity (L_{IR}) and SFR for galaxies with $L_{IR} \lesssim 10^{11}\,L_{\odot}$ (e.g. Luhman et al. 2003; Graciá-Carpio et al. 2011; Díaz-Santos et al. 2017; Schaerer et al. 2020).

There is, however, an observed deficit of [C II] emission from galaxies with $L_{IR} \gtrsim 10^{11}\,L_{\odot}$, wherein the ratio of [C II] luminosity to infrared luminosity steeply declines by an order of magnitude as shown in Figure 1.8 (e.g. Malhotra et al. 1997, 2001; Luhman et al. 2003; Graciá-Carpio et al. 2011; Díaz-Santos et al. 2017). The mechanism(s) driving the [C II] deficit are not yet fully understood, though the [C II] deficit is observed across a range of redshifts and galaxy types (e.g. Graciá-Carpio et al. 2011; Smith et al. 2017; Díaz-Santos et al. 2017), which

limits its reliability as an SFR tracer, particularly for the most active galaxies.

Additionally, interpreting [C II] line emission is not straightforward. [C II] has an ionisation energy of 11.3 eV, i.e. significantly below the 13.6 eV required to ionise hydrogen. [C II] can therefore be emitted from both neutral and ionised gas and [C II] lines trace both phases of the ISM.

To measure the source of [C II] emission and probe the origin of the [C II] deficit requires combining [C II] observations with other tracers of the ISM and star-formation.

1.5 Dust-obscured star formation

In the 1990's when the first infrared observatories were launched, namely the *Infrared Astronomy Satellite* (IRAS) and the *Cosmic Background Explorer* (COBE) they unveiled a background of infrared radiation which is roughly equal to the cosmic optical background (Figure 1.9). This indicates that over the history of the Universe, $\sim$ 50% of all UV and optical emissions have been absorbed and reprocessed by dust. Thus UV and optical studies of stellar processes would miss $\sim$ 50% of the light if the IR is not also studied (e.g. Dole et al. 2006; Hodge & da Cunha 2020). This 50% is not evenly distributed among all galaxies. Some galaxies show very little IR emission, while others appear brightest in the IR, and it is this population of IR-bright, dusty star forming galaxies (DSFGs) that makes up the majority of the missing 50%.

1.5.1 ULIRGs

In the local Universe, a population of luminous infrared galaxies (LIRGs), ultra luminous infrared galaxies (ULIRGs) and hyper luminous infrared galaxies (HyLIRGs) are observed, defined as having IR luminosities $> 10^{11}$, $> 10^{12}$ and $> 10^{13} L_{\odot}$, respectively (Sanders & Mirabel, 1996). The high IR luminosities in these populations are caused by dust attenuation of the UV and optical emission from young stars as discussed in Sections 1.3.1 and 1.4.2. The ULIRGs and HyLIRGs are found to almost exclusively be the product of galaxy-galaxy

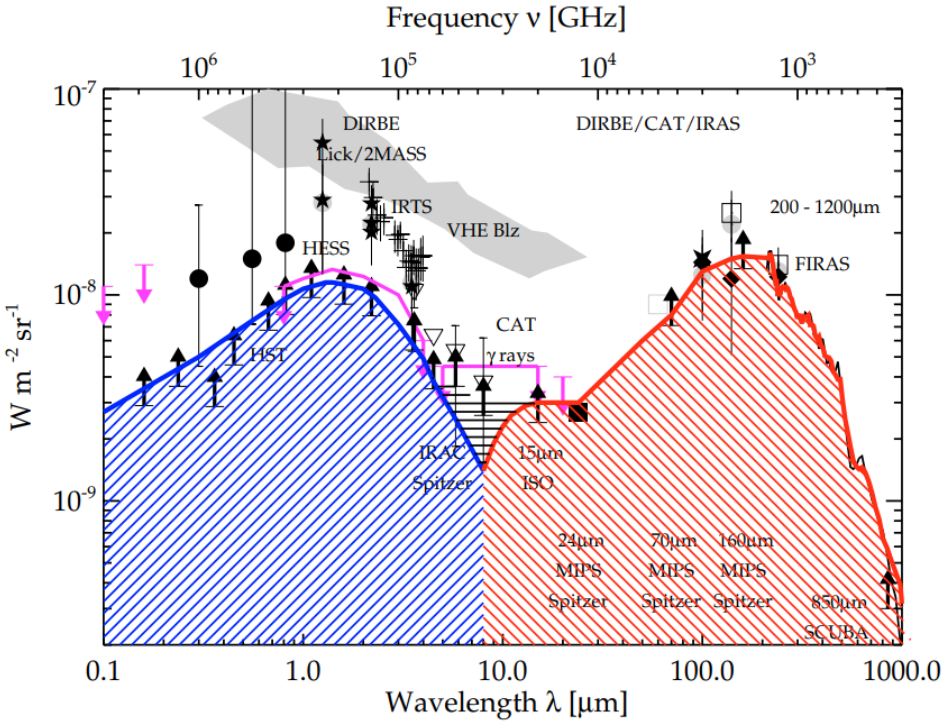

Figure 1.9: The IR background (shaded red) compared to the UV/optical background (shaded blue) (Dole et al., 2006). The similar areas of both regimes shows that observations in the UV and optical miss half of the light emitted by stars and AGN as half of it has been absorbed and reprocessed by dust.

mergers (e.g. Neugebauer et al. 1984; Soifer et al. 1987; Sanders & Mirabel 1996; Downes & Solomon 1998; Sturm et al. 1999; Dasyra et al. 2006; Farrah et al. 2013; Bellocchi et al. 2016).

The amount of dust-obscured star-formation increases out to at least $z \sim 1.5$ with the contribution from the most active systems also increasing across the same redshift range (e.g. Blain et al. 1999; Chary & Elbaz 2001; Dole et al. 2006; Magnelli et al. 2013; Bourne et al. 2017; Gruppioni et al. 2020; Zavala et al. 2021; Traina et al. 2024). This coincides with the peak of the SFRD (as seen in Figure 1.5) and so understanding the contribution of dusty galaxies to the SFRD could help us to understand the drivers of the evolving SFRD, mass buildup and the role of dusty galaxies in the early Universe.

At high redshift ($z > 2$), DSFGs are often observed to reside in proto-clusters (e.g. Chapman et al. 2009; Daddi et al. 2009; Capak et al. 2011; Walter et al. 2012; Ivison et al. 2016; Oteo et al. 2018). Observed overdensities can help place constraints on dark matter halo mass buildup at early times informing models of large scale structure formation as well as starburst triggering studies (e.g. Cooray & Sheth 2002; Dekel et al. 2009; Behroozi et al. 2013) making DSFGs an important population in a wider cosmological context. DSFGs are theorised to be progenitors of early type galaxies (Ivison et al., 2016) and show evidence from morphological studies that bulge formation has already begun in high redshift DSFGs (Rizzo et al., 2021). DSFGs as progenitors of elliptical galaxies is explored further in Section 1.5.3.

Recent observations with the James Webb Space Telescope (JWST) have been revealing the high redshift DSFG population in unprecedented detail, revealing features that support merger and interaction based star formation rate boosting at early epochs (e.g. Polletta et al. 2024; Crespo Gómez et al. 2024).

1.5.2 Submillimeter galaxies

Among the higher redshift IR detected galaxies are a subpopulation known as submillimetre galaxies (SMGs). Originally observed with the Submillimetre Common User Bolometric Array (SCUBA) instrument on the James Clerk Maxwell Telescope (JCMT) (Smail et al., 1997; Hughes et al., 1998; Barger et al., 1998)

these are selected for their 850μm flux. Originally thought to be high redshift analogues of ULIRGS, significant research subsequently took place to constrain their contribution to star formation in the Universe.

Dusty submillimetre galaxies that are selected at far-infrared and submillimetre wavelengths are an important population that contribute up to 50% of the cosmic star-formation rate density during their peak at $z \sim 2$–3 (e.g. Wardlow et al. 2011; Barger et al. 2012; Casey et al. 2013; Zavala et al. 2017; see Casey et al. 2014 for a review), but have a redshift tail that extends to at least $z \sim 6$ (e.g. Casey et al. 2012; Swinbank et al. 2012; Simpson et al. 2014; Cooke et al. 2018; Zavala et al. 2018; Reuter et al. 2020). The selection at 850μm lends itself to naturally discovering SMGs across a range of redshifts due to the effect of the negative K-correction. The 850μm flux is positioned on the Rayleigh Jeans tail of the modified black body used to model dust emission in the SED of an SMG (Sections 1.3.1 and 1.4.1) and thus as the emission becomes dimmer at increasing redshift, the SED is shifted to the right cancelling out the dimming over a redshift range of $1 \lesssim z \lesssim 8$ as shown in Figure 1.10.

SMGs have star-formation rates that typically exceed 300 $M_{\odot}yr^{-1}$ (e.g. Wardlow et al. 2011; Swinbank et al. 2014; Dudzevičiūtė et al. 2020), dust masses $\gtrsim 3 \times 10^8 M_{\odot}$ (e.g. Gullberg et al. 2018; Dudzevičiūtė et al. 2020) and gas masses of $\gtrsim 1 \times 10^{10} M_{\odot}$ (e.g. Bothwell et al., 2013; Birkin et al., 2021) and many SMGs are thought to be undergoing starbursts phases (e.g. Davé et al. 2010; Wardlow et al. 2011; Swinbank et al. 2014; da Cunha et al. 2015; Smolčić et al. 2015; Dudzevičiūtė et al. 2020; Uematsu et al. 2024). When submillimetre galaxies were first discovered, it was thought that they were high redshift analogues for ULIRGs, which primarily have their excess star formation attributed to participation in mergers and tidal interactions, causing compaction of gas (e.g. Sanders & Mirabel 1996; Clements & Baker 1996; Farrah et al. 2001; Surace et al. 2001; Veilleux et al. 2002; Psychogyios et al. 2016). However, as more data became available with which to study SMGs and the advent of interferometry, it was found that the extent of star formation within SMGs is more extended than within ULIRGs (e.g. Simpson et al. 2015; Hodge et al. 2016) and environmental studies have shown that while SMGs tend to reside in overdense environments (e.g. Hickox et al. 2012; Álvarez Crespo et al. 2021; García-Vergara et al. 2020;

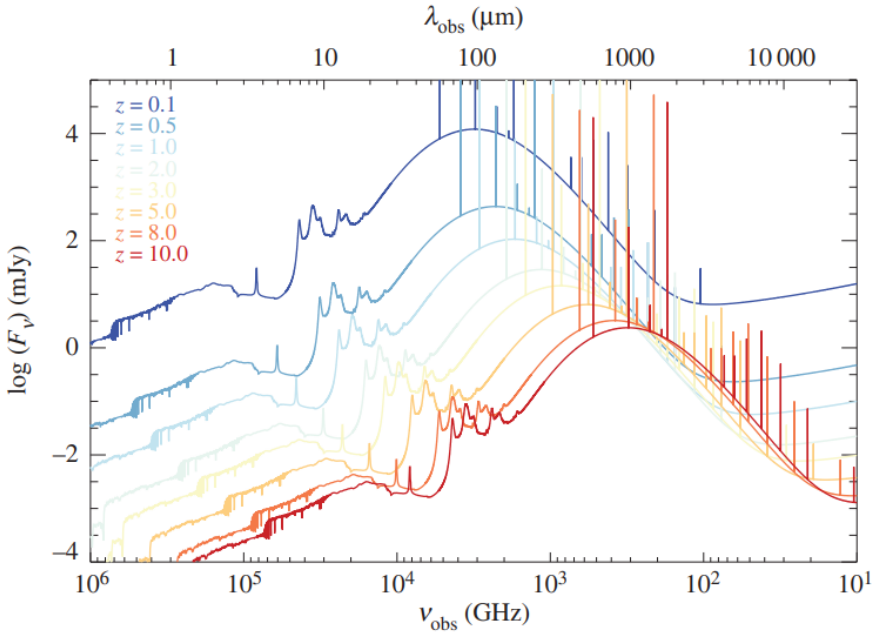

Figure 1.10: The average SED of the ALESS SMG sample (da Cunha et al., 2015) plotted over the redshift range $z = 0.1 - 10$. The dimming of the SED is cancelled out by the redshifting of the SED towards the dust peak causing us to observe an almost constant 870 μm flux from $z \sim 1 - 8$. This effect is known as the negative K-correction.

Cornish et al. *in prep.*) many galaxy pairs that were resolved by ALMA are line of sight chance alignments rather than galaxies at the same redshift which are interacting (Wardlow et al., 2011; Hayward et al., 2018) leading to confusion about the triggering mechanisms compared to ULIRGs which are generally the result of mergers (Section 1.5.1).

The triggering of the high star-formation rates in SMGs remains a topic of debate, with evidence existing for major and minor mergers (Conselice et al., 2008; Davé et al., 2010; Engel et al., 2010), galaxies sharing gas in a pre-merger state (Hayward et al., 2011), SMGs containing undermassive black holes leaving more gas available for star formation (McAlpine et al., 2019), accretion through the cosmic web (Bournaud & Elmegreen, 2009; Dekel et al., 2009) and late stage mergers (Hopkins et al., 2013; Gullberg et al., 2019).

Now, with the Atacama Large Millimetre/submillimetre Array (ALMA; Section 1.6) it is also possible to directly study the gas and dust in high-redshift SMGs to probe the dynamics and triggering in this population. Such studies are possible, targeting far-IR emission lines as tracers of gas, and dust continuum as a tracer of recent star formation (e.g. Carilli & Walter 2013; Hodge & da Cunha 2020 and references therein).

To date, most follow-up studies of SMGs have focused on the $z \sim 2$–3 population, which is brighter at optical and near-IR wavelengths than the higher-redshift population. $z \sim 2$ SMGs typically have stellar masses of $\sim 7 \times 10^8\,\mathrm{M}_\odot$ (da Cunha et al., 2015; Dudzevičiūtė et al., 2020) and dust and gas masses in excess of $10^8\,\mathrm{M}_\odot$ and $10^{10}\,\mathrm{M}_\odot$ respectively (Bothwell et al. 2013; da Cunha et al. 2015; Dudzevičiūtė et al. 2020; Birkin et al. 2021.)

1.5.3 High-z SMGs

Whilst the redshift distribution of SMGs peaks at $z \sim 2.5$ there is a significant tail of sources out to at least $z \sim 6$ (e.g. Swinbank et al. 2012; Simpson et al. 2014; Strandet et al. 2017; Cooke et al. 2018; Zavala et al. 2018; Hygate et al. 2023). While most studies of SMGs have focused on the $z \lesssim 3$ population, the high-redshift ($z \gtrsim 4$) SMGs are of particular interest for models of galaxy formation, as they place tight limits on dust and star formation models in the first $\sim 1\,\mathrm{Gyr}$

after the Big Bang (e.g. Mancini et al. 2016; Behrens et al. 2018; Hayward et al. 2021; Millard et al. 2021; Long et al. 2023).

There is also evidence that these high-redshift SMGs may be the progenitors of $z \sim 1$–2 quiescent galaxies (Toft et al., 2014). Massive quiescent galaxies and high redshift quiescent galaxies have star formation histories consistent with them having formed all their stars in a rapid burst of star formation which quickly depleted their gas reservoirs (Dekel et al., 2009; Toft et al., 2014; Valentino et al., 2020), placing SMGs (and high-redshift i.e. $z \gtrsim 4$ SMGs in particular) as the primary candidates to be the progenitors of such systems.

JWST has been revealing the high redshift SMG population in greater detail than previously achievable, revealing a range of morphologies with no trend in morphology with redshift (Gillman et al., 2023). SMGs also show evidence of inside out galaxy formation exhibited by normal star forming galaxies (Section 1.3.3) supporting central bulge growth and potential for future transformation into an elliptical galaxy.

Thus, an understanding of the dynamics and different mass components and depletion timescales is necessary to reinforce connections between the both low and high-redshift SMGs, and also their theorised descendents.

1.6 ALMA

The Atacama Large Millimetre/submillimetre Array (ALMA)[1] is an interferometer consisting of 50 12 m antennas which make up the main array, and complemented by an additional 12 7 m antennas and four 12 m antennas in a compact configuration. The antennas are fitted with 10 receiver bands which cover the wavelength range 0.32 mm – 8.57 mm (although Band 2 is still under development, having had first light in 2023). Since coming online ALMA has revolutionised observations in the IR and submillimetre, advancing study of DSFGs drastically (see Hodge & da Cunha 2020 for a review). Though ALMA is located on the

[1] ALMA is a partnership of ESO (representing its member states), NSF (USA) and NINS (Japan), together with NRC (Canada), NSTC and ASIAA (Taiwan), and KASI (Republic of Korea), in cooperation with the Republic of Chile. The Joint ALMA Observatory is operated by ESO, AUI/NRAO and NAOJ

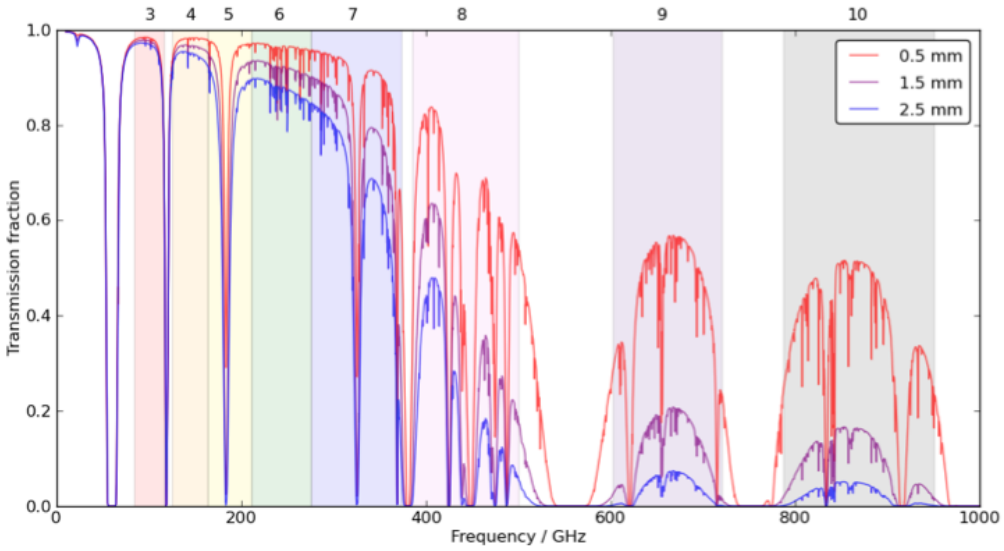

Figure 1.11: The atmospheric transmission at the frequencies of ALMA's wavebands for precipitable water vapour levels of 0.5, 1.5 and 2.5 mm showing how the higher frequency wavebands are greater affected by worsening conditions. Image from https://almaost.jb.man.ac.uk/help/.

Chajnantor plateau, $\sim$ 5000 m above sea level, the shorter wavelengths probed by ALMA are still subject to absorption by the atmosphere which affects the different wavebands to different extents, with better conditions being required for observations in higher frequency bands to reach required depth. The frequency covered by each waveband is shown in Figure 1.11 as well as the impact of worsening atmospheric conditions on transmission in each band.

ALMA allows unparalleled spatial and spectral resolution in the wavelengths of interest. One of its most powerful features is the nature of its observations producing a data cube. It observes the sky in multiple 'spectral windows' (spws) simultaneously. These spws are pre-selected at the point of creating a proposal for ALMA data, with the bandwidth covered and spectral resolution specified by the user. As such, it is possible to spectrally resolve an emission line, and measure the continuum flux at nearby frequencies simultaneously, making ALMA highly efficient for studies of dust and gas in the ISM of galaxies, targeting far-IR tracers such as those mentioned in Section 1.4.

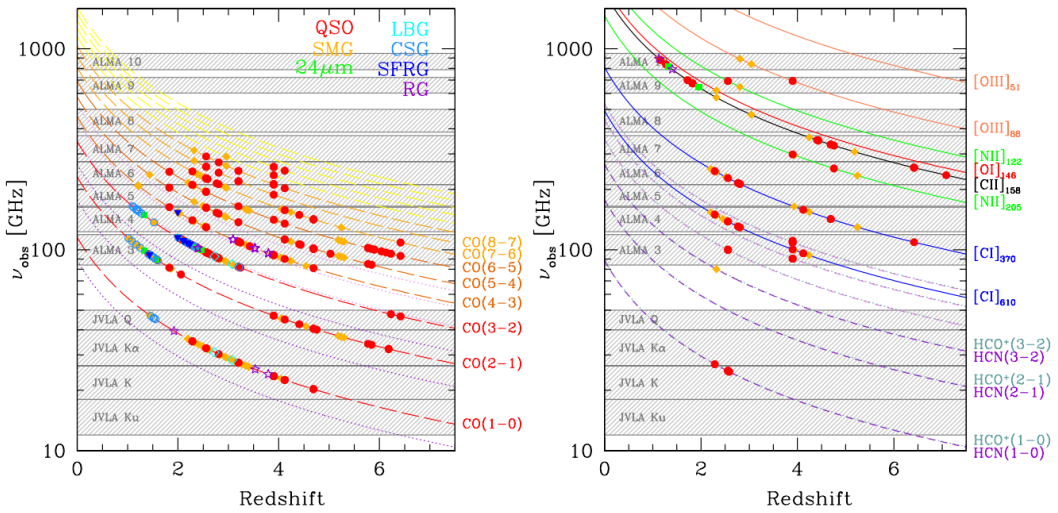

Figure 1.12: The frequencies of the most commonly targeted far-IR emission lines redshifted in the range $0 < z < 8$ overlaid onto the frequency coverage of ALMA bands 3–10 as well as frequency coverage from JVLA. Image from Carilli & Walter (2013).

The antennas that comprise ALMA are moveable, allowing different baselines ranging from 15 m to 16 km, and thus different resolutions, to be achieved from a single instrument. Being an interferometer, the signal is not measured directly, instead the difference in signals between pairs of antennae are measured. Pairs that are positioned closer together are more sensitive to extended emission than ones that are far apart, and vice versa. This means that the weighting of signals from different baselines can be varied in the processing stage changing the resolution of the resultant image. Considerations required when processing ALMA data are explored in Chapter 2.

The ability to fine tune ALMA data makes it an even more powerful tool for galaxy studies, allowing studies of the same galaxies at multiple spatial scales to be achieved with a single observation set. Additionally, the nature of a data cube providing both spectral and photometric data allows line ratios and SEDs to be constrained without requiring time on multiple instruments. ALMA is uniquely placed to be able to observe the most common far-IR line tracers as shown in Figure 1.12 (Carilli & Walter, 2013) across the range of redshifts for which DSFGs and SMGs are observed.

1.7 Aims of this thesis

This thesis utilises new ALMA observations targeting [C II] 158 μm and [N II] 205 μm in 12 $z \sim 4.5$ SMGs to study the origin of the [C II] emission within the ISM, and the nature of $z \sim 4.5$ SMGs.

Chapter 2 describes the data used as well as the considerations that go into performing a custom ALMA data reduction. We describe the flux extraction methodology and resultant catalogue of galaxies with observed [C II] and [N II] emission, the properties of the emission compared to previous detections and serendipitous sources detected in our data. Chapter 3 details the investigation into the properties of the [C II] 158 μm emission line in the resulting sample of $z \sim 4.5$ SMGs. We constrain the portion of [C II] originating from the ionised and neutral ISM and use this information to address theories of the [C II] deficit and the use of [C II] as a tracer of star formation. In Chapter 4 we perform a resolved study of the ionised and neutral gas in $z \sim 4.5$ SMGs including emission region sizes and kinematics to investigate the triggering mechanisms of their rapid star formation. In Chapter 5 we present our final conclusions as well as future work that could be performed leading on from this thesis. Placing additional constraints on the ISM via additional far-IR lines would help constrain results from this work further, and high resolutions from JWST's NIRSpec instrument would allow determination of the kinematics of the ionised gas in these sources, complementing our results from the [C II] line. Applying the methods from Chapter 3 to a wider range of galaxies will help improve the correction of [C II] to account for the deficit, making it a more useful tool for a wider range of galaxies.

Chapter 2

Data Reduction and Detected Line Properties

2.1 Introduction

In order to carry out the analyses in Chapters 3 and 4 to investigate both the properties of the ISM in $z \sim 4.5$ SMGs and the resolved properties of the [C II], [N II] and far-IR continuum, it is necessary to compile a data-set with sources that are detected in both [C II] and [N II]. As such we perform dedicated data reduction on the ALMA observations of the sources as described in Section 2.4. We first process the data to maximise detected flux and create a custom region finding algorithm to optimise the emission extracted from the processed data cubes for use in Chapter 3. The data is then re-processed to create data cubes with increased resolution for the kinematic studies detailed in Chapter 4. During this analysis we search for and describe any serendipitously detected sources present in our data cubes, which we present in Section 2.12.

We use ALMA data for these studies as its powerful data cubes allow us to spatially and spectrally resolve the emission lines of interest as well as giving us measurements of the continuum at those frequencies. As described in Section 1.6, ALMA is an interferometer which measures the difference in signal detected by each pair of antennae. As such, intrinsic ALMA data are a fourier-transform of

the sky (i.e. in the *uv* plane). Most projects then process the data to create a brightness map from which normal scientific analysis can be performed. This is known as CLEANing (Högbom, 1974) and the CLEANing parameters can have non-negligible effects on the output map. Thus, careful consideration is needed when choosing these values.

In this Chapter we will discuss the sample used for the studies contained in Chapters 3 and 4, before explaining how we use CASA to process the data to extract a catalogue of galaxies with measurements of their [C II], [N II] and far-IR continuum emission.

2.2 Sample selection

The sample used in this study comprises 12 SMGs that were initially identified at 870 μm in the LABOCA Extended *Chandra Deep Field*-South Survey (LESS; Weiß et al., 2009) and at 850 μm in the UKIDSS/UDS field by the SUCBA-2 Cosmology Legacy Survey (S2CLS; Geach et al., 2017) single-dish blank field surveys. The 842 (126 from LESS and 716 from S2CLS) submillimetre-selected sources were then followed up with ALMA Band 7 observations to pinpoint the source of the submillimetre emission as part of the ALESS and AS2UDS surveys (Hodge et al., 2013; Stach et al., 2019).

ALESS (Hodge et al., 2013) is an ALMA Cycle 0 program which achieved 3× greater depth than the original LESS observations with a beam size $\sim 200\times$ smaller. This survey resolved at least 35% of the original LESS observations out into multiple individual galaxies. ALESS was the first statistically significant survey of SMGs performed with ALMA leading to redshift distributions (Simpson et al., 2014), matches with optical counterparts for studies of stellar morphologies (Chen et al., 2015), SED fitting (da Cunha et al., 2015) and constraints on AGN fractions (Wang et al., 2013b).

In order to detect larger samples of some rarer objects detected in ALESS, an even larger survey is required to further increase number counts. As such the AS2UDS (Stach et al., 2019) was completed throughout Cycles 1, 3, 4 and 5 yielding 708 detections, a 5× increase compared to ALESS. From this, clustering

studies leading to halo mass estimates were undertaken (Stach et al., 2021), radio properties further constrained (Algera et al., 2020) and links between SMGs and massive local ellipticals demonstrated (Gullberg et al., 2019).

Untargeted searches of the original ALESS and AS2UDS Band 7 data cubes were conducted, identifying two ALESS and 10 AS2UDS galaxies with emission lines in the ALMA wavelength coverage, which were interpreted as most likely to be [C II] emission at $z \sim 4.5$ (Swinbank et al., 2012; Cooke et al., 2018). Given that the [C II] line is expected to be $\sim 10\times$ brighter than other lines that may be detected (e.g. [N II], [O I], or high-J^{12} CO) Swinbank et al. (2012) and Cooke et al. (2018) assume that contamination from these lines is unlikely for the shallow depth of their data. Additional multiwavelength analysis supported this conclusion in all but two cases (AS2UDS 0243.0 and AS2UDS 0535.0; Cooke et al. 2018). AS2UDS 0243.0 and AS2UDS 0535.0 both have photometric redshifts indicating their line detection could be lower-z CO, discussed in Section 2.11.

This thesis presents follow-up Band 6 and deeper Band 7 data targeting all 12 SMGs with emission lines in the original ALESS (two galaxies) and AS2UDS (10 galaxies) with the goal of detecting [N II] 205 μm and [C II] 158 μm in Band 6 and Band 7, respectively. Additionally, AS2UDS 0002.0 and AS2UDS 0109.1 are covered by our observations in both bands and we search for emission from these sources. The summary of our findings for individual sources is in Sections 2.11 and 2.12.

2.3 Observations

The observations were tuned to target [C II] and [N II], assuming that the emission lines detected in the original Band 7 data were [C II] at $z \sim 4.5$ (Swinbank et al., 2012; Cooke et al., 2018). The data were taken for ALMA project 2018.1.01140.S (PI: Wardlow) between December 2018 and October 2019 (Cycle 6). These observations are designed in such a way to obtain new [C II] measurements that are twice as deep as the original detections over a single beam (requested to be 0.5″). [N II] observations that are 6 times deeper were requested, to ensure that

a [C II]/[N II] ratio of up to 20 can be detected in most sources, and up to 35 in the brightest three.

The new Band 7 observations of ALESS SMGs were taken on 2018 December 08 using 49 ALMA antennae with a maximum baseline of 783.5 m (corresponding to a spatial scale of 0.18″). The new Band 7 data in AS2UDS were obtained on 2019 October 17 with 46 antennae and a maximum baseline of 740 m (corresponding to a spatial scale of 0.18″). SMGs were observed for ~ 150 s each and both sets of Band 7 data were taken with mean precipitable water vapour (PWV) of 0.9 mm. Observations have a spectral resolution of 15.6 MHz (~ 13.4 km s^{-1} at 350 GHz).

The Band 6 data for the ALESS SMGs were observed in three execution blocks on 2018 December 26, 2018 December 27 and 2019 April 7 with 51, 47 and 42 antennae and maximum baselines of 480–500 m. The mean PWV was between 1.0 mm and 2.8 mm for the three execution blocks. Both ALESS sources were observed for ~ 2812 s each. All Band 6 observations have a spectral resolution of 15.6 MHz (~ 17.3 km s^{-1} at 270 GHz). AS2UDS 0002.1, AS2UDS 0208.0, AS2UDS 0535.0 and AS2UDS 0643.0 were observed in three execution blocks on 2018 December 10–11 using 47 antennae and maximum baselines of 783.5 m. The mean PWV was between 1.5 mm and 1.6 mm. Each source was observed for ~ 1630 s. The remaining AS2UDS targets were observed in four execution blocks with 46 antennae on 2018 December 11–13. The mean PWV was between 1.2 mm and 1.9 mm and the maximum baseline was 783.5 m. Each source was observed for ~ 1940 s.

2.4 Data reduction

2.4.1 CLEANing parameters

Our ALMA data are processed using the Common Astronomy Software Application (CASA) (McMullin et al., 2007) version 5.6.1. CASA (McMullin et al., 2007) was created to give astronomers the tools needed to process their own interfometric data to optimise the output science they wish to perform with it. It contains

a variety of pre-made routines for purposes such as converting the native CASA image format (which is optimised for better efficiency) to the more standard FITS file format, tools for data extraction and analysis, as well as routines to turn the visibility files into an image.

We received calibrated measurement sets (ms file) from the European ALMA Regional Centre (ARC) using their 'request calibrated ms' file service. Prior to the data being made available to download the ARC performs quality assurance checks to monitor for example, the response of the antennas, their temperatures, weather conditions etc. to ensure the data taken is able to meet the science goals stated in the proposal for the data.

Upon receiving the calibrated ms files, the CASA task TCLEAN is used to image the data. Before going into detail about the CLEANing process we first outline the TCLEAN parameters that are important and which should be understood before proceeding with data reduction.

The first parameter is 'specmode' for which the only options we will consider are 'mfs', standing for multi-frequency synthesis, where a single channel continuum image is produced, and 'cube', where a multi-channel data-cube is produced for the purpose of spectral line imaging.

'cell' determines the physical size represented by each pixel in the resultant image and is determined by finding the expected resolution of the image, which we calculate using

$$\frac{\lambda}{b_{max}} \times 206265 \tag{2.1}$$

where λ is the central wavelength of the observations and b_{max} is the maximum baseline of the array during data acquisition where λ and b_{max} are in the same units, and the constant of 206265 converts the ratio to arcseconds. The maximum baseline is provided in the weblog supplied with the data, and also in the ALMA QA2 file. The optimum cell size has between 4–6 pixels per resolution element. This is the idealised beam and does not take into account of factors that will affect the actual beam size, such as position of antennas.

'imsize' determines the total size of the image and is optimised by taking the average wavelength, λ, and dividing by the diameter of one antenna, D, and again

multiplying by the constant to give

$$\mathrm{FoV} = \frac{\lambda}{\mathrm{D}} \times 206265 \tag{2.2}$$

with the Field of View (FoV) in arcseconds. FoV is then divided by the cellsize to give the imsize in pixels. Particular imsize values optimize the internal CASA Fast Fourier Transform (FFT) routines. Optimal values are even and divisible by 2, 3 or 5 only (McMullin et al., 2007). The tool 'synthesisutils' is used to find the nearest optimum value to the calculated imsize. Our data have cellsize=0.04″ and imsize=750 pix for Band 7, cellsize=0.08″ and imsize=504 pix for the ALESS Band 6 data, and cellsize=0.05″ and imsize=840 pix for the AS2UDS Band 6 data.

The 'weighting' option determines how the signals from different baselines are weighted in the final image. By selecting 'Briggs' weighting, the user gains control of baseline weighting via the 'ROBUST' parameter which ranges in value from −2.0 to +2.0 allowing a smooth transition between uniform and natural weighting (Briggs, 1995). Natural weighting gives all baseline samples equal weighting. As shorter baselines are more densely sampled than longer baselines, this results in the overall image having a higher weighting towards shorter baselines, resulting in poorer overall resolution (larger beam size). On the other hand uniform weighting gives equal weight to all baselines regardless of how densely they are sampled, resulting in better angular resolution (smaller beam size) but a loss of signal due to increased noise as a result of weighting down data points from densely sampled baselines to give an overall uniform result.

The 'gridder' parameter determines what model is used to resample the weighted visabilities (as a function of baseline and wavelength of observation) into a standard *uv* grid. The *uv* plane grid measures the signal in terms of baseline separations measured in units of wavelength as seen by the source. It is this weighted grid that is has an FFT applied to it to create the image.

At this point it is possible to produce an image without performing any CLEANing cycles, creating what is known as a 'dirty' image. This is the result of purely Fourier transforming the signals from the *uv* plane and will contain artefacts from the 'dirty' beam, i.e. a Gaussian with sidelobes. These may show

up as ripples in the image around sources. It is the deconvolution stage that takes an image from dirty to clean.

To produce a CLEANed image the 'deconvolver' must be selected. The deconvolver is responsible for deconvolving the true sky brightness map from the point spread function (PSF) of the instrument. This is where the 'CLEANing' part of the algorithm TCLEAN comes into play. In essence, the 'CLEANing' algorithm searches for peaks in amplitude in the dirty image and then subtracts a scaled version of the PSF (or 'dirty beam') from this location. It then adds the removed amplitude to the new 'model' image, and leaves behind a new residual image from which the amplitude has been removed. This process is repeated until no amplitude peak is found above the user defined image noise level. A 2D illustration of this process is displayed in Figure 2.1. Once the brightness map has been recreated, this is then convolved with the idealised beam to create the final image.

Finally, the masking method used for the deconvolution is the final option to consider. Only pixels within the mask will be searched for amplitude peaks by the deconvolver, as opposed to using the whole image which would be much more computationally intensive and could lead to noise peaks being amplified. There are three choices for masking: 'user' which implements a custom-user created mask, typically around any visible sources, 'pb' where the primary beam generated by the gridder is used (which only works with some gridder options), and 'auto-multithresh' where regions are created using multiple sub-parameters. These define things such as; the amplitude at which to consider something a potential source, the minimum number of contiguous pixels that must comprise a real source, and the kernel size that is used to convolve and smooth masks.

While 'auto-multithresh' is the most complicated with the number of sub-parameters it requires, it is useful as it is designed to emulate what an experienced user would select, and eliminates user bias, standardising the masking process. Once sub parameters that work for the data are found it can be quickly applied to many images without requiring the user to directly guide the cleaning process.

The CLEANing process can be performed interactively, meaning that CASA will display the residual image after each CLEANing cycle, (this can be useful for learning how the CLEANing process works and for keeping tabs on the sources

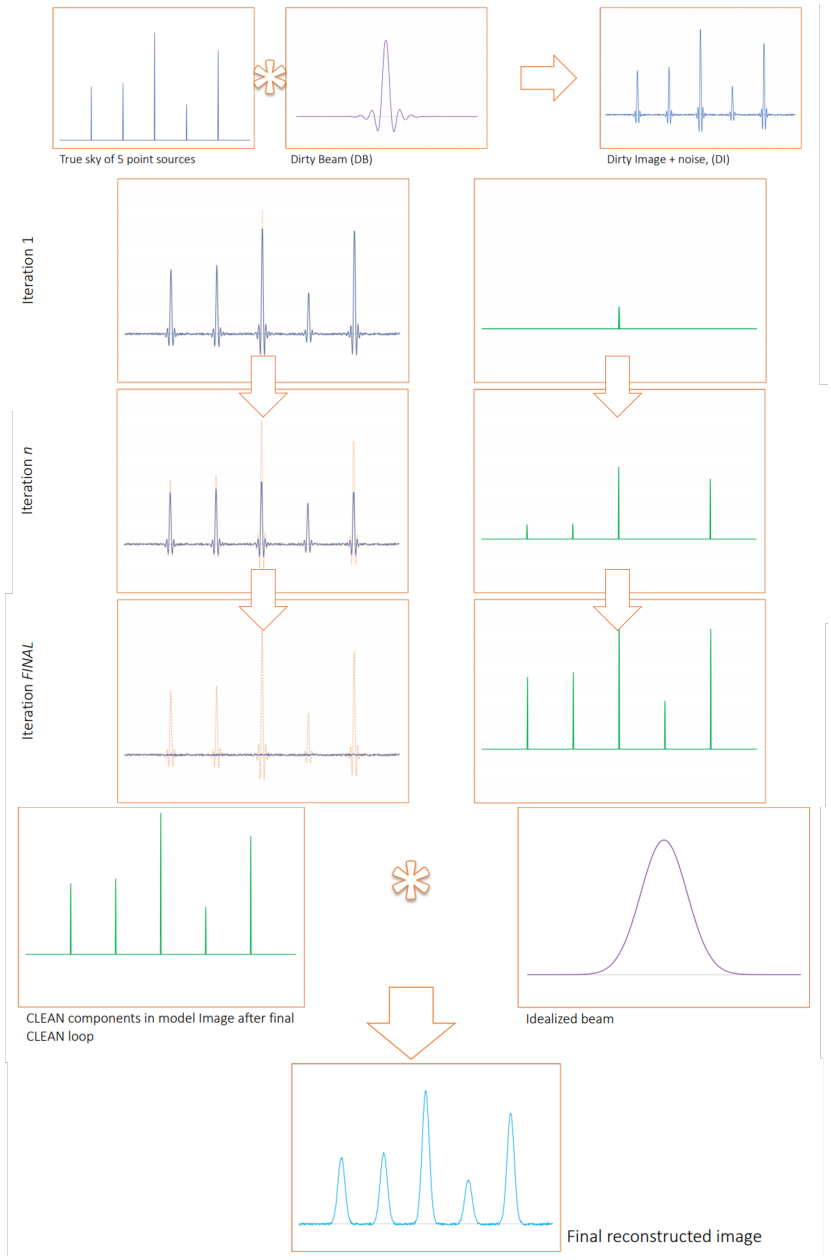

Figure 2.1: 2D Illustration of how the CLEANing process works and why it is needed. The initial image is a function of the true sky brightness map and the 'dirty beam' which through repeated cleaning cycles is CLEANed into the brightness map convolved with a 'clean' beam, removing fringes and artefacts (Högbom, 1974). The top row shows the components of the dirty image, i.e. the true sky brightness map, the dirty beam and noise. The left column of the 'iteration' images shows how flux is removed from the dirty image by successively subtracting scaled versions of the dirty beam from the amplitude peaks, until only noise remains. The right column shows the removed amplitude being successively added to the clean image. The final image is produced by convolving the recovered fluxes with the idealised beam as shown in the bottom row.

being CLEANed), but it also slows the CLEANing process. The non-interactive option proceeds with successive cleaning cycles without displaying the residual image and masks after each cycle, allowing full automation of the process.

2.4.2 The CLEANing of this data

We next detail the CLEANing process undertaken for the ALMA data used in this thesis and explain our choice of parameters. We use the data as we received it from the ARC and applied no time averaging to the data.

We start by imaging the data without CLEANing to produce 'dirty' cubes from which an initial visual search for emission lines at the positions of the SMGs is conducted. The dirty cubes are also visually inspected for the presence of any additional, serendipitous line sources. We identify three additional line emitters within our observations, which are discussed in Section 2.12.

Frequency channels containing emission lines are then excluded and the rest of the cube collapsed along the frequency axis to create a dirty continuum map using 'mfs' mode in TCLEAN. This dirty continuum map is used to visually identify new continuum emitters. We identify four untargeted continuum emitters.

To generate cleaned spectral cubes we use UVCONTSUB to fit and subtract the continuum in the *uv*-plane and then use TCLEAN to mask the previously-identified spectral emission and clean the data. Primary beam corrected images are created using the primary beam maps created by CASA. We use a fit order of zero (flat line) for the Band 7 data and one (tilted line) for the Band 6 as the Band 6 data resides in a steeper portion of the dust spectral energy distribution and the continuum is poorly fit by a flat line.

To produce cleaned images from the continuum subtracted visibility files we again use TCLEAN, using 'cube' mode to create cleaned, continuum-subtracted, emission line cubes. We select Briggs weighting and set ROBUST = 2.0 (i.e. natural weighting). While natural weighting gives the poorest resolution, it maximises the available flux. This is required for the science that we undertake in Chapter 3 which targets integrated fluxes. We also still need to robustly confirm which sources have detected emission lines, which also requires maximising the

signal to noise ratio (SNR). We use the 'standard' gridder as it is computationally less intensive than other available options, and it is suitable for point-like sources in a single image and is therefore applicable for our data. We use the 'HOGBOM' deconvolver for the CLEANing algorithm. HOGBOM is selected as it uses a point source delta function, which is best for isolated point sources (which our data are mostly expected to be) as well as being computationally efficient. We use the 'auto-multithresh' masking technique because it automates the masking process as described in Section 2.4.1. The sub-parameters that we set for auto-multithresh are the 'sidelobethreshold' (3.0), 'noisethreshold' (3.5), 'minbeamfrac' (0.3), 'lownoisethreshold' (1.5) and 'negativethreshold' (7.0).

We find only insignificant changes to the output images (and the flux recovered from them) when changing the sub-parameters controlling the auto-masking, indicating that it is doing a good job of identifying peak emission.

The images are cleaned to 3× the theoretical rms noise level (σ in Jy) calculated as:

$$\sigma = \frac{2k_B T_{sys}}{\eta_q A_{eff} \sqrt{\Delta v \Delta t}} \tag{2.3}$$

where k_B is the Boltzmann constant, T_{sys} is the system temperature in K, $\eta_q = 0.9$ (a term to parametrize losses during correlation), A_{eff} is the effective area which equals 0.9 (aperture efficiency) times the area of a single antenna in m^2, Δv is the bandwith of a single channel in MHz, and Δt is the integration time in seconds. Values of T_{sys} and Δv are provided in the weblog file supplied with the data, and Δt can be found by creating a '.listobs' file from the visibility data. The theoretical noise limit is used as the cleaning process will affect the noise in the resultant image, and since the dirty images have not been cleaned the noise level measured empirically from them is not representative of the expected noise level in a final cleaned image.

The process is the same for CLEANing the continuum data, except the non-continuum subtracted visibility files are used, emission line free channels are selected and 'specmode' is set to 'mfs'.

The cleaned continuum images and spectral cubes are used for the final identification of spectral line and continuum emission and these are measured from

the primary beam corrected data as outlined in Sections 2.5 and 2.6.

All resulting Band 6 data have beamsizes of $\sim 0.5 \times 0.5$ arcsec and typical continuum noise levels of ~ 0.1–0.5 mJy beam^{-1} when imaged with ROBUST = 2.0 CLEANing (Section 2.4). For Band 7 these values are $\sim 0.45 \times 0.35$ arcsec for the beam and continuum noise levels of ~ 1–5 mJy beam^{-1}.

Finally, we ensure that no emission is 'resolved out'. This effect applies when an array configuration does not provide baselines short enough to be sensitive to extended emission. As a result emission can be missed by the observations giving an underestimation of the sources true brightness. A simple test of whether data may be missing flux is to perform 'uv-tapering'. By tapering the data, longer baselines are completely removed, leaving only baselines that are shorter and more sensitive to extended emission. If the flux measured from tapered data increases significantly compared to data that includes all baselines, it is an indication that there may be extended emission which is being missed by the array configuration. We perform this analysis on our data, tapering the Band 7 data such that it has a beam size of 0.8 arcsec and the Band 6 to 1.0 arcsec (roughly double the original beams with ROBUST = 2.0). One of our targets, ALESS 65.1, shows a significant increase in measured flux with tapering. However the increase is proportionally equal in Band 6 and 7, meaning the results in Chapter 3 do not change by using untapered data.

The images described above are used for all the analyses in Chapter 3. For the analyses in Chapter 4 we re-image the data, changing only the ROBUST parameter to 0.0. This gives greater resolution and a smaller beam for resolved studies of the [C II], [N II] and continuum emission. By re-imaging with ROBUST=0.0 we achieve a beam of $\sim 0.40 \times 0.30$ arcsec in Band 7, and a Band 6 beam of $\sim 0.40 \times 0.35$ arcsec, however AS2UDS 0109.1 becomes undetected at this resolution due to residing at the edge of the image where noise is greater. We also explore ROBUST $= -2.0$ (uniform weighting) but find the majority of sources became undetected at this resolution and so it is not used any further. The effect on the output image of changing the ROBUST parameter is shown in Figure 2.2 where a lower ROBUST value produces a noisier image with a smaller beam and more pronounced structural features.

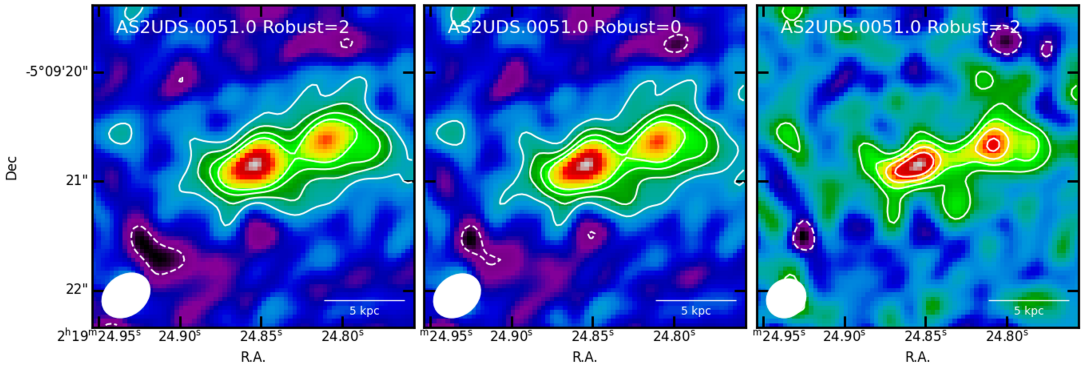

Figure 2.2: The effect of changing the ROBUST setting on the output image for our most extended source; AS2UDS 0051.1. The left-most panel shows AS2UDS 0051.1 imaged with ROBUST = 2.0 which produces the largest, most elongated beam and lowest noise image. As ROBUST is changed to 0.0 (centre) and -2.0 (right) the beam size shrinks as shorter baselines are down-weighted, and the background noise level rises compared to the source. The white solid contours are set at 3, 5, 7 and 9σ while the dashed contours are at -3σ. The ellipse in the bottom left of each panel shows the beam size.

2.5 Continuum measurements

Band 6 (260 GHz) and Band 7 (350 GHz) continuum fluxes are measured from the primary beam corrected images at the position of each target SMG and for the untargeted line and continuum emitters identified in Section 2.4.2. These continuum fluxes are measured using the CASA task IMFIT, which fits 2D Gaussian ellipses to the peak of emission found within pre-defined search regions. For the targeted SMGs we base these regions on the coordinates from Swinbank et al. (2012) and Cooke et al. (2018), and for the untargeted sources the emission peak location is used. The size of the region is typically 4", and is chosen to allow recentroiding but restricting each fit to only one source.

In one case, AS2UDS 0051.0, the source is significantly extended and there are two main emission regions, with the western source having a low surface brightness in Band 7, shown in Figure 2.2 and discussed in Section 2.11. Therefore, IMFIT is unable to automatically identify and fit all the extended flux in AS2UDS 0051.0, and in this case we instead manually define an extraction region using the algorithm described in Section 2.6. We then use IMFIT to measure the

Table 2.1: Far-infrared properties of the 12 targeted SMGs.

Source	z^a	$S_{260\,\mathrm{GHz}}{}^b$ (mJy)	$S_{350\,\mathrm{GHz}}{}^c$ (mJy)	$L_{\mathrm{IR}}{}^d$ ($10^{12}\,L_\odot$)	SFR $\mathrm{M}_\odot\mathrm{yr}^{-1}$
AS2UDS 0002.1	-	7.16 ± 0.38	9.78 ± 0.35	-	-
AS2UDS 0051.0	4.421	4.85 ± 0.33	6.39 ± 0.93	6.51 ± 0.95	1124 ± 164
AS2UDS 0104.0	4.423	4.37 ± 0.19	6.07 ± 0.30	6.18 ± 0.30	1065 ± 52
AS2UDS 0109.0	4.450	5.51 ± 0.22	6.77 ± 0.55	6.90 ± 0.56	1190 ± 97
AS2UDS 0109.1	4.451	1.45 ± 0.20	-	2.74 ± 0.59	472 ± 102
AS2UDS 0208.0	-	2.41 ± 0.15	4.27 ± 0.21	-	-
AS2UDS 0232.0	-	3.72 ± 0.19	5.48 ± 0.27	-	-
AS2UDS 0243.0	1.63	2.83 ± 0.15	4.60 ± 0.27	-	-
AS2UDS 0535.0	4.601	1.15 ± 0.092	2.06 ± 0.38	2.12 ± 0.39	365 ± 67
AS2UDS 0568.0	4.404	1.27 ± 0.072	1.76 ± 0.42	1.79 ± 0.43	309 ± 74
AS2UDS 0643.0	4.98	1.39 ± 0.15	2.27 ± 0.19	-	-
ALESS 61.1	-	2.51 ± 0.051	4.44 ± 0.20	-	-
ALESS 65.1	4.445	1.56 ± 0.033	5.93 ± 0.29	6.05 ± 0.29	1042 ± 49

[a] Spectroscopic redshift from Swinbank et al. (2012) and Cooke et al. (2018) and confirmed by our measurements for galaxies with [C II] and [N II] detections. For galaxies with other detected lines, redshifts are from our new line identity suggestions.
[b] Continuum flux in Band 6 (260 GHz), measured as described in Section 2.5.
[c] Continuum flux in Band 7 (350 GHz), measured as described in Section 2.5.
[d] Infrared luminosity measured over the rest-frame 8–1000 μm as described in Section 2.10.

flux density in this custom region for Band 7.

AS2UDS 0109.1 is serendipitously included in our observations of AS2UDS 0109.0; however the 11" separation of the two sources means that AS2UDS 0109.1 is in a region of low primary beam coverage/high noise and its continuum is not detected in Band 7.

Table 2.1 contains the measured continuum fluxes of all targets. For 10 of the 12 targets (83%) our Band 7 flux measurements from the new Cycle 6 data are consistent with those presented in Hodge et al. (2013) and Stach et al. (2019) (Cycles 0 and Cycles 1–3, respectively). The exceptions are AS2UDS 0002.1 and AS2UDS 0232.0, which are brighter in our data at the 3.9σ and 2.2σ level, respectively. The difference is likely to be the result of the higher resolution observations

of Stach et al. (2019) resolving out flux in these sources.

2.6 Line measurements

In order to measure the flux from the emission lines we use an iterative process; we initially extract the spectra from beam-size regions at the SMG positions (from Cooke et al. 2018; Swinbank et al. 2012) in continuum-subtracted cubes that have not been corrected for primary beam response. We then visually examine these spectra to identify channels containing line emission (by identifying the point at which the emission level returns to being consistent with the image noise) and then collapse the cube over these channels to create a 2D pseudo-image of the line, which is used to identify any extended line emission. The RMS noise in these pseudo-line images is measured and pixels containing more than 2.5× the noise are identified.

Pixels containing signal greater than 2.5× the RMS are identified using a 'spiral search' algorithm. The spiral search begins at a user-supplied start pixel, usually the centre of the emission, and the algorithm moves out in a spiral motion. When a pixel in the image is found to have a value $> 2.5\times$ the noise, the corresponding pixel in a mask map is set to 1. The search terminates when a whole spiral loop is completed without finding any qualifying pixel values, or when the search has travelled more than 75 pixels away from the start along the x axis. This corresponds to ~ 3 arcsec and is larger than any of our sources are expected to be. The second stop condition exists for images with high noise, which can have small islands of noisey pixels with fluxes above the noise threshold. Thus the spiral search identifies groups of contiguous pixels containing flux from the target.

At this point all the emission from the source has been identified, however we find that the identified region often includes small extensions and features that may include noise that happens to be adjacent to the source. We attempt to remove these by setting a higher flux threshold but find that this shrinks the whole region, including the loss of real flux while the (now shrunken) extensions remain. As such, we instead convolve the detected regions with a Gaussian kernel that is

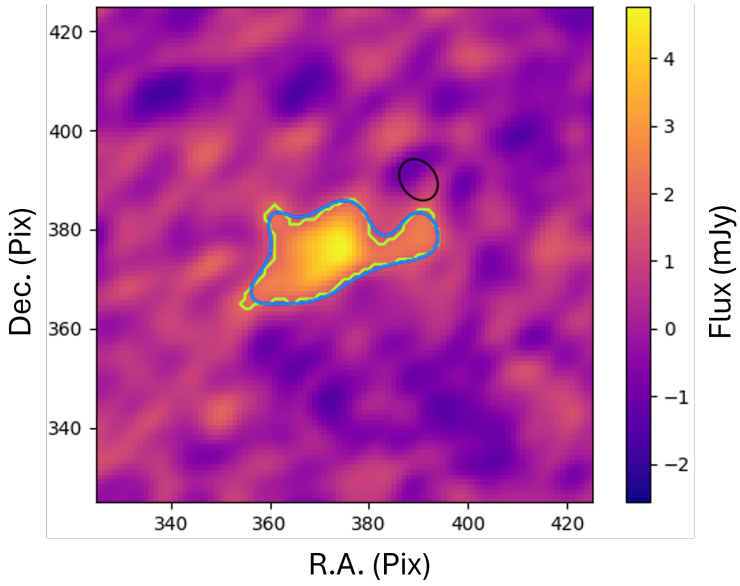

Figure 2.3: The appearance of an extraction region before (yellow line) and after (blue line) convolution with a kernel 0.5× the FWHM of the beam as described in Section 2.6. The beam size is shown by the black ellipse. The background image is the collapsed 'pseudo' [C II] image used for selecting pixels to include in the region.

0.5× the FWHM of the beam. This results in the mask no longer containing only ones and zeroes, but having region edges that taper down in a Gaussian manner. We select pixels with $\geq 1/3$ of the kernel peak to comprise the final extraction region. The convolution step captures regions containing real flux that is below the 2.5σ level whilst also smoothing the edges of the extraction region to ensure that unphysical features that are smaller than the beam are not given undue weight. An example of the effect of this convolution on the final region is shown in Figure 2.3.

We verify the convolution and the chosen kernel size by measuring the returned line fluxes and signal-to-noise ratio (SNR) for various pixel value cutoffs and kernel sizes. The selected convolution parameters optimise the extracted flux and SNR across all targets, as shown in Figure 2.4.

Using the new region we re-extract the spectrum and repeat the process starting with the identification of channels containing line emission. This whole process is repeated until the channels containing flux do not change with each newly created extraction region, i.e. the line emitting channels converge.

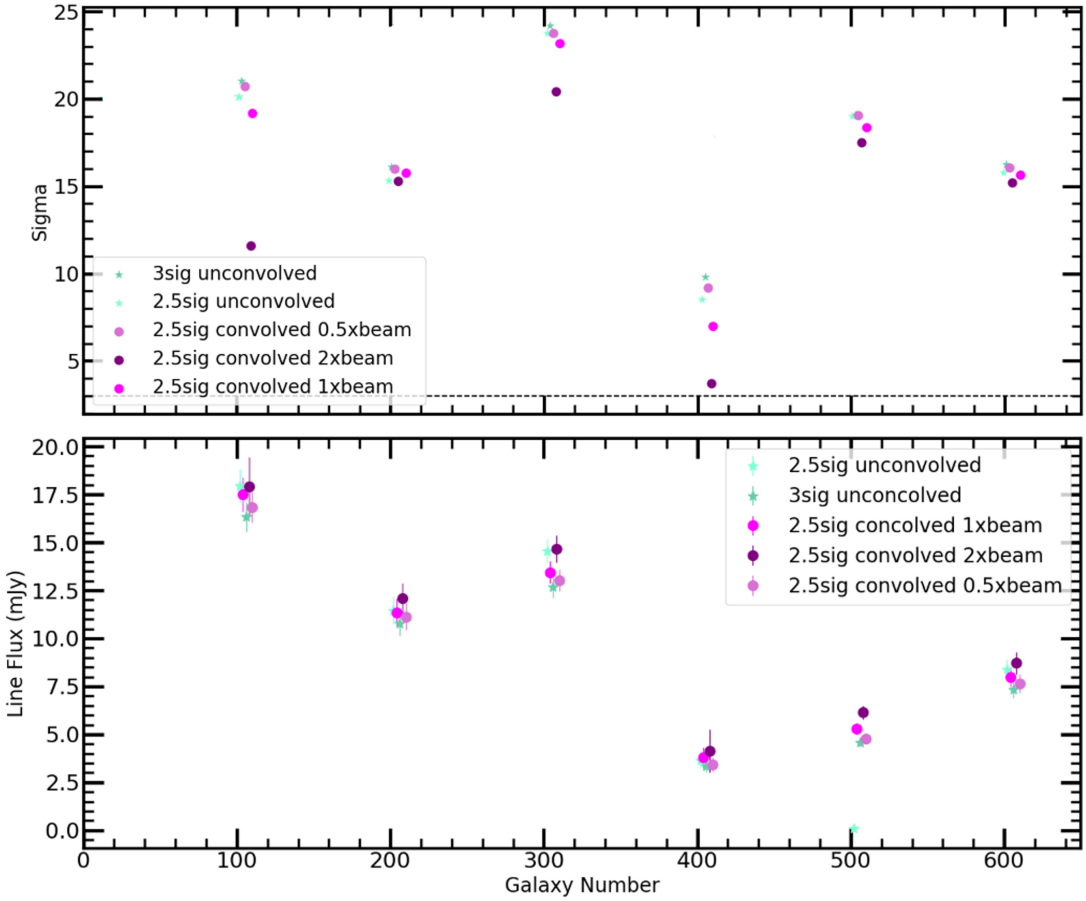

Figure 2.4: A comparison of how different sized convolution kernels affects the extracted flux (*bottom*) and SNR (*top*) from each source. Stars represent regions that have not been convolved with the beam and are selected on pixels above 2.5× and 3× the noise level (lighter and darker stars, respectively). Circles show the regions selected above 2.5× the noise and then convolved with kernels that are 0.5×, 1× and 2× the FWHM of the beam. The 0.5× kernel gives the best tradeoff between measured flux and SNR. Each grouping of points on the x-axis represents measurements from a different galaxy which are spaced out in intervals of 100 for visualisation purposes. The points within each galaxy grouping are offset for ease of viewing.

Table 2.2: Line properties derived for the observed ALESS (AL) and AS2UDS (AS) sources. All quoted fluxes are the integrated line flux ($S_{line}dv$).

Galaxy	Band 7 Obs. Freq (GHz)	Band 7 Line	Band 7 Flux (Jy km s^{-1})	Band 7 Lum $10^9\,L_\odot$	Band 6 Obs. Freq (GHz)	Band 6 Line	Band 6 Flux (Jy km s^{-1})	Band 6 Lum $10^7\,L_\odot$
AL 61.1	-	-	-	-	-	-	-	-
AL 65.1	349.14	[C II]	4.67 ± 0.18	2.94 ± 0.12	268.3	[N II]	0.41 ± 0.08	20.0 ± 4.1
AS 0002.1	-	-	-	-	-	-	-	-
AS 0051.0	350.91	[C II]	18.1 ± 0.89	11.3 ± 0.56	269.92	[N II]	0.55 ± 0.1	26.6 ± 5.0
AS 0104.0	350.44	[C II]	11.63 ± 0.74	7.27 ± 0.46	269.37	[N II]	0.77 ± 0.07	28.4 ± 2.5
AS 0109.0	348.72	[C II]	14.82 ± 0.63	9.35 ± 0.40	268.05	[N II]	1.44 ± 0.09	70.0 ± 4.3
AS 0109.1	348.63	[C II]	1.6 ± 0.2^a	1.01 ± 0.13	268.09	[N II]	0.13 ± 0.03	6.13 ± 1.55
AS 0208.0	-	-	-	-	-	-	-	-
AS 0232.0	-	-	-	-	-	-	-	-
AS 0243.0	350.99	CO(8-7)	3.69 ± 0.43	-	-	-	-	-
AS 0535.0	339.26	[C II]	6.61 ± 0.35	4.40 ± 0.23	260.89	[N II]	0.13 ± 0.03	6.71 ± 1.49
AS 0568.0	351.78	[C II]	8.72 ± 0.55	5.42 ± 0.34	270.41	[N II]	0.08 ± 0.02	3.61 ± 0.72
AS 0643.0	-	-	-	-	244.36	[N II]	0.43 ± 0.05	-

[a] This flux value and corresponding luminosity is taken from Cooke et al. (2018) as the value we obtained was uncertain due to noise at the image edges where this source resides in Band 7.
For AS2UDS 0243.0 while the line in B7 is at the expected frequency there is no corresponding detection in B6 and so we refer to the photometry to conclude this is a $z = 1.63$ source.The observed line in AS2UDS 0643.0 is not at the expected frequency a discussion of why we believe this line is still [N II] can be found in 2.11 along with a new redshift estimate.
Fluxes are measured using the methods described in Section 2.6 and luminosities calculated using redshifts determined in Section 2.9.

Spectra are extracted from the identified line emission regions using the CASA task SPECFLUX and the extracted spectra are fit with 1D Gaussians using a Levenberg-Marquardt Least-Squares fitting algorithm from ASTROPY (Astropy Collaboration et al., 2022). From these fitted gaussians the integrated flux is measured. To measure the uncertainty on the flux and thus the SNR, we first measure the spectral noise as the standard deviation of the emission free channels. The error on the line flux is calculated by adding this level of random noise to the spectrum and refitting the gaussian. This fitting process is repeated 1000 times and the standard deviation of these new measurements taken for the error on flux.

The extracted spectra and their fits are presented in Figure 2.5; measured parameters of the lines are listed in Table 2.2. Line fluxes measured here are used for the analyses in Chapter 3.

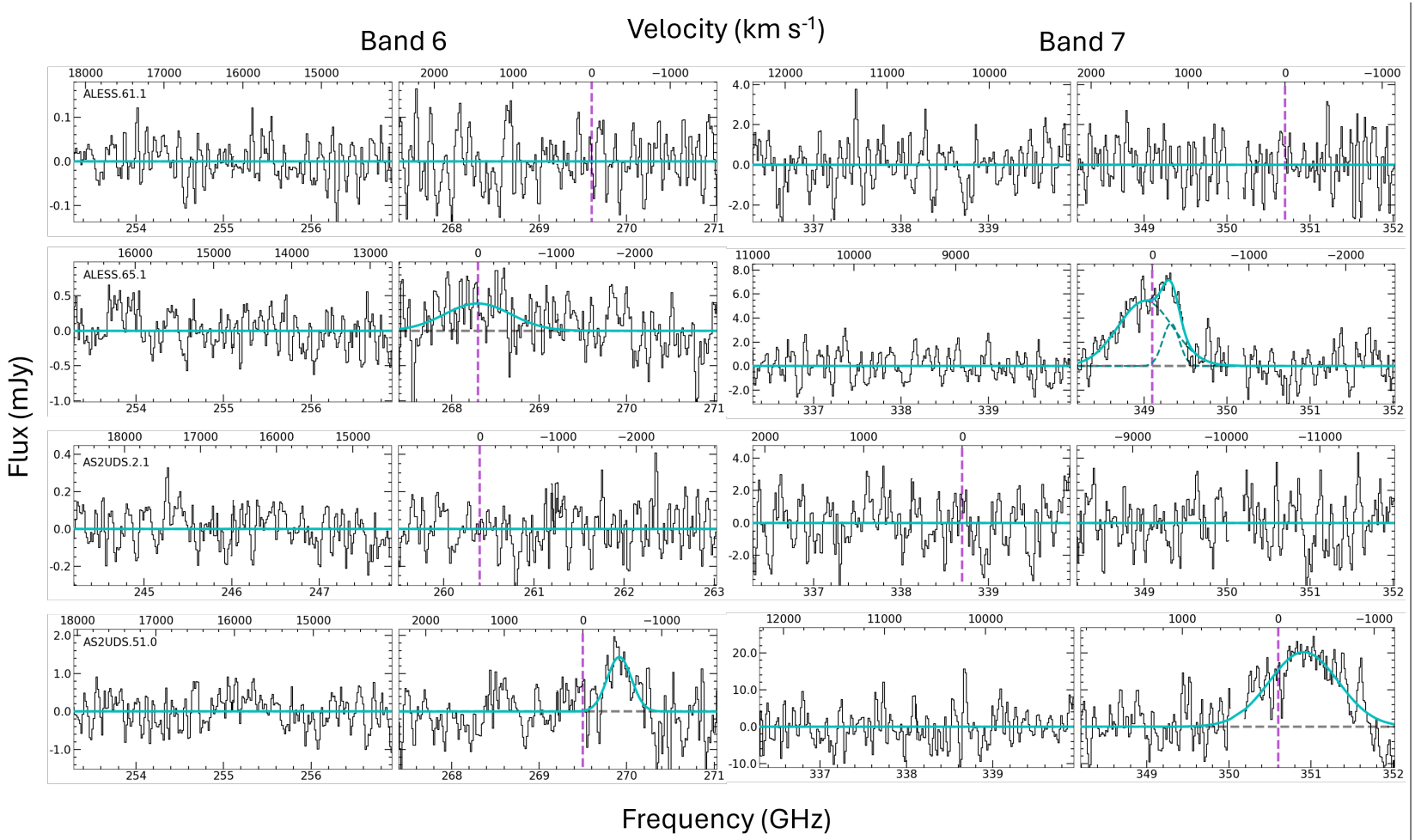

Figure 2.5: Extracted continuum subtracted spectra including Gaussian fits for all targeted sources, plus AS2UDS 0109.1. The black line shows the spectra extracted for each source without any binning. The purple dashed line shows the expected frequency for the lines in each sideband assuming the original detection from Cooke et al. (2018) and Swinbank et al. (2012) are [C II] at $z = 4.5$, and the grey dashed line shows the zero level of the spectrum. The cyan solid line shows the result of the Gaussian fitting. The Gaussian is only shown if the line has an SNR > 3. For ALESS 65.1 the blue dashed lines show the two components of the double Gaussian used to fit this line.

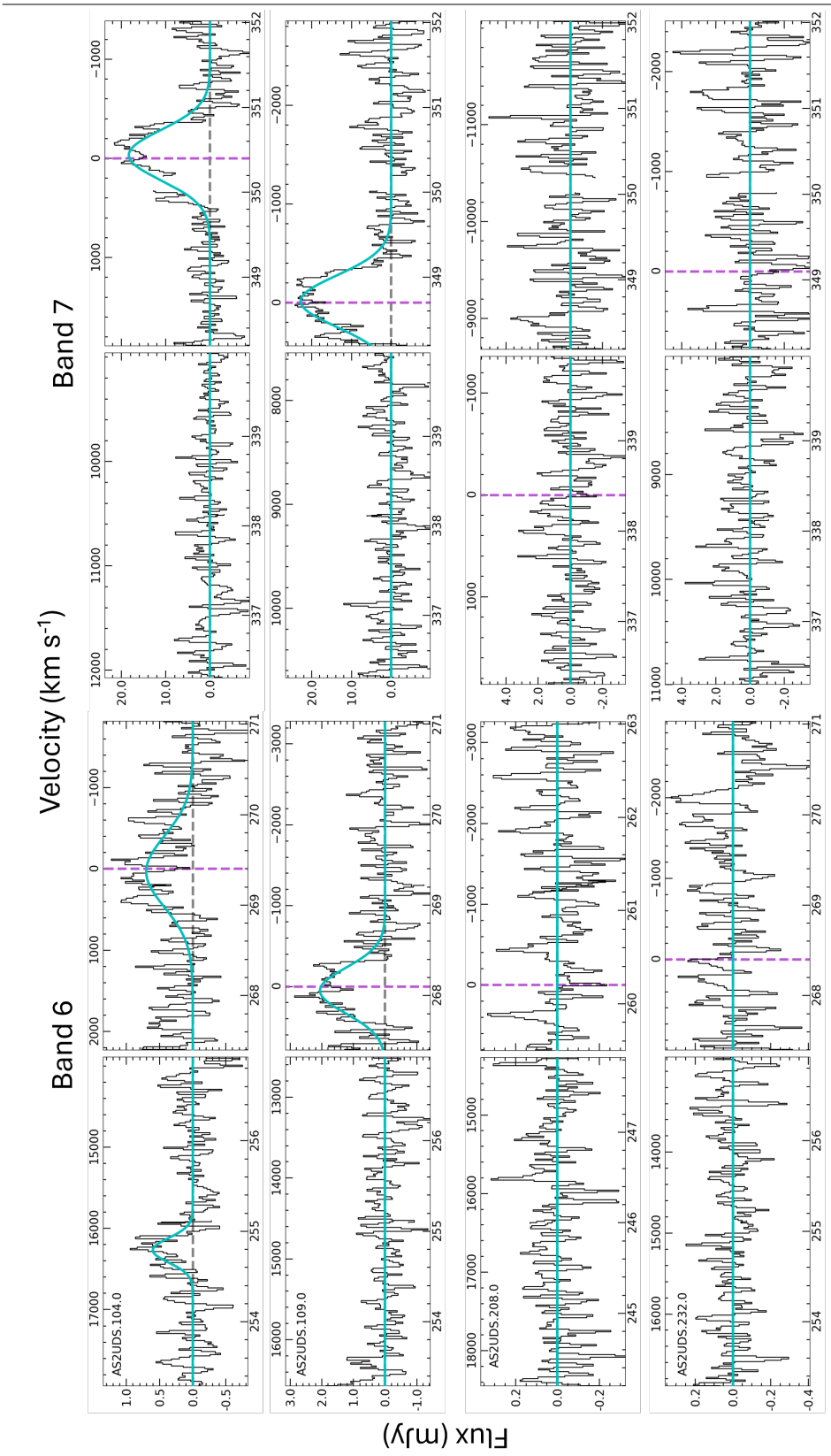

Figure 2.5 (Continued)

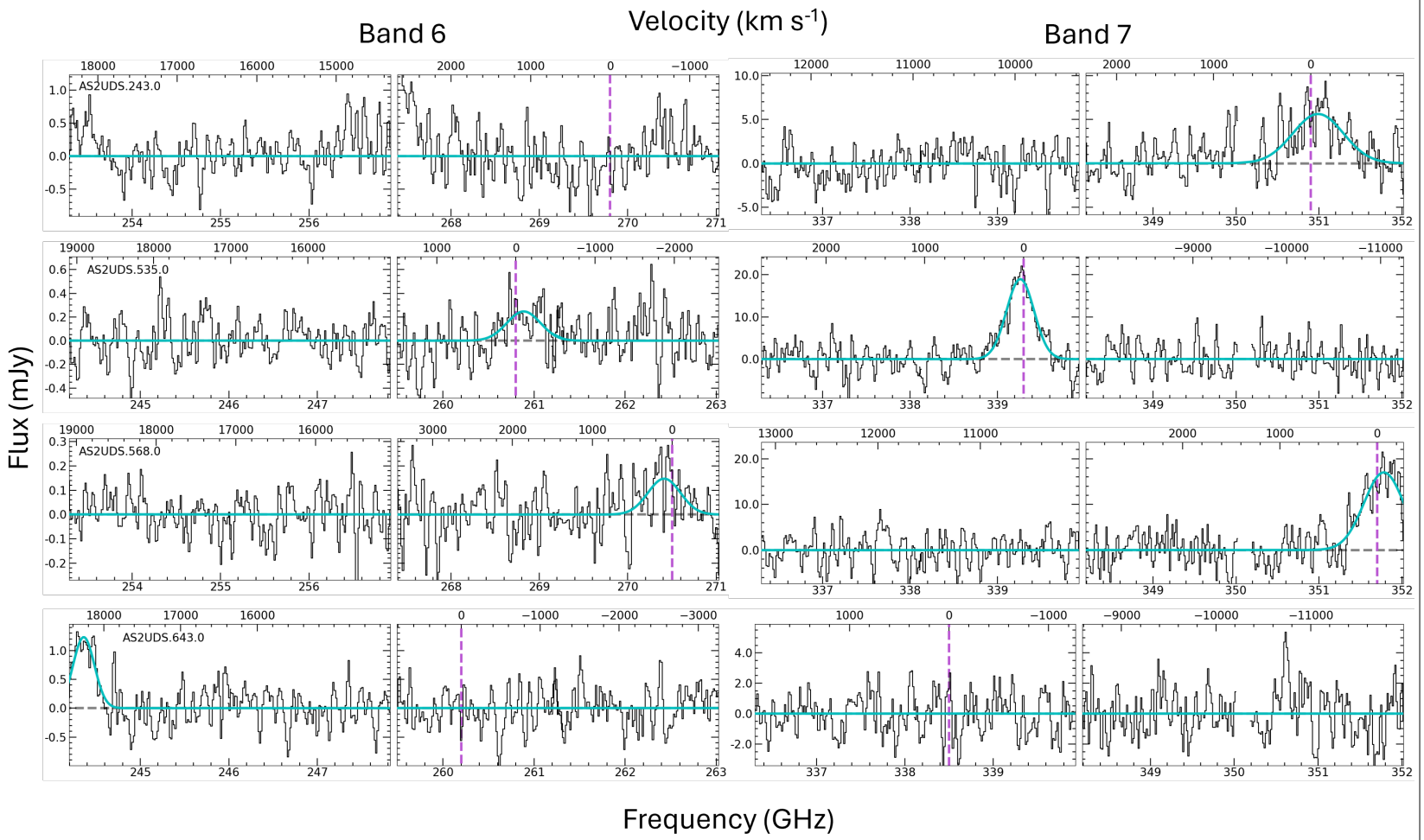

Figure 2.5 (Continued)

2.7 Comparison with previous line measurements

Of the lines that are detected, we detect all [C II] lines at a SNR> 6 and [N II] at SNR> 4. A lower detection threshold (SNR > 3) than previous studies (Swinbank et al., 2012; Cooke et al., 2018) is used to classify a positive line detection, as we have prior information on the spatial positions and redshifts of these sources.

Both [C II] line fluxes and FWHMs that we measured for the AS2UDS sources are higher than were measured by Cooke et al. (2018) (Figure 2.6). The difference is likely due to the different beam sizes of the data: our beams are typically ~ 0.4–0.5 arcsec compared to 0.15–0.3 arcsec for Cooke et al. (2018) meaning that it is possible for Cooke et al. (2018) to have 'resolved out' some emission by observing in an array configuration that is only sensitive to the most compact emission.

Figure 2.6 shows the ratios of our fluxes to ones from Cooke et al. (2018) as well as the ratios of the FWHMs, showing no significant correlation between the two. It is worth noting that out of all of the Cooke et al. (2018) sources, we detect only those with the brightest [C II] emission; the undetected sources all had an initial detection significance of $< 10\sigma$. This result could help future untargeted surveys in determining false positive rates when searching for line emission in ALMA and interferometric data. We find no significant trends between the SNR of a line and the ratio of it's FWHM or [C II] flux.

For the two ALESS sources, while the flux of the detected galaxy (ALESS 65.1) is comparable to that measured in Swinbank et al. (2012) the FWHM we observe is substantially greater. Our higher spectral resolution and sensitivities allowing us to resolve the double-Gaussian components of the line could be partially responsible for the difference in FWHM. However, we note that fitting a single gaussian still yields a FWHM of 684 km s^{-1}, $\sim 1.4\times$ wider than the FWHM measured in Swinbank et al. (2012). This could be exacerbated by our lack of spectral binning: it is possible that binning caused emission at the edges of the line to be averaged out, causing the line to appear narrower.

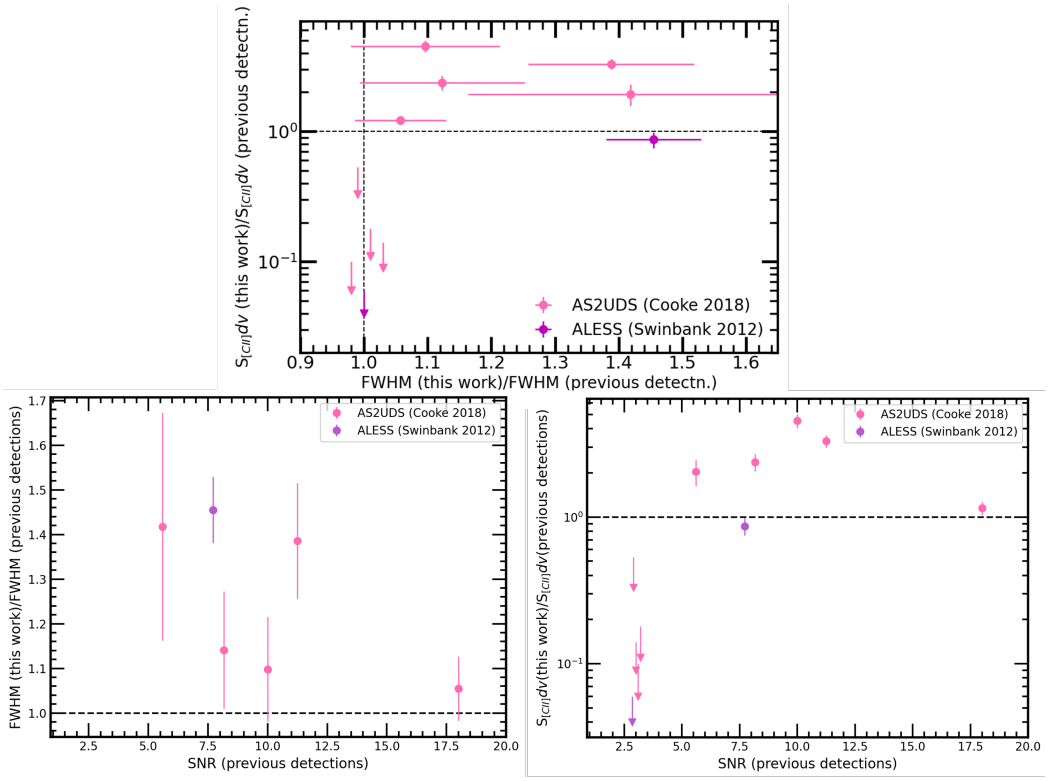

Figure 2.6: (*Top:*) Ratio of the flux measured in our observations of the [C II] line to that previously measured by Cooke et al. (2018) and Swinbank et al. (2012) against the ratio of FWHM between detections. (*Lower Left:*) Ratio of the FWHM of the new measurements to the old ones against the SNR measured in previous detections. (*Lower Right:*) Ratio of the [C II] flux of the new measurements to the old ones against the SNR measured in previous detections. For the AS2UDS sources all of our observations have higher integrated fluxes than Cooke et al. (2018), which is likely due to the smaller beam size in the Cooke et al. (2018) observations resolving out some flux. The measurement for ALESS 65.1 is consistent with that from Swinbank et al. (2012) in flux but with a broader FWHM. We fit a double Gaussian to ALESS 65.1 but this does not account for the full difference. We theorise that our higher spectral resolution and sensitivity allow us to resolve the double Gaussian component of this line, creating the discrepancy. $S_{[\mathrm{CII}]}dv$ is the integrated flux of the emission line measured in $\mathrm{mJy\,km\,s^{-1}}$. Upper limits are 3σ and are scattered around 1 on the x-axis for visibility. As no line is measured for these sources we assume them to have a FWHM equal to that in their previous detection. We find no significant trends between the SNR of a line and the ratio of its FWHM or [C II] flux, i.e. the width of a line has no effect on its likelihood of being spurious.

2.8 Ancillary data

For SED fitting (Section 2.10) and the interpretation of individual galaxies we complement our measurements with additional photometry. For the AS2UDS sources we use data from Cooke et al. (2018), Stach et al. (2019), the UDS DR11 catalog (O. Almaini et al., in preparation) and the UDS20 radio catalogue (V. Arumugam et al., in preparation; see also Arumugam 2013). For the two ALESS sources additional photometry is from Swinbank et al. (2012); Wardlow et al. (2011); Hodge et al. (2013); Simpson et al. (2014) and Birkin et al. (2021) in the optical and infrared and Biggs et al. (2011) for the 1.4GHz data.

2.9 Redshift determination

Of the 12 galaxies observed, six exhibit lines in both the Band 6 and 7 cubes at the frequencies expected for [N II] and [C II] respectively. These are ALESS 65.1, AS2UDS 0051.0, AS2UDS 0104.0, AS2UDS 0109.0, AS2UDS 0535.0 and AS2UDS 0568.0. Therefore, we confirm the redshifts of these galaxies as those determined by Cooke et al. (2018) and Swinbank et al. (2012). The redshifts do not change when measured from our [C II] detections. Additionally we detect [C II] and [N II] in AS2UDS 0109.1 which is within the field of view of the data targeting AS2UDS 109.0, although it is at the edge of the cubes. More discussion of this source can be found in Section 2.11 and its redshift is confirmed as that from Cooke et al. (2018).

In one galaxy (AS2UDS 0643.0) there is a line only in the Band 6 cube, at a frequency offset from that which we expected for [N II] 205 μm (see Figure 2.5). We suggest this line is most likely [N II]205μm which places this source at $z = 4.98$. AS2UDS 0243.0 has a line in the Band 7 cube at the same frequency as in Cooke et al. (2018). However, the photometric results suggest that this source is at $z < 2$, since it is detected at 1.4 GHz, and we re-identify the line as CO(8-7) as suggested by Cooke et al. (2018), giving AS2UDS 0243.0 a resdshift of 1.63 and excluding it from analysis of the [C II]/[N II]line ratios (Chapter 3).

A more detailed discussion of each galaxy is presented in Section 2.11. Redshifts are used for IR-luminosity calculations during SED fitting (Section 2.10) and line luminosities (Table 2.1) used in analyses in Chapter 3.

2.10 SED fitting

Our data provide new constraints on both the redshifts of the SMGs (from the ALMA spectroscopy; see Section 2.7) and the SEDs from the new Band 6 (260 GHz; $\sim 1150\,\mu$m) continuum photometry (Section 2.5). Thus, we use this data to explore the SEDs of the sources for which we have measured the redshift. To measure the IR-luminosity ($L_{\rm IR}$) of these galaxies the average ALESS template from da Cunha et al. (2015) redshifted to our measured redshifts and is normalised to our measured Band 7 (860μm) continuum photometry. In all cases the Band 6 photometric point that we measured in Section 2.6 is consistent with the model SED. An example of the template fit is shown in Figure 2.7.

For AS2UDS 0109.1 the 870μm measurement from Stach et al. (2019) was used instead of the photometry measured from our data. This is due to the source residing in the outer regions of the data cube where noise is high due to primary beam correction; AS2UDS 0109.1 is therefore not detected at the $> 3\sigma$ level in our data. As such the photometry from Stach et al. (2019) is of a higher fidelity and was preferred for SED fitting of this SMG.

The $L_{\rm IR}$ (rest frame 8-1000μm) for sources with a [C II] and [N II] detection are included in Table 2.1 alongside derived SFRs obtained using the Kennicutt (1998) relation. The $L_{\rm IR}$ calculated in this section are used for investigation of the [C II] deficit in Chapter 3.

2.11 A discussion of individual galaxies

In this section we will discuss the individual properties of each galaxy, including any multiwavelength data available and specifics of the processing that was done to each source in order to extract all the necessary data. We discuss and

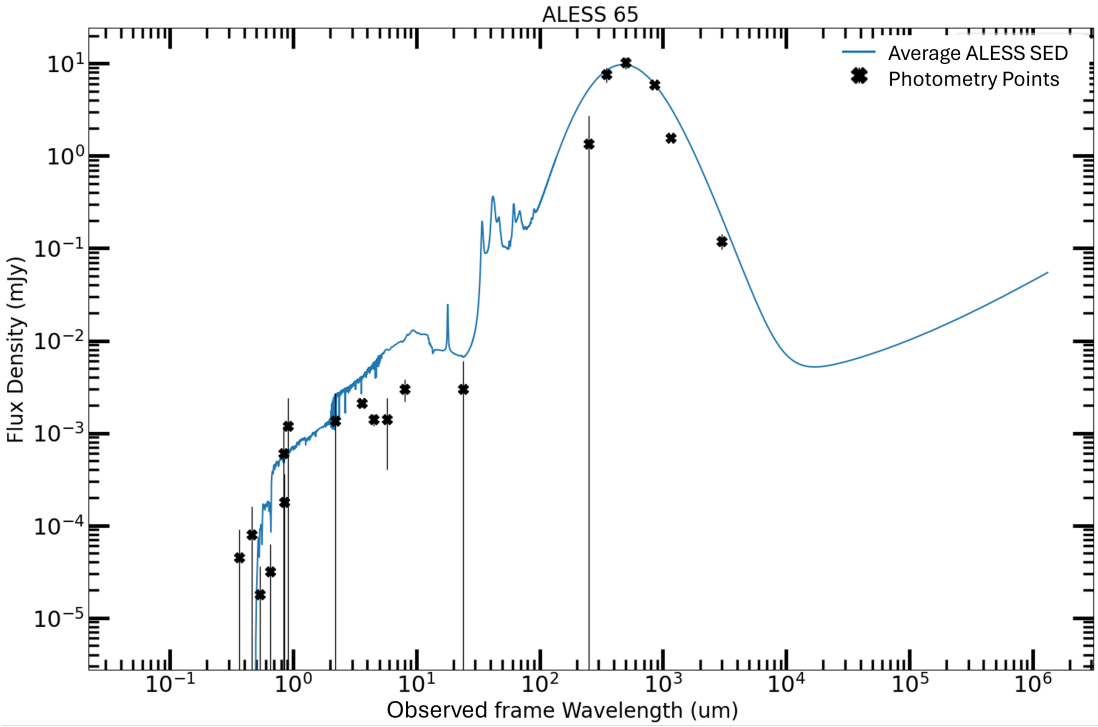

Figure 2.7: Example of the SED template used (average of the ALESS sample da Cunha et al. 2015) which has been normalised to the observed frame 860 μm photometry point from our Band 7 observations for ALESS 65.1 with other archival photometry plotted to assess the suitability of the template for each galaxy. Points with error bars reaching down to the bottom of the plot are upper limits there the limit is at the top of the upper error bar.

justify emission line identities for sources which were not at the expected redshift. Cutouts of the multiwavelength data for all AS2UDS sources are shown in Figure 2.8.

2.11.1 ALESS 61.1

Swinbank et al. (2012) detect $2.5 \pm 0.4\,\mathrm{Jy\,km\,s^{-1}}$ (6.3σ) at 350.726 GHz, assumed to be [C II], which was confirmed by Gullberg et al. (2018) with a detection of $4.6 \pm 1.7\,\mathrm{Jy\,km\,s^{-1}}$ but at low SNR (2.7). Birkin et al. (2021) detect a CO(4-3) line which confirms this galaxy as being at $z \sim 4.4$, but it is offset by $\sim 900\,\mathrm{km\,s^{-1}}$ suggesting a redshift of 4.404 as opposed to 4.419 in Swinbank et al. (2012). After extracting from regions centred on the detections in all of the above studies we are unable to recover any spectral line emission from this source in either band, including after tapering the data and re-analysing. As such we conclude that the original line detection was spurious and Birkin et al. (2021) detected a line by chance in their data. We measure continuum fluxes of 2.51 ± 0.051 mJy in Band 6 and 4.44 ± 0.2 mJy in Band 7 (in agreement with measurements from Swinbank et al. (2012)). ALESS 61.1 is undetected at 1.4 GHz (Biggs et al., 2011) but has a 24 μm counterpart that is visible in the near-IR (Swinbank et al., 2012).

2.11.2 ALESS 65.1

Swinbank et al. (2012) detect a [C II] flux of $5.4 \pm 0.7\,\mathrm{Jy\,km\,s^{-1}}$ (7.7σ) at 349.073 GHz which was confirmed by Gullberg et al. (2018) with a $4.9 \pm 1.0\,\mathrm{Jy\,km\,s^{-1}}$ detection. We detect $5.09 \pm 0.21\,\mathrm{Jy\,km\,s^{-1}}$ at 349.15GHz in agreement with their results, as well as an [N II] detection of $0.41 \pm 0.08\,\mathrm{Jy\,km\,s^{-1}}$ (5.1σ) at 268.3 GHz. We detect continuum fluxes of 1.56 ± 0.033 mJy in Band 6 and 5.93 ± 0.29 mJy in Band 7 (higher than the Swinbank et al. 2012 detection; see discussion in Section 2.7 for proposed reasons for discrepancies in measurements.) ALESS 65.1 is undetected at 1.4 GHz (Biggs et al., 2011) and has no optical or near-IR counterparts, with only weak detections in SPIRE imaging (Swinbank et al., 2012).

2.11.3 AS2UDS 0002.1

Cooke et al. (2018) detect flux of $1.3 \pm 0.3\,\mathrm{Jy\,km\,s^{-1}}$ (8.7σ) at 338.707 GHz, assumed to be [C II], but report a B-band detection within 1" of the 870 μm emission which may be contaminating the optical/near-IR photometry. We do not detect any line flux for this source in either band and so conclude that the previous "line" detection was spurious. We do detect continuum fluxes of 7.16 ± 0.38 mJy in Band 6 and 9.78 ± 0.35 mJy (higher than that detected in Cooke et al. 2018, who measure 7.4 ± 0.5 mJy). AS2UDS 0002.1 is undetected at 1.4 GHz and has a photometric redshift of 3.35.

2.11.4 AS2UDS 0051.0

Cooke et al. (2018) detect a [C II] flux of $4.0 \pm 0.4\,\mathrm{Jy\,km\,s^{-1}}$ (10.5σ) at 350.571 GHz which is confirmed in Gullberg et al. (2018) with a $6.8 \pm 1.8\,\mathrm{Jy\,km\,s^{-1}}$ detection. We further confirm this with a $19.69 \pm 0.96\,\mathrm{Jy\,km\,s^{-1}}$ detection at 350.91GHz and an [N II] detection of $0.55 \pm 0.1\,\mathrm{Jy\,km\,s^{-1}}$ (5.5σ) at 269.9 GHz. AS2UDS 0051.0 consists of two connected components in both the Band 6 and Band 7 data (Figure 2.2). This requires careful extraction to ensure that the fluxes measured in all tracers ([C II], [N II] and continuum in both bands) are tracing the same regions of the source. Once all emission has been properly accounted for, we detect continuum fluxes of 4.85 ± 0.33 mJy in Band 6 and 6.39 ± 0.93 mJy in Band 7 (in agreement with measurements from Cooke et al. 2018). AS2UDS 0051.0 has no optical or near-IR counterparts and is undetected in the radio.

2.11.5 AS2UDS 0104.0

Cooke et al. (2018) detect a [C II] flux $4.9 \pm 0.6\,\mathrm{Jy\,km\,s^{-1}}$ (17.3σ) at 350.447 GHz. We detect $12.03 \pm 0.77\,\mathrm{Jy\,km\,s^{-1}}$ of emission at 350.44 GHz, confirming the previous detection. We detect [N II] with a flux of of $0.77 \pm 0.07\,\mathrm{Jy\,km\,s^{-1}}$ (11σ) at 269.3 GHz. We also report the detection of another line in addition to the [N II] 205 line in the Band 6 data when using an unconvolved extraction region, which is at the correct frequency to be CO(12-11). However, when the region is convolved with a region $0.5\times$ the beam during our extraction pipeline the noise

added pushes it below the detection limit (i.e. it becomes $< 3\sigma$). We detect continuum fluxes of 4.37 ± 0.19 mJy in Band 6 and 6.07 ± 0.3 mJy in Band 7 (in agreement with the Cooke et al. (2018) detection). It has no optical or *Spizer* coverage and is undetected in K-band and radio.

2.11.6 AS2UDS 0109.0

Cooke et al. (2018) detect a [C II] flux of 4.5 ± 0.4 (11.3σ) at 348.715 GHz. We confirm this with a 15.99 ± 0.68 Jy km s^{-1} detection at 348.72 GHz. In Band 6 we detect [N II] at 1.44 ± 0.09 Jy km s^{-1} (16σ) at 268.1 GHz. We detect continuum fluxes of 5.51 ± 0.22 mJy in Band 6 and 6.77 ± 0.55 mJy in Band 7 (in agreement with the Cooke et al. (2018) detection). AS2UDS 0109.0 has a K-band and 4.5 μm detection but no 1.4 GHz detection.

2.11.7 AS2UDS 0208.0

Cooke et al. (2018) detect 2.2 ± 0.3 Jy km s^{-1} (8.1σ) at 338.445GHz, assumed to be [C II], but report that it lies within 1" of a bright B-band source with z_{phot}=2.5 ± 0.2 which may be lensing the source. We are unable to detect any emission lines in either of the observed bands and conclude that the original detection is likely spurious. We do detect this source in the continuum with a measurement of 2.41 ± 0.15 mJy in Band 6 and 4.27 ± 0.21 in Band 7 (in agreement with the measurement from Cooke et al. 2018). The SMG has no optical counterpart and is undetected at 1.4 GHz.

2.11.8 AS2UDS 0232.0

Cooke et al. (2018) detect 0.9 ± 0.2 Jy km s^{-1} (7.2σ) at 349.140 GHz, assumed to be [C II], but we are also unable to recover any emission lines for this source and conclude that the original detection was spurious. We detect continuum fluxes of 3.72 ± 0.19 mJy in Band 6 and 5.48 ± 0.27 mJy in Band 7 which is consistent with the measurement from Cooke et al. (2018). AS2UDS 0232.0 has no optical

or near-IR coverage and is undetected at 1.4 GHz. It is detected at 4.5 μm and 24 μm.

2.11.9 AS2UDS 0243.0

Cooke et al. (2018) detect 3.2 $\pm$ 0.4 Jy km s^{-1} (15.5σ) at 350.939GHz which is assumed to be [C II]. AS2UDS 0243.0 has a derived photometric redshift of z=1.58$\pm$0.05 suggesting the detected line may CO(8–7) at z=1.63 $\pm$ 0.01. We confirm this detection of 4.55 $\pm$ 0.49 Jy km s^{-1} at 350.99 GHz (9.3σ) and due to lack of [N II] detection in Band 6 agree with their conclusion that this source lies at z=1.63. AS2UDS 0243.0 is detected in B-band and at 1.4 GHz which further supports the conclusion of it residing at $z < 2$. We find continuum measurements of 2.83 $\pm$ 0.15 mJy in Band 6 and 4.60 $\pm$ 0.27 mJy in Band 7 (consistent with Cooke et al. 2018).

2.11.10 AS2UDS 0535.0

Cooke et al. (2018) detect a 3.6 $\pm$ 0.2 Jy km s^{-1} (12.1σ) line at 339.301GHz. We confirm this by detecting a 5.82 $\pm$ 0.28 Jy km s^{-1} line at 339.26 GHz. We find an [N II] detection of 0.13 $\pm$ 0.03 Jy km s^{-1} (4.3σ) at 260.9 GHz. We measure continuum photometry of 1.15 $\pm$ 0.092 mJy in Band 6 and 2.06 $\pm$ 0.38 mJy in Band 7 (consistent with the measurement in Cooke et al. 2018). This source has a B-band detection and photometric redshift of $z = 0.80 \pm 0.03$ with a secondary peak at 4.63. A lack of mid-IR and radio detection is what led this source to initially be identified as a $z \sim 4.5$ [C II] emitter and our [N II] detection (Table 2.2) confirms this.

2.11.11 AS2UDS 0568.0

Cooke et al. (2018) detect a [C II] flux of 2.8 $\pm$ 0.5 Jy km s^{-1} (10.3σ) at 351.701GHz. We confirm this detection at 9.37 $\pm$ 0.58 Jy km s^{-1} at 351.78 GHz, as well as an [N II] detection of 0.08 $\pm$ 0.02 Jy km s^{-1} (4σ) at 270.4 GHz. We detect continuum fluxes of 1.27 $\pm$ 0.072 mJy in Band 6 and 1.76 $\pm$ 0.42 mJy in Band 7 (in agreement

with the measurement from Cooke et al. 2018). AS2UDS 0568.0 has no optical or near-IR detections, and is undetected at 1.4 GHz.

2.11.12 AS2UDS 0643.0

Cooke et al. (2018) detect $1.5 \pm 0.4\,\mathrm{Jy\,km\,s^{-1}}$ (7.2σ) at 338.512 GHz, assumed to be [C II], with a photometric redshift of z=$4.44^{+0.62}_{-1.08}$ (Cooke et al., 2018). There are also foreground sources at $z < 4$ within 1"–2" of AS2UDS 0643.0. We cannot confirm this line detection, recovering no lines in our Band 7 data, however we detect a line $0.43 \pm 0.05\,\mathrm{Jy\,km\,s^{-1}}$ in Band 6 at 244.4 GHz, which is significantly ($\sim$18200 $\mathrm{km\,s^{-1}}$) offset from the frequency expected for [N II] 205 μm. Possible identities for this line are:
- CO(9-8) at z=3.24 (no lines would be visible in B7)
- CO(10-9) at z=3.715 (no lines would be visible in B7)
- CO(11-10) at z=4.18 (no lines would be visible in B7)
- CO(12-11) at z=4.65 (no lines would be visible in B7, CII just off the end)
- [N II] 205 at z=4.98 (no lines would be visible in B7)

Given the relative brightness of these lines and the previous photometric information (z_{phot}=$4.44^{+0.62}_{-1.08}$ Cooke et al. 2018) available we conclude that this line is most likely [N II] 205 μm at $z = 4.98$. We would not detect [C II] in Band 7 in this case as it would be redshifted out of the spectral windows. We detect continuum fluxes of 1.39 ± 0.15 mJy in Band 6 and 2.27 ± 0.19 mJy in Band 7 (in agreement with the measurement from Cooke et al. 2018).

2.12 Untargeted sources

While anylysing the data, six additional sources were serendipitously identified: these consist of three line emitters AS2UDS 0109.1, 243B and 568B, and four continuum identified sources; AS2UDS 0002.0, 535C1 and 535C2. They have the following positional matches in The NASA Extragalactic Database (NED)[1]:

[1]The NASA/IPAC Extragalactic Database (NED) is funded by the National Aeronautics and Space Administration and operated by the California Institute of Technology

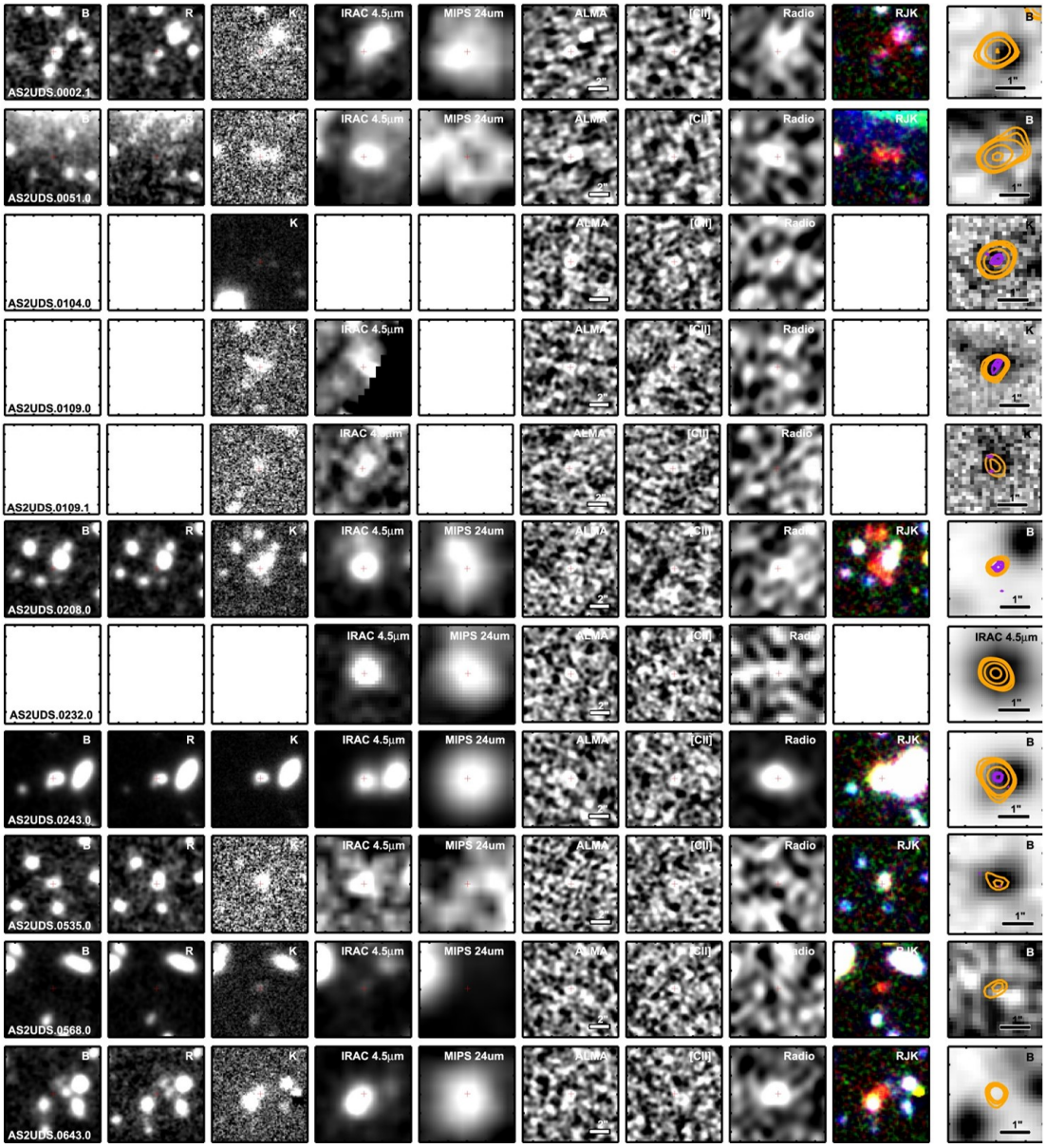

Figure 2.8: Multiwavelength data for all targeted AS2UDS sources as well as AS2UDS 0109.1 which we also detect. The first nine thumbnails are $10''\times10''$centred on the source of the submillimetre emission (red cross). The last column of thumbnails is $3''\times3''$with overlaid contours at high (purple, $\sim 0.15''$, where available) and low (orange, $\sim 0.5''$, tapered) resolution of the ALMA 870 μm flux at 3, 4, 5, 10 and 20σ.

- We detect AS2UDS 0002.0 at 02h18m24.139s -05d22m55.254s which has a measured $z_{phot} = 3.335^{+0.07}_{-0.06}$ (Dudzevičiūtė et al., 2020). AS2UDS 0002.0 is within the field of view for AS2UDS 0002.0 in both bands. We measure continuum fluxes of 10.45 ± 0.9 mJy in Band 7 (344GHz) and 7.19 ± 0.7 mJy in Band 6 (254GHz). We do not find any line detections for this source in our data. AS2UDS 0002.0 has a plethora of multiwavelength data with detections from the B-band through to 1.4 GHz, which are presented in Dudzevičiūtė et al. (2020). Given this redshift we would expect to see [N II] 205 μmat 337 GHz but it is possible that the uncertainty on the z_{phot} means that it is redshifted off the side of our observations (as when the redshift is at it's upper limit).

- We detect AS2UDS 0109.1 at 02h16m19.050s -05d22m23.339s. AS2UDS 0109.1 is within the field of view of AS2UDS 0109.0 in both Bands 6 and 7, and we detect continuum fluxes of 6.57 ± 2.6 mJy in Band 7 (344GHz) and 1.44 ± 0.2 mJy in Band 6 (262 GHz). Cooke et al. (2018) report a tentative 5.3σ detection of a potential [C II] line at 348.6 GHz which would place AS2UDS 0109.1 at the same redshift as AS2UDS 109.0 ($z = 4.451$). We confirm this detection at 6.7σ. However, since the source resides at the edge of the Band 7 field of view it is subject to a high noise level leading to large uncertainties. As such, we use the value of 870 μmflux measured in Cooke et al. (2018). We search for a corresponding [N II] line which should reside at 268.0 GHz at $z = 4.451$ and find a 0.13 ± 0.03 Jy km s^{-1} (3.9σ) detection confirming this source is at the same redshift at AS2UDS 109.0. This source is thus included in our analysis in Chapter 3. AS2UDS 0109.1 has no optical coverage, but is detected in K-band and IRAC, and undetected at 1.4 GHz.

- We detect a source in the continuum data for AS2UDS 535.0 which we refer to as 535C1 at 02h18m12.719s -5d30m23.778s. The closest source to this found in NED is SSTSL2 J021812.72-053023.7 (UKIDDS ID 003402) at a 0.36 arcsec separation, with a photometric redshift of $z = 3.05$ (Williams et al., 2009). We detect continuum fluxes of 3.79 ± 0.90mJy in Band 7 (344GHz) and 0.77 ± 0.09 mJy in Band 6 (254GHz). This source is detected in all IRAC channels and is included in a catalogue of quiescent galaxies

(Williams et al., 2009). The addition of our far-IR measurements indicate that this source may have a large dust mas and may have its colour reddened by this rather than this being a reflection of its stellar population and thus star-formation activity. The steepness of a decline in measured fluxes between Band 7 and 6 suggests we are measuring the Rayleigh-Jeans tail of the dust SED which would be redshifted to these frequencies at $z \sim 3$

- We detect a second source in the continuum data for AS2UDS 535.0 which we refer to as 535C2 at a position of 02h18m13.453s -05d30m42.810s. The closest source to this found in NED is SSTSL2 J021813.40-053042.8 (UKIDDS ID 002904) at a 0.54 arcsec separation, with a photometric redshift of $z = 0.66$ (Williams et al., 2009). We detect continuum fluxes of 1.87 ± 0.39mJy in Band 6 only (254GHz). This source is not in the field of view of the Band 7 data so we measure no continuum flux in Band 7. Like 535C1, our far-IR detection in combination with IRAC detections indicate that this source may be dusty and masquerading as a red-quiescent galaxy, although without the Band 7 photometry it is not possible to assess the behaviour of the dust SED in this source.

- We detect a line emitter in the data cube for AS2UDS 0243.0 which we refer to as 243B at a position of 02h16m17.649s -05d07m18.617s. We identify this source in NED as WISEA J021617.75-050718.6 (UKIDDS ID 046739) at a 0.78 arcsec separation with a measured photometric redshift of $z = 0.380$ Williams et al. (2009). We detect continuum fluxes of 1.25 ± 0.68 mJy in Band 7 (344 GHz) and 0.59 ± 0.12 mJy in Band 6 (262 GHz). We also detect line emission at a 23 sigma level of 1.29 ± 0.06 mJy at 256.6 GHz. This would align with being CO(3-2) at $z = 0.3475$, constraining this source's redshift. Our line detection is shown in Figure 2.9 (top). This source was identified in Chen et al. (2016) as a multiple counterpart for AS2UDS 0243.0 however here we spectroscopically confirm its redshift and thus that this source is not physically associated with AS2UDS 0243.0 and is simply a line-of-sight alignment.

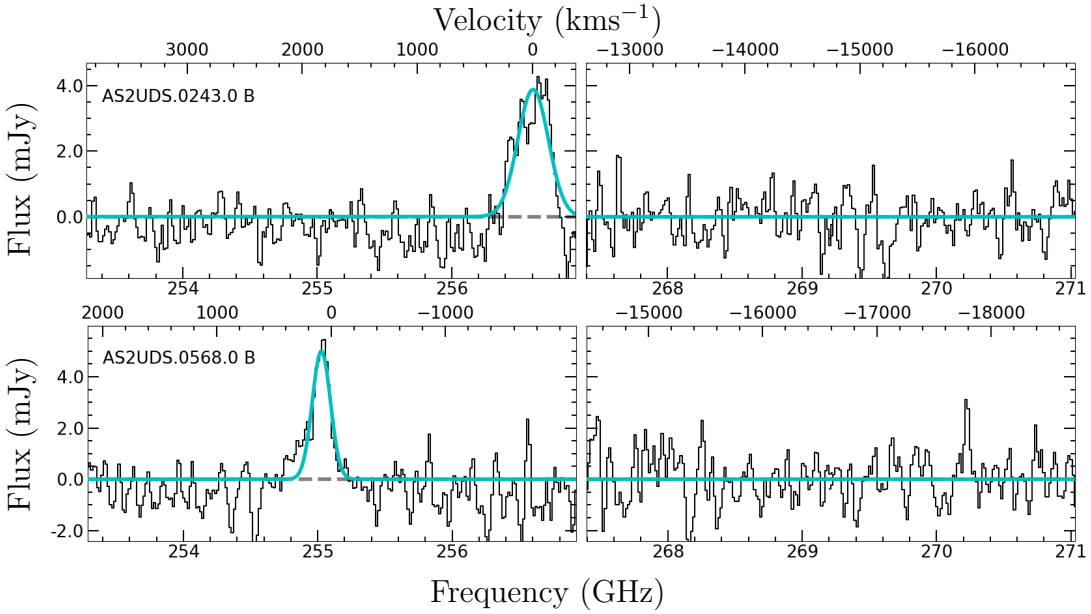

Figure 2.9: The emission lines detected in the additional sources 243B (*top*) and 568B (*bottom*). Extracted, continuum-subtracted, spectra are shown black, with the zero-level shown by the gray dashed line, and fitted single gaussian in cyan.

- 568B: 02h18m40.452s -05d20m03.248s We identify this source as WISEA J021840.39-052002.6 (UKIDDS ID 022596) at a 0.24 arcsec separation with a spectroscopic redshift of $z = 0.9300$ Espino-Briones et al. (2022). We detect continuum fluxes of 2.69 ± 1.16 mJy in Band 7 (344 GHz) and 1.22 ± 0.17 mJy on Band 6 (262 GHz). We also detect line emission at a 11sigma level of 1.00 ± 0.09 mJy at 255.0 GHz. This corresponds to [CI] 609 μm at $z = 0.9300$. Our line detection is shown in Figure 2.9 (bottom).

2.13 Conclusions

Here we present new observations in Band 6 and 7 of 12 SMGs, initially thought to be at $z \sim 4.5$ due to serendipitous detections of the [C II] 158 μm line in their data cubes (Swinbank et al., 2012; Cooke et al., 2018). Our new data aims to confirm the [C II] detection with deeper data, and provide complementary [N II] 205 μm data from the Band 6 observations. We have undertaken dedicated imaging of the

new ALMA data in order to optimise recovered flux, finding that six out of the 12 targeted SMGs are at the originally predicted redshift with detections of both [C II] and [N II], as well as recovering detections of both lines for one serendipitous source. We created a custom region generation algorithm to extract the flux from our images for further analysis in Chapter 3. We find that our detected fluxes are generally higher than those measured in the discovery papers, owing to flux being resolved out in the original higher resolution data.

We fit SEDs to the detected sources, informing redshift determinations for sources with line detections that do not align with being $z \sim 4.5$ [C II] and find the likely identity of these emission lines. We use the SEDs to calculate IR luminosities which we use for analysis in Chapter 3.

We re-image the detected $z \sim 4.5$ for increased spatial resolution in order to perform kinematic analysis in Chapter 4 finding a $\sim 20\%$ reduction in beam size between ROBUST values of 2.0 and 0.0.

This Chapter concludes with having a sample of seven SMGs which we go onto use to investigate the complex nature of the [C II] line in Chapter 3 and perform kinematic analysis in Chapter 4. We detect six serendipitous sources, two of which are SMGs in the AS2UDS data set and the other four are unrelated galaxies for which we detect line and/or continuum emission.

Chapter 3

Integrated [C II] and [N II] properties in $z \sim 4.5$ SMGs

3.1 Introduction

In this chapter we combine [C II] measurements with observations of the [N II] 205 μm line in the seven SMGs identified to be at $z \sim 4.5$ in Chapter 2. These sources already have multiwavelength observations, including far-infrared photometry and some with identified optical/near-IR counterparts.

The [C II] deficit is observed at high IR-luminosities as described in Section 1.4.3 and is a phenomenon reproduced in simulations across redshifts from 0–8 (Liang et al., 2024), which affects its use as a tracer of star formation and potentially the underestimation of SFR at high $L_{\rm IR}$. [N II] 205μm has an ionisation energy of 14.5 eV and it can therefore only originate from ionised regions of the ISM. Thus, by combining [C II] measurements with [N II] 205 μm observations it is possible to determine the fraction of [C II] that originates from ionised regions of the ISM as compared to photodissociation regions (PDRs; Oberst et al. 2006; Decarli et al. 2014).

The fraction of [C II] that is emitted from different regions of the ISM can provide insights into what mechanisms may be driving the [C II] deficit by determining if it preferentially occurs in galaxies with a higher or lower $[\mathrm{C\,II}]_{PDR}$

fraction.

This chapter is set out as follows: in Section 3.2 we assess the behaviour of our sources in relation to their [C II]/$L_{\rm FIR}$ to assess how deficited they are in comparison to other sources, and search for a similar deficit in the [N II] emission. We then constrain the [C II] luminosity function using our detections in Section 3.3. In Section 3.4 we determine the percentage of the [C II] emission originating from PDRs vs the ionised ISM and then in Section 3.5 we search for correlation between the amount of [C II] coming from PDRs and the strength of the [C II] deficit. In Section 3.6 we present a correction that can be made to an observed [C II] luminosity to account for the deficit using its observed [N II] luminosity, allowing for a more accurate [C II] derived SFR. We present our conclusions in Section 3.7.

3.2 [C II] deficit

The targeted SMGs all have $L_{\rm IR}> 10^{12}\,{\rm L}_{\odot}$ (Table 2.1) – within the luminosity range at which the [C II] deficit becomes apparent both at low redshift (e.g Stacey et al. 1991; Malhotra et al. 2001; Luhman et al. 2003; Díaz-Santos et al. 2017) and at $z \sim 5$ (e.g. Iono et al. 2006; Wang et al. 2013a; Rawle et al. 2014). Figure 3.1 shows that some of these $z \sim 4.5$ SMGs also have fainter [C II] emission than the lower luminosity trend lines, although several of the targets are broadly consistent with lower-luminosity local galaxies. Other high-redshift SMGs (Reuter et al., 2020; Cunningham et al., 2020) show similar behaviour. Note that the points from Díaz-Santos et al. (2017) in Figure 3.1 were originally measured as [C II]/$L_{\rm FIR}$ where $L_{\rm FIR}$ is measured between 42.5–122.5μm. Here we assume $L_{\rm FIR}$ to be $\sim 0.5\times$ the $L_{\rm IR}$ according to Dale & Helou (2002) and adjust the points accordingly to display against our data.

We next probe whether the [N II] emission has a similar deficit in galaxies with high infrared luminosities. Figure 3.1 shows a similar decrease in $L_{\rm [NII]}/L_{\rm IR}$ with increasing $L_{\rm IR}$. There are fewer low redshift galaxies with similar observations, but the [N II] line luminosity for $z \sim 4.5$ SMGs follows the local galaxy trend. It is difficult to identify whether a 'deficit' exists in this [N II] lines as there are few

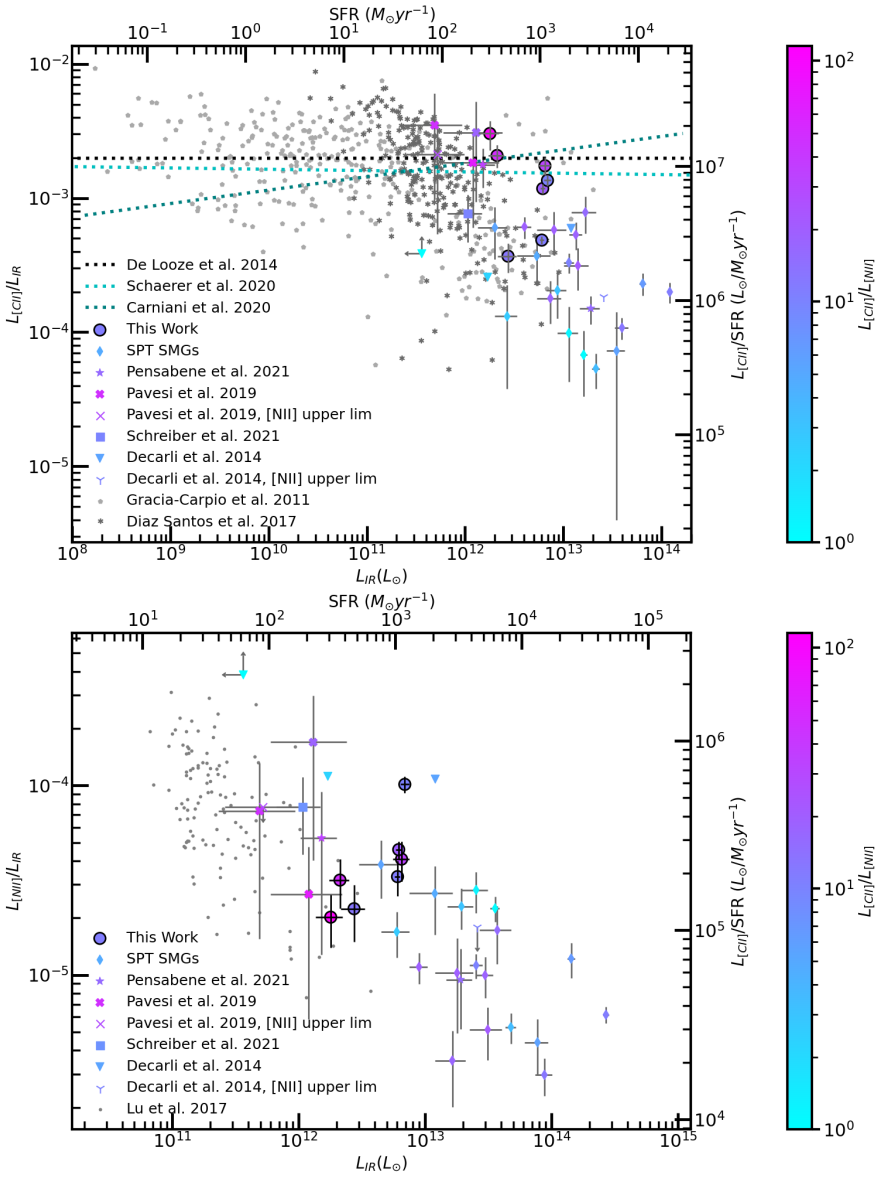

Figure 3.1: The [C II] deficit as a function of $L_{\rm IR}$ (*top*) and the equivalent relationship for [N II] (*bottom*) for $z = 4.5$ SMGs compared with local (grey; Graciá-Carpio et al. 2011; Díaz-Santos et al. 2017; Lu et al. 2017) and non-local galaxies and SMGs (coloured points; Decarli et al. 2014; Cunningham et al. 2020; Reuter et al. 2020; Pensabene et al. 2021; Pavesi et al. 2019; Schreiber et al. 2021). Non-local galaxies are colour-coded according to their [C II]/[N II] luminosity ratio as shown by the colour-bars; non-filled points are undetected in [N II]. The $z \sim 4.5$ SMGs from this work have a range of [C II]/$L_{\rm IR}$, with two showing a clear [C II] deficit. The [N II] emission from the SMGs is broadly consistent with expectations from local galaxies. In Section 3.5 we further explore the apparent correlation that galaxies with lower [C II]/[N II] ratios have higher fractions of [C II] originating from H II regions and have more significant [C II] deficits.

observations in galaxies with $L_{\rm IR} < 10^{11}\,{\rm L}_{\odot}$, which is where the flat relationship is observed in [C II].

3.3 [C II] luminosity function

The SMGs targeted by this study were originally serendipitously-detected, and therefore used to derive the $z = 4.5$ [C II] luminosity function (Swinbank et al., 2012; Cooke et al., 2018). Our new deep data robustly confirms the detection of [C II] in six of the SMGs (plus one serendipitous [C II] detection), but shows that the other six are not at $z = 4.5$. We therefore next update the $z = 4.5$ luminosity function to account for these confirmations.

We separate the AS2UDS sample into galaxies with with 870 μm fluxes (S_{870}) above and below the original survey detection limit of S_{870}=3.6 mJy Cooke et al. (2018). ALESS 65.1 is incomplete in its original (S_{870}) flux, though it is above the 50% completeness limit of 4.0 mJy Weiß et al. (2009) and has been corrected accordingly.

To calculate the [C II] completeness correction we inject 10^4 fake lines with different luminosities and linewidths into spectra taken from each galaxies image and test for detection by attempting to re-extract the injected lines. The 50% completeness limit is $L_{\rm [CII]} > 2.79 \times 10^8 L_{\odot}$, 60% at $L_{\rm [CII]} > 3.13 \times 10^8 L_{\odot}$, 70% at $L_{\rm [CII]} > 3.51 \times 10^8 L_{\odot}$, 80% at $L_{\rm [CII]} > 4.01 \times 10^8 L_{\odot}$, 90% at $L_{\rm [CII]} > 5.04 \times 10^8 L_{\odot}$, 95% at $L_{\rm [CII]} > 7.26 \times 10^8 L_{\odot}$, and 99% at $L_{\rm [CII]} > 2.79 \times 10^9 L_{\odot}$. All of the detected lines have $L_{\rm [CII]} > 10^9\,{\rm L}_{\odot}$, and thus our study is $> 99\%$ complete in the luminosity ranges probed.

As our study only targets SMGs the observed density of [C II] emitters is a lower limit, since non-SMG [C II] sources would be missed by our observations. We calculate an upper limit on the density of [C II] emitters based on the number of serendipitous [C II] sources visible within our area of observation. On average, we detect < 1 serendipitous [C II] emitters per field in our observations. Thus we can constrain the $L_{\rm [CII]}$ to between n-sources/Mpc^3 (where n is the number of [C II] detected galaxies measured by us, black circles in Figure 3.2) and (n+1)-sources/Mpc^3 (black downwards triangles in Figure 3.2).

The updated $z = 4.5$ [C II] luminosity function is shown in Figure 3.2. As explored in Section 2.7 the [C II] luminosities measured here are brighter than presented in Cooke et al. (2018) for the same objects. Furthermore, the fainter targets from Cooke et al. (2018) are not confirmed by our observations. The cumulative effect is that our updated measurements probe a brighter portion of the [C II] luminosity function than Cooke et al. (2018) and Swinbank et al. (2012).

Our measurements show an elevation in the bright end of the luminosity function compared with the $z = 0$ calibration from Hemmati et al. (2017), a finding which is seen in the ALPINE survey (Yan et al., 2020; Loiacono et al., 2021) and model predictions from Lagache et al. (2018) (Figure 3.2). Simulations from Popping et al. (2016), and Yang et al. (2022) (which is based on work Popping et al. 2019) underpredict the luminosity function at high [C II] luminosities, where the Yang et al. (2022) luminosity function is extrapolated from their predicted [C II]-halo mass relationship using a halo mass function[1]. Extrapolation of the local [C II] luminosity function (Hemmati et al., 2017) is also lower than high-redshift observations, which points to evolution in the [C II] luminosity function over the past ~ 12.7 Gyr. These results suggest that the 'knee' of the Schechter function may move to higher $L_{[\mathrm{CII}]}$ with increasing redshift. We note however that in the case where [C II] traces SFR, the knee may be at even higher values of $L_{[\mathrm{CII}]}$ at earlier epochs when the star formation rate density in the Universe is at its peak at $z \sim 2$ (Figure 1.5).

3.4 [C II] emission regions

[C II] and [N II] have similar critical densities, but [C II] can be emitted from both H II regions and PDRs, whereas [N II] has a higher ionisation energy, and it can only originate from the ionised ISM. Thus, the ratio of $L_{[\mathrm{CII}]}/L_{[\mathrm{NII}]}$ can be used to infer the percentage of the [C II] emission originating from PDRs, and by extension the amount coming from the ionised ISM. Thus, the $L_{[\mathrm{CII}]}/L_{[\mathrm{NII}]}$ ratio provides insight into the different regions of origin for the [C II] and [N II] emission lines in each galaxy.

[1] https://github.com/JohannesBuchner/hmf

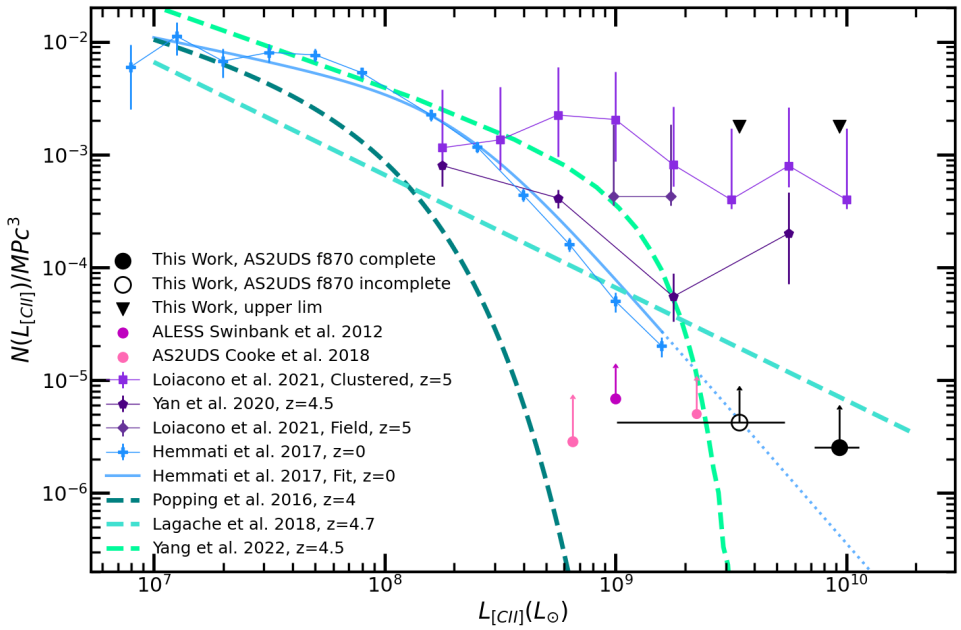

Figure 3.2: The $z \sim 4.5$ [C II] luminosity function for our new, deeper [C II] observations (black) is compared with initial measurements from Cooke et al. (2018) and Swinbank et al. (2012) (peach and pink coloured circles, respectively). Black downwards triangles represent upper limits based on our average detection of < 1 serendipitous [C II] emitter in each field in our observations. Results from the ALPINE survey are shown by dark purple pentagons for the main survey (Yan et al., 2020) and in purple squares/diamonds for serendipitous sources that are clustered/in the field from Loiacono et al. (2021). $z = 0$ results from Hemmati et al. (2017) are shown by blue plusses and the fit to this data is shown in a solid blue line for the data range covered by their observations, and a dotted blue line where it is extrapolated beyond this. Finally results from simulations from Popping et al. (2016), Yang et al. (2022) and Lagache et al. (2018) are shown by teal, green and aquamarine dashed lines respectively. These results support an evolution in the $L_{[CII]}$ luminosity function with redshift with the Hemmati et al. (2017) $z = 0$ calibration underestimating the number of [C II] emitters at high $L_{[CII]}$.

Figure 3.3 shows the $L_{[CII]}/L_{[NII]}$ ratio as a function of L_{IR}. We follow Decarli et al. (2014) and Oberst et al. (2006) to determine that if all the [C II] emission originates from H II regions then $L_{[CII]}/L_{[NII]} = 2.44$ is expected for an assumed gas density of $32\,cm^{-2}$, based on the measurement of [N II] 122 μm/[N II] 205 μmin Oberst et al. (2006). In order to calculate the percentage of [C II] originating from the ionised ISM, we divide 2.44 by the observed $L_{[CII]}/L_{[NII]}$ ratio. Significantly higher values of the $L_{[CII]}/L_{[NII]}$ ratio correspond to higher fractions of the [C II] emission originating from PDRs (i.e. less emission from H II regions).

We note that the derived fraction of [C II] from the PDR can also change as a function of C+/N+. Oberst et al. (2006) assume C+/N+ = 1.772 (Savage & Sembach, 1996; Oberst et al., 2006). However if significant amounts of Carbon are ionised to higher ionisation states (e.g. by X-rays) this could cause a deficit in C+ compared to N+. Discussions on how the C/N abundance ratios can affect the $L_{[CII]}/L_{[NII]}$ ratio can be found in Langer et al. (2016) and Zhang et al. (2018).

All seven of the $z \sim 4.5$ SMGs have [C II] emission that is dominated by PDRs with an average [C II] PDR fraction of $89.0 \pm 6.47\%$. However, we caution that there appears to be variation in the SMG population (which may be due to selection effects), since SMGs identified by the SPT show more diversity in the dominant [C II] emission regions (Cunningham et al., 2020; Reuter et al., 2020). Figure 3.3 includes galaxies of different types at $z = 2.5$–6.6, demonstrating that different galaxies (even within the same selection criteria) can have significant variation in their $L_{[CII]}/L_{[NII]}$ ratios. Thus, studies that focus on [C II] alone are likely probing different regions of different galaxies, even within the same sample. This should be accounted for when the [C II] emission line is being used as a tracer of any one phase of gas, or as an SFR tracer as the conversion needed to infer an SFR will change depending on which gas phase it is tracing, just as the conversion of any one tracer of e.g. ionised gas will have a different conversion factor to SFR compared to a tracer of neutral gas. We search for a correlation between $L_{[CII]}/L_{[NII]}$ and L_{IR} and find a Spearman's rank coefficient of -0.22 with a p-value of 0.20 (i.e. a non significant (p-value > 0.05) negative correlation)

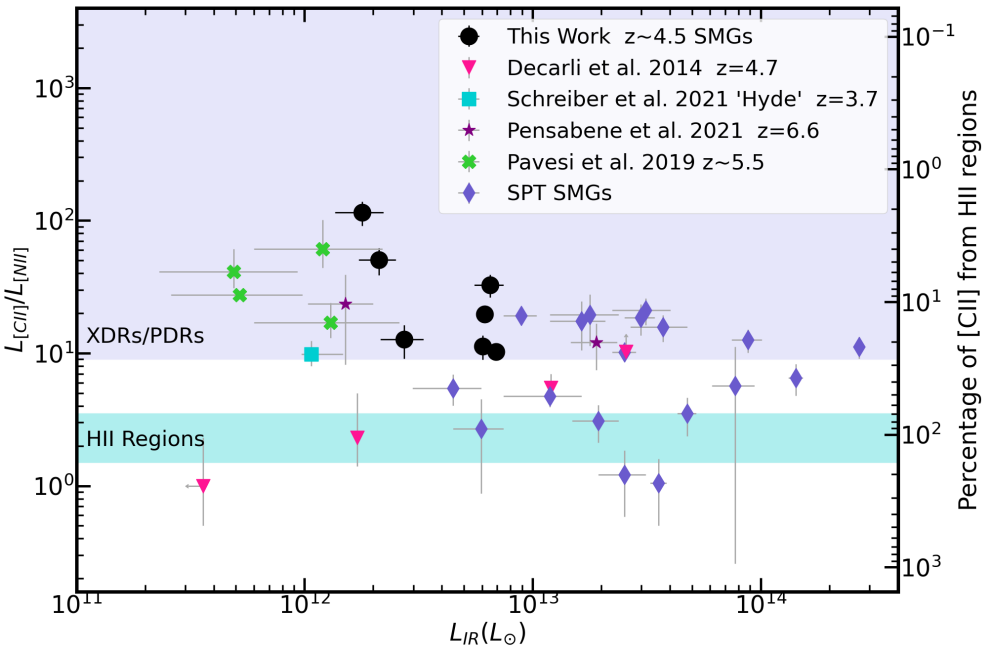

Figure 3.3: The $L_{[\mathrm{CII}]}/L_{[\mathrm{NII}]}$ ratio against the total IR luminosity (rest-frame $8-1000\,\mu$m) for this sample of $z\sim4.5$ SMGs and samples of LAEs, SMGs and QSOs at $z=4.7$ (Decarli et al., 2014), the quenching/SF galaxy 'Hyde' at $z=3.7$ (Schreiber et al., 2021), quasar host galaxies at $z=6.6$ (Pensabene et al., 2021), two 'normal' galaxies and one LBG at $z\sim5.5$ (Pavesi et al., 2019), and a sample of SMGs at $z=3$–6 from SPT (Cunningham et al., 2020; Reuter et al., 2020). Shading shows the ratio of [C II] to [N II] emission expected from H II regions and PDRs from Decarli et al. (2014). The [C II] emission from all the $z\sim4.5$ SMGs predominantly originates from PDRs though with PDR fractions ranging from 76% to 97%. There is a large spread of $L_{[\mathrm{CII}]}/L_{[\mathrm{NII}]}$ across all samples, which highlights the variation in the origin of [C II] emission from different galaxies. We search for a correlation between $L_{[\mathrm{CII}]}/L_{[\mathrm{NII}]}$ and L_{IR} and find a Spearman's rank coefficient of -0.22 with a p-value of 0.20 (i.e. a non significant (p-value >0.05) negative correlation).

3.5 Origin of the [C II] deficit in $z = 4.5$ SMGs

We next investigate whether the $L_{[CII]}/L_{[NII]}$ ratio is correlated with the strength of the [C II] deficit in individual galaxies. Such a correlation would exist if the mechanism driving the [C II] deficit is driven primarily in one phase of the ISM.

As explored in Section 3.2, Figure 3.1 shows the $L_{[CII]}/L_{IR}$ ratio against L_{IR}, with colour-coding representing the $L_{[CII]}/L_{[NII]}$ ratio of each galaxy. It appears that galaxies with lower $L_{[CII]}/L_{[NII]}$ ratios (i.e. a higher fraction of [C II] originating from H II regions) have greater [C II]-deficits. If this is the case then it suggests that the [C II] deficit may be being driven by the ionised regions.

To explore this correlation further, in Figure 3.4 we plot $L_{[CII]}/L_{IR}$ as a function of $L_{[CII]}/L_{[NII]}$. There is a significant positive correlation between these parameters (Spearman's rank correlation coefficient = 0.64, p-value = 2×10^{-5}), which indicates that there is indeed a link between the ionisation of the ISM and the mechanism driving the [C II]-deficit. This result is consistent with findings from Díaz-Santos et al. (2017) and Sutter et al. (2019), which used $L_{[CII]}/L_{[NII]}$ to show that the [C II] deficit is greater when considering only [C II] originating from the ionised ISM.

We also investigate whether there is a correlation between the [N II] deficit and the $L_{[CII]}/L_{[NII]}$ ratio. If a correlation occurs this would indicate that there is something more fundamental about the mechanism driving the [C II] deficit such that it drives the deficit in other lines, as well as affecting PDRs. However, Figure 3.4 shows that no such correlation exists.

A plethora of mechanisms have been proposed as the drivers of the [C II] deficit. One of the simplest solutions is the saturation of the [C II] line (see e.g. Kaufman et al. 1999, also Rybak et al. 2019, Bisbas et al. 2022). The saturation is hypothesised to occur in regions of extremely strong ionising fields, where [C II] ions could become thermally saturated and would thus reach a maximum rate of photon emission. The same would not be true for the dust in these regions which could continue to radiate brighter, causing an apparent deficit in the measured [C II] relative to the dust continuum emission. Such a process would coincide with H II regions as these are the areas with the strongest ionising fields. Thus, this hypothesis is consistent with our data (e.g. Figure 3.4). This theory is also

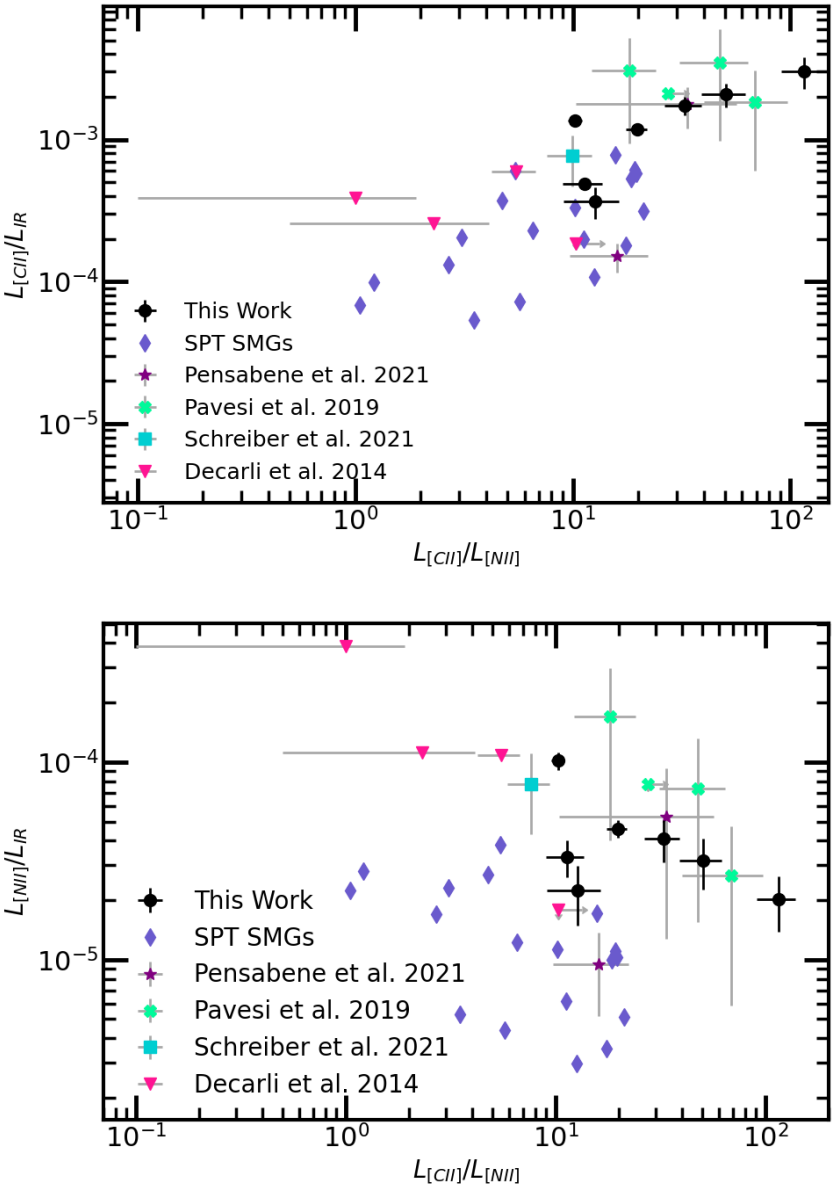

Figure 3.4: The $L_{[\mathrm{CII}]}/\mathrm{L_{IR}}$ (*top*) and $L_{[\mathrm{NII}]}/\mathrm{L_{IR}}$ (*bottom*) ratios as a function of $L_{[\mathrm{CII}]}/L_{[\mathrm{NII}]}$. These figures show the correlation between the [C II] and [N II] deficits and the fraction of [C II] originating from PDRs. The top panel shows a significant correlation between the parameters (Spearman's rank correlation coefficient = 0.64, p-value = 2×10^{-5}), demonstrating that galaxies with a greater contribution of [C II] flux from H II regions (i.e. lower $L_{[\mathrm{CII}]}/L_{[\mathrm{NII}]}$ ratios) have a stronger [C II] deficit (i.e. lower $L_{[\mathrm{CII}]}/\mathrm{L_{IR}}$). Conversely, the bottom panel shows that there is no significant correlation (Spearman's rank correlation coefficient = -0.111, p-value = 0.50) between the [N II] deficit and $L_{[\mathrm{CII}]}/\mathrm{L_{IR}}$. Symbols are the same as those described in Figure 3.3.

explored in Díaz-Santos et al. (2017) with additional evidence being that this deficit is also observed in other emission lines (e.g. the [N II] 205μm line as seen in Figure 3.1 here, along with [N II] 122 μm and [OIII] 88 μm lines in Díaz-Santos et al. 2017), and the strength of the emission line deficit is anti-correlated with the line's critical density.

An alternative theory is that proposed by Narayanan & Krumholz (2017) wherein the size of PDRs shrinks at higher SFRs and thus IR luminosities. This is due to the typical cloud surface density increasing, which in turn increases the hydrogen molecular fraction (H_2/H I). If [C II] is preferentially produced in PDRs, then decreasing the size of the PDRs will create an overall decrease in the [C II] luminosity.

Sutter et al. (2019) propose that the deficit seen in the [C II] emission from ionised regions could be driven by a change in the fraction of UV photons being absorbed by dust within H II regions as compared to PDRs. The hypothesis is driven by the observed correlation between galaxies with warmer dust temperatures and a greater [C II]-deficit (Díaz-Santos et al., 2017). Galaxies with warmer dust tend to have heightened absorption of UV photons by dust, which leads to a lower fraction of the UV light leaking into the diffuse ISM and being able to ionise the [C II] in diffuse H II regions (e.g. Díaz-Santos et al., 2017; Herrera-Camus et al., 2018). Sutter et al. (2019) suggest that the decrease in [C II]/$L_{\rm IR}$ could be caused by either: a smaller fraction of the UV radiation being above the Lyman limit due to a lack of very recent star-formation, or a smaller fraction of the UV light reaching the diffuse ISM and thus being able to ionise [C II]. This second scenario would appear as increased emission from the warm dust compared with [C II], creating an apparent deficit in the [C II] emission. Since we observe the same trend in [C II]-deficit with respect to ionised vs neutral ISM [C II] as Sutter et al. (2019) in high-redshift SMGs (Figure 3.4; which we know are sites of active star formation), we suggest that the second mechanism (increased emission from warm dust) is the more likely of these scenarios to be driving the deficit in these sources.

By examining the trends seen in Figure 3.4 it is possible to determine which region of the ISM is responsible for the decrease in $L_{\rm [CII]}$ compared to $L_{\rm IR}$. We consider a model where $L_{\rm [CII]}$ is equal to $L_{\rm [CII],pdr} + L_{\rm [CII],ion}$ and where $L_{\rm [NII]}$ scales

proportionally with $L_{[CII],ion}$. By varying the amount of $L_{[CII],ion}$ with constant $L_{[CII],pdr}$ (and vice versa) and tracking the effect on $L_{[CII]}/L_{IR}$ and $L_{[NII]}/L_{IR}$ vs $L_{[CII]}/L_{[NII]}$, it is seen that the change in the amount of $L_{[CII]}$ must be originating from the PDRs.

Given this scenario, if the [C II] deficit was originating from the ionised ISM then we would expect to see a mirrored decrease in $L_{[CII]}/L_{IR}$ and $L_{[NII]}/L_{IR}$ with increasing $L_{[CII]}/L_{[NII]}$. Instead, we see an increasing $L_{[CII]}/L_{IR}$ with increasing $L_{[CII]}/L_{[NII]}$ while $L_{[NII]}/L_{IR}$ remains approximately constant, consistent with the scenario of reduced [C II] emission from PDRs as proposed by the scenario from Narayanan & Krumholz (2017). This result also supports observations of galaxies exhibiting a greater [C II] deficit having a larger fraction of their emission originating from the ionised ISM.

3.6 Improving the accuracy of [C II] as a SFR tracer

Linear correlations between [C II] luminosity and SFR are increasingly being used to measure SFR, especially in high-redshift galaxies where there is not much multiwavelength data. As such, [C II]-SFR relations have been calibrated for a number of datasets across different redshift ranges (e.g. De Looze et al. 2014; Carniani et al. 2020; Harikane et al. 2020). The use of such data for estimating SFR is problematic as the [C II] deficit means that SFR could be unknowingly underestimated at high L_{IR}, but the observer would have no way of knowing that their data is in the deficit regime without having to first collate enough photometry to fit an IR SED.

We measure the relation between the [C II] deficit and the $L_{[CII]}/L_{[NII]}$ ratio (Figure 3.4) and we next aim to use the $L_{[CII]}/L_{[NII]}$ ratio to derive the intrinsic [C II] luminosity that would be present if there were no [C II] deficit. i.e. use the [N II] 205 μm to correct the measured [C II] luminosity to a value that directly correlates with the IR luminosity and hence the SFR. Thus, this correction will improve the accuracy of [C II] as a SFR tracer, without the need for detected IR continuum photometry and SED fitting.

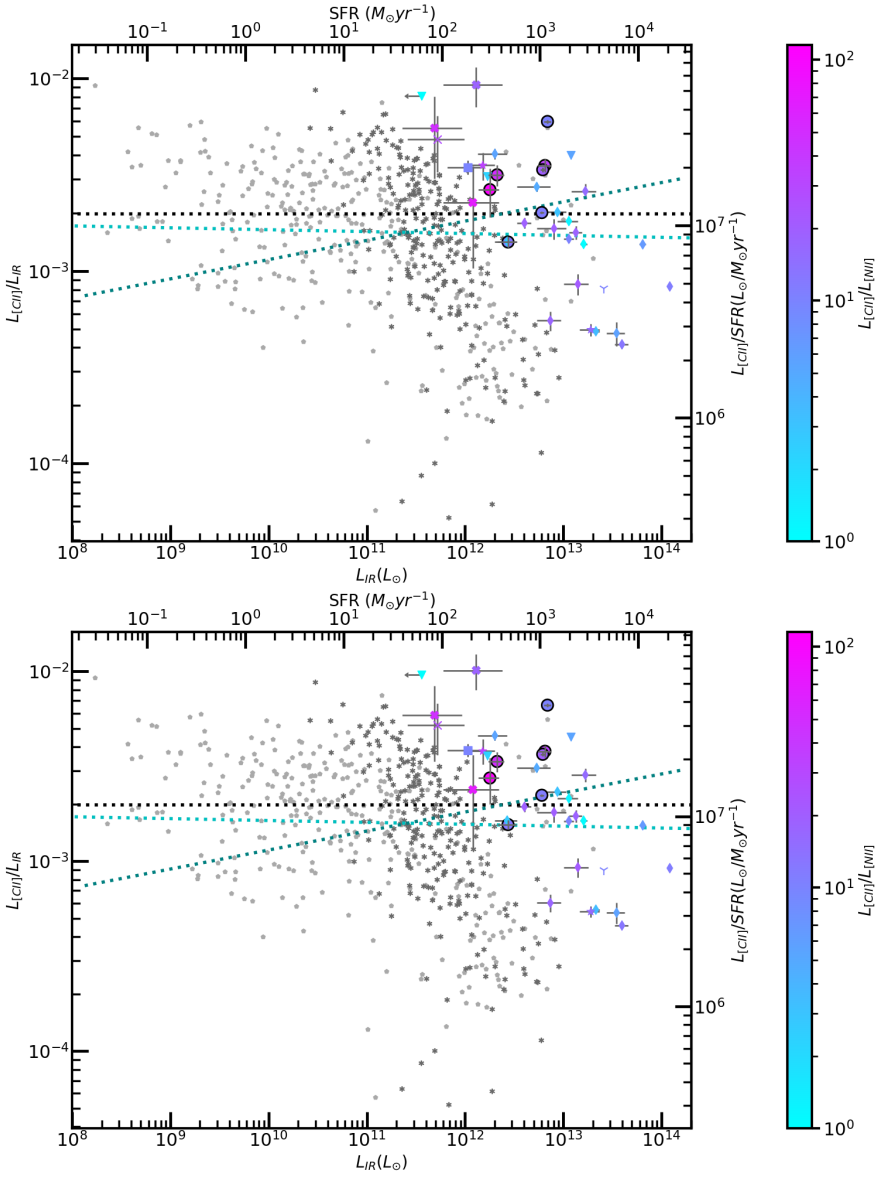

Figure 3.5: *Top:* The correlation between corrected [C II]/$L_{\rm IR}$ as a function of $L_{\rm IR}$, after the observed [C II] luminosity has been adjusted based on a calibration to the $L_{\rm [CII]}$-SFR relation from De Looze et al. (2014). This adjustment has only been performed for galaxies with a measured $L_{\rm [CII]}$ and $L_{\rm [NII]}$. Error bars represent observational uncertainties only. *Bottom:* The same as the top panel, but using the [C II] calibration that is based on the $L_{\rm [CII]}$-SFR relation from Carniani et al. (2020). Local galaxies are shown with grey points (Graciá-Carpio et al., 2011; Díaz-Santos et al., 2017), and non-local galaxies and SMGs (coloured points; Decarli et al. 2014; Pavesi et al. 2019; Cunningham et al. 2020; Reuter et al. 2020; Pensabene et al. 2021; Schreiber et al. 2021).

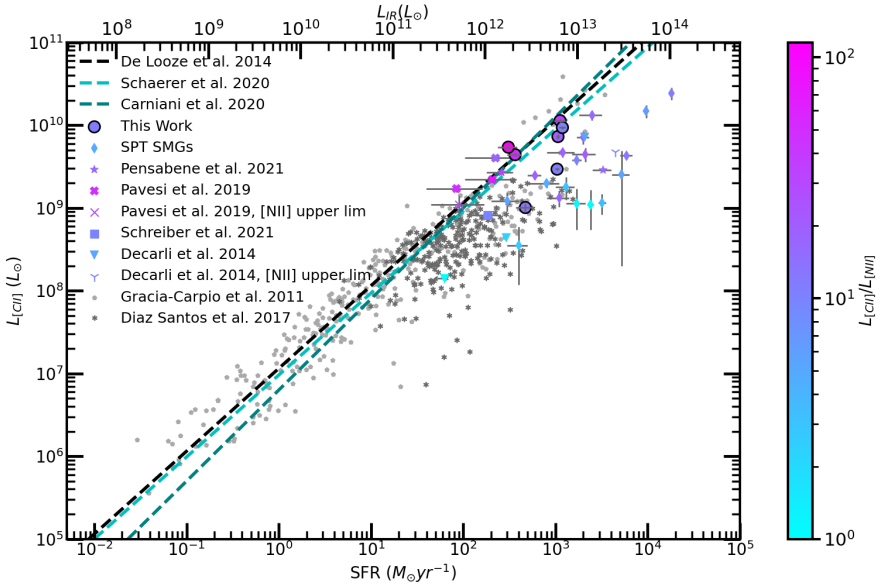

Figure 3.6: Observed $L_{[\mathrm{CII}]}$-SFR correlation for our galaxy sample, with colours represented the observed $L_{[\mathrm{CII}]}/L_{[\mathrm{NII}]}$ ratio (where non-filled points represent a limit in the $L_{[\mathrm{NII}]}$). Local galaxies are shown with grey points (Graciá-Carpio et al., 2011; Díaz-Santos et al., 2017), and non-local galaxies and SMGs (coloured points; Decarli et al. 2014; Pavesi et al. 2019; Cunningham et al. 2020; Reuter et al. 2020; Pensabene et al. 2021; Schreiber et al. 2021). The dashed lines show the $L_{[\mathrm{CII}]}$-SFR relations calibrated by De Looze et al. (2014), Schaerer et al. (2020) from ALPINE data, and Carniani et al. (2020).

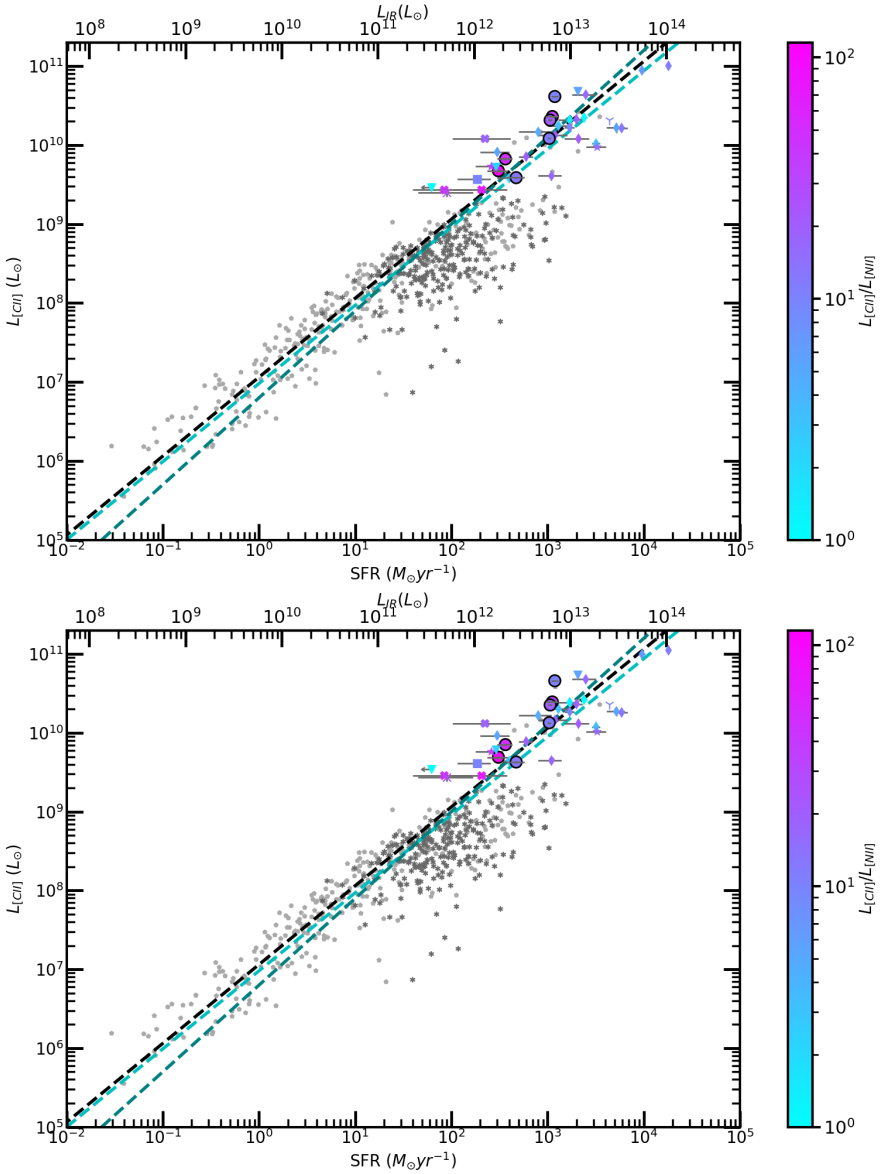

Figure 3.7: *Top:* The $L_{[CII]}$-SFR correlation after the [C II] luminosity has been corrected for the [C II] deficit using the $L_{[CII]}/L_{[NII]}$ ratio and the De Looze et al. (2014) calibration. This adjustment has only been performed for galaxies with a measured $L_{[CII]}$ and $L_{[NII]}$. Error bars represent measurement uncertainties only. *Bottom:* As the top panel, but using the Carniani et al. (2020) $L_{[CII]}$-SFR relation for calibration. Points are the same as described in Figure 3.6.

To parameterise the required correction we consider [C II]-SFR relations from De Looze et al. (2014) (using the calibration for H II/starburst galaxies, though our results do not change significantly if we use the calibration from their entire sample) and Carniani et al. (2020). For each galaxy and each [C II]-SFR relation we measure the difference between the observed [C II] luminosity and the [C II] luminosity that would be expected based on the IR luminosity (i.e. equivalent to SFR). The expected vs observed luminosities are parameterised as a function of $L_{[\mathrm{CII}]}/L_{[\mathrm{NII}]}$ ratio and the fits are used to correct the observed [C II] luminosities using only the $L_{[\mathrm{CII}]}/L_{[\mathrm{NII}]}$.

The equation to perform the correction are as follows,

$$[CII]_C = B([CII]^2_O/[NII])^a \tag{3.1}$$

where $[CII]_C$ is the corrected [C II] luminosity, $[CII]_O$ is the observed [C II] luminosity, [N II] is the observed [N II] 205 μm luminosity. We measure $\log(B) = 1.43 \pm 0.16$ and $a = -0.701 \pm 0.13$ for the De Looze et al. (2014) relation, and $\log(B) = 1.49 \pm 0.17$ and $a = -0.719 \pm 0.14$ for the Carniani et al. (2020) relation. We also explored the [C II]-SFR relation from Harikane et al. (2020), but it is a poor fit to our data. The relation from Schaerer et al. (2020) is consistent with that from De Looze et al. (2014) and so is not reported separately.

The results of correcting the [C II] luminosities to intrinsic values using this method are shown in Figure 3.5 for the [C II]-deficit and Figures 3.6 and 3.7 show the uncorrected and corrected [C II]-SFR relations, respectively. Thus, by utilising both the [C II] and [N II] lines the SFR of a galaxy can be calculated using the above calibration in a way that accounts for the [C II] deficit and gives a more accurate result (i.e. closer to the value obtained from an L_{IR}conversion) compared to using [C II] alone.

3.7 Conclusions

We have used ALMA Band 6 and 7 data to study the sample of seven SMGs at $z \sim 4.5$ described in Chapter 2. The ALMA data are used to measure the

[C II] 158 μm and [N II] 205 μm far-IR emission lines and dust continuum. We study the fraction of [C II] emission originating from PDRs and thus assess the suitability of [C II] as a SFR tracer at high IR luminosities. Our main results are summarised as follows:

- We constrain the $z = 4.5$ [C II] luminosity function, updating previous measurements from Cooke et al. (2018) and Swinbank et al. (2012) in light of the new information about the SMGs. Our measurements are consistent with results from the ALPINE survey (Yan et al., 2020; Loiacono et al., 2021), and simulations from Lagache et al. (2018).

- In all of the $z \sim 4.5$ SMGs the majority of the detected [C II] line emission originates from PDRs. The fraction of the [C II] luminosity from PDRs is $\sim$ 70–95% in these SMGs, in agreement with studies of other high redshift SMGs (Cunningham et al., 2020; Reuter et al., 2020)

- We observe a deficit in both the [C II] and [N II] line luminosities in galaxies with high IR luminosities, consistent with previous results (Cunningham et al., 2020; Reuter et al., 2020; Díaz-Santos et al., 2017). There is a significant correlation between the strength of the [C II] deficit and the [C II]/[N II] ratio across all sources studied. We use the relationships between [C II]/[N II], [C II]/$L_{\rm IR}$and [N II]/$L_{\rm IR}$to determine that the deficit most likely originates from a difference occurring in the galaxies PDRs.

- We identify a relation to correct observed [C II] fluxes using [C II]/[N II] line ratios which minimises the effect of the [C II] deficit and yields more reliable [C II]-SFR relationships, accounting for the [C II] deficit and preventing underestimation of the SFR. Thus, this calibration can be used to obtain more accurate SFRs for galaxies without detections of the dust continuum. This is important when using [C II] as the lone indicator of SFR as without multiwavelength data and an IR SED it is impossible to know if observations are affected by the deficit.

Chapter 4

Resolved properties of [C II] and [N II] in $z \sim 4.5$ SMGs

4.1 Introduction

As discussed in Section 1.5.2, the triggering mechanisms of SMGs, and particularly those at high redshift, is a topic of debate with evidence existing for both major mergers and more secular processes. Additionally, there are few direct comparisons between the kinematics (and thus origins of SMG populations) at different epochs which causes difficulty in drawing conclusions about their evolution through cosmic time. The fate of SMGs is a topic of open research, with the leading theory being that SMGs are progenitors to massive elliptical galaxies (e.g. Toft et al. 2014) where information about gas fractions and depletion timescales can help build evidence for links between SMGs and early type galaxies.

In this Chapter we present a resolved study of the [C II] and [N II] emission from seven SMGs at $z \sim 4.5$. The targets are the seven SMGs described in Chapter 2 with detections of both [C II] and [N II] in their data cubes. We aim to determine the relative sizes of the [C II], [N II] and continuum emission regions and thus the sizes of the neutral gas, ionised gas and dust. By examining the cospatiality and dynamics of the gas we aim to place constraints on the history and potential triggering mechanisms of these sources. We study the dynamics

of the gas in six of the SMGs (AS2UDS 0109.1 being too faint) using the [C II] emission and dynamical models.

This study aims to investigate the resolved properties of the target SMGs, and we therefore use the higher resolution data, processed as detailed in Section 2.4. The data are reprocessed using the Common Astronomy Software Application (CASA) McMullin et al. (2007) version 5.6.1. The CASA task TCLEAN is used to image the data, using Briggs weighting (Briggs, 1995) with ROBUST = 0.0 and −2.0 to maximise the visibility to extended emission. Whilst ROBUST = −2.0 theoretically gives higher resolution output due to higher weighting on longer baselines, examination of the reimaged data shows that the corresponding increase in noise in these images is significant. We therefore use the data imaged with ROBUST = 0.0 in our analyses. The data are CLEANed down to 3× the rms level with sources masked using CASA's 'AUTO-MULTITHRESH' routine. CLEANed continuum maps are created using only line free channels. For spectral cubes, we use UVCONTSUB to fit and subtract the continuum from the data in the *uv*-plane before masking and CLEANing the cubes for analysis using TCLEAN.

This Chapter is structured as follows: in Section 4.2 we assess the cospatiality of the emission types. In Section 4.3 we measure the sizes of the emission in the *uv*-plane and compare the sizes of different gas and dust tracers. In Section 4.4 we undertake a kinematic analysis of the $z \sim 4.5$ SMGs and measure the masses of their different components in Section 4.5. In Section 4.6 we discuss the evolution of SMGs, including comparing SMGs at different epochs, exploring their triggering and future evolution. We present our conclusions in Section 4.7.

4.2 Cospatiality of gas and dust tracers

We first investigate whether the [C II], [N II] and dust continuum are all emitted by the same region(s) of each SMG, by pinpointing the location of each gas/dust tracer. For [C II] and [N II] the positions are measured from Moment 0 maps created from the data cubes for each of the SMGs, as shown in Figure 4.1. Note that AS2UDS 0109.1 is near the edge of the field of view and thus strongly affected

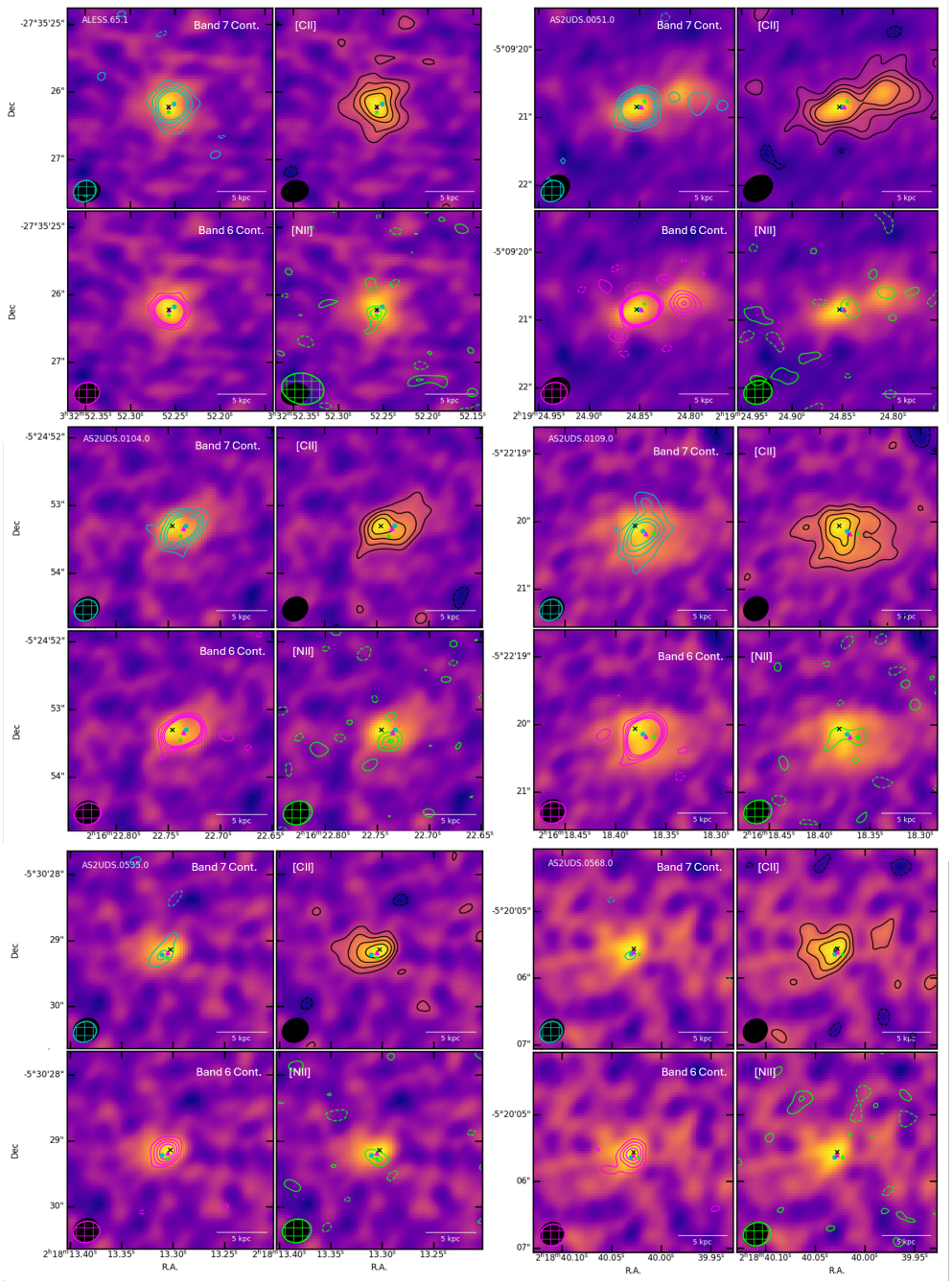

Figure 4.1: $3'' \times 3''$ moment 0 maps of the [C II] emission from our six targets. Each group of four panels presents a single SMG (as labelled in the top-left of the group) with contours highlighting a different gas or dust tracer in each panel. North is up and east is to the left. Band 7 continuum is shown in cyan (top-left of each group), [C II] (black; top-right), Band 6 continuum (pink; bottom-left), and [N II] (lime; bottom-right); positions of the peak flux of each gas/dust are indicated with crosses of corresponding colours on all panels. Contours are at the 3σ, 5σ, 7σ and 9σ levels and negative emission is represented by dashed contours at the same levels. The beam size for each background [C II] image is shown by the black ellipse and overlaid with the beam of the corresponding contour map.

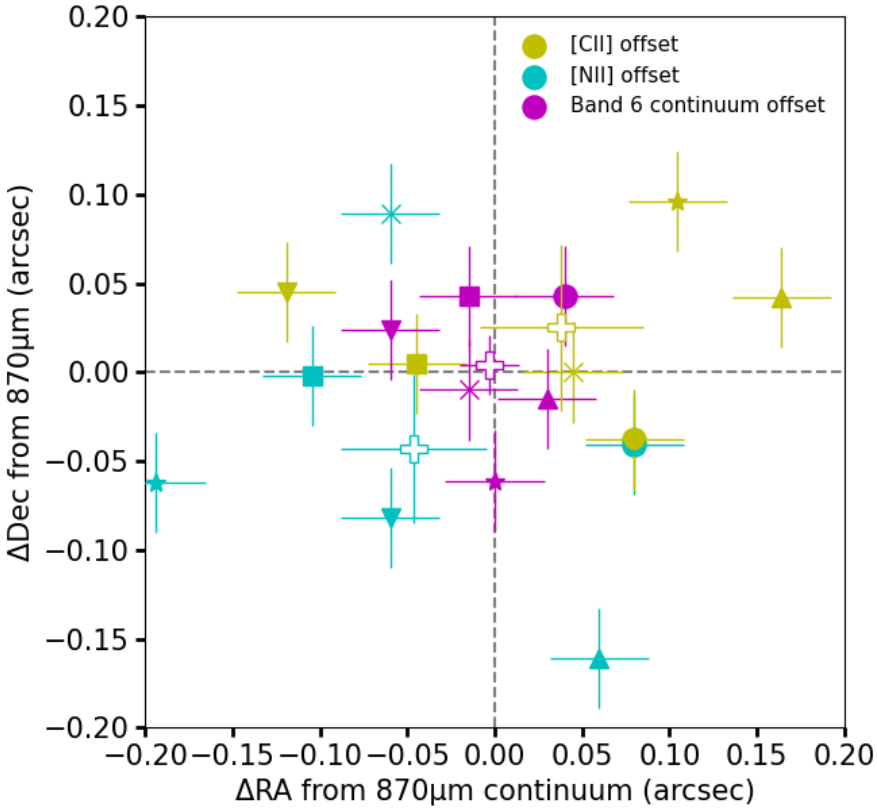

Figure 4.2: Spatial offsets between the peak of the Band 7 (350 GHz) continuum emission and the Band 6 continuum (260 GHz; pink), [C II] (yellow) and [N II] (cyan). Each galaxy is represented by a different marker style[a] and the empty plusses show the average offset position of each emission type. The Band 6 and Band 7 continuum are consistent with being cospatial, but both [C II] and [N II] have significant scatter from the Band 7 continuum, though these offsets are in different directions, which indicates an offset in the positions of ionised and neutral gas within the galaxies.

[a] Circles are ALESS 65.1, crosses are AS2UDS 0051.0, upwards triangles are AS2UDS 0104.0, stars are AS2UDS 0109.0, downwards triangles are AS2UDS 0535.0 and squares are AS2UDS 0568.0.

by noise and the primary beam correction. Therefore, AS2UDS 0109.1 is excluded from this analysis.

Half of the SMGs have smooth morphologies in the Band 7 continuum (observed frame 860 μm), which is typically broadly replicated in the Band 6 continuum (observed-frame 1110 μm), [C II], and [N II] emission, although with lower SNR in the latter. The exceptions are AS2UDS 0568.0, AS2UDS 0051.0 and AS2UDS 0109.0.

AS2UDS 00568.0 is not well-detected in [N II] or the Band 6 continuum, leading to unclear morphologies in these tracers, though the [C II] and the Band 6 continuum maps are broadly similar.

AS2UDS 0109.0, has a 5σ extension to the north of the peak emission in the Band 7 continuum that is not present in the [C II] or any of the other tracers. Conversely, the [C II] emission is extended to the east and west (also at the 5σ level) beyond the other tracers. This extended [C II] emission could be the result of a tidal interaction with the nearby galaxy AS2UDS 0109.1 ($\sim$74 kpc separation). The [C II] would be more affected by this than the [N II] and continuum as the [C II] is expected to be more extended and thus more easily gravitationally influenced by outside forces than the ionised gas and dust that resides in more compacted regions closer to the galaxies centre. The dynamics of these features are explored using moment 1 maps in Section 4.4.

AS2UDS 0051.0 consists of two distinct components that are both detected at $> 3\sigma$ in all four gas/dust tracers (Figure 4.1). The [C II] and [N II] lines show that the velocity offset between the two components is only 200 km s^{-1}. The [C II] map shows that gas is being shared between the two components and it is thus highly likely that AS2UDS 0051.0 is undergoing major merger. The eastern component is the brighter of the two and contains the emission peak for all emission types measured here.

The two galaxies with the most disturbed morphologies in Figure 4.1 (AS2UDS 0109.0 and AS2UDS 0051.0) are the two SMGs with the brightest infrared luminosities (and thus SFRs; Table 2.1). These galaxies each have SFR $> 1000\,M_{\odot}\,yr^{-1}$, compared to an expected $\sim 500 M_{\odot} yr^{-1}$ for $z = 4.5$ SMGs based on calibrations from Dudzevičiūtė et al. (2020). Thus, our morphological findings are consistent with theories of enhanced star formation being a result of interactions and mergers

experienced by populations of SMGs, especially at high redshift (Conselice et al., 2008; Davé et al., 2010; Engel et al., 2010; Hopkins et al., 2013).

Figure 4.2 shows the spatial offsets between the peak of the Band 7 continuum emission and the peak of the [C II], [N II] and Band 6 continuum for each galaxy. The average positional offset between the Band 7 and Band 6 continuum emission is $0.047'' \pm 0.017''$ ($\sim$ 0.3 kpc at $z \sim 4.5$), where the stated uncertainties represent the galaxy-to-galaxy scatter; measurement uncertainties are typically $0.028''$ The average separation between the Band 7 continuum and the [C II] emission is $0.10'' \pm 0.047''$ ($\sim$ 0.7 kpc at $z \sim 4.5$) and there is an average of $0.13'' \pm 0.042''$ ($\sim$ 0.9 kpc at $z \sim 4.5$) between the Band 7 continuum and [N II] emission. The mean separation between the [C II] and [N II] peak positions is $0.15'' \pm 0.11''$ ($\sim$ 1 kpc at $z \sim 4.5$)

Figure 4.2 therefore shows that the two dust continuum tracers are consistent with being cospatial, but that [C II] and [N II] lines likely originate from different regions of the galaxies. Intriguingly, the [C II] and [N II] lines appear to be offset in different directions from the dust continuum, which highlights the multi-phase nature of the [C II] line. This finding is consistent with the [N II] line primarily tracing the ionised medium, but the [C II] line tracing both the neutral and ionised ISM (Chapter 3). Thus, the difference in positions of the [C II] and [N II] lines indicates an offset in the different ISM phases within these $z \sim 4.5$ SMGs.

4.3 Emission region sizes

We next estimate the sizes of different emission regions in the SMGs directly in the *uv*-plane by comparing the amplitude of the signal from the source as a function of *uv*-distance. The *uv*-distance is a measurement of the separation of antennas as seen from the source, in units of kλ, where λ is the wavelength of the observations. This method is advantageous because it directly measures the received signal at different scales, without making assumptions about the source and without requiring weighting of the data, as is necessary during CLEANing and imaging.

Table 4.1: Sizes of the Band 7 continuum and [C II] emission as measured from *uv-amplitude* plots.

Source	Band 7 Cont. size (arcsec)	[C II] size (arcsec)	Band 6 Cont. size (arcsec)	[N II] size (arcsec)
ALESS 65.1	0.23 ± 0.02	0.31 ± 0.02	0.33 ± 0.02	0.29 ± 0.02
AS2UDS 0051.0	0.33 ± 0.04	0.53 ± 0.03	0.88 ± 0.06	0.70 ± 0.05
AS2UDS 0104.0	0.26 ± 0.02	0.43 ± 0.01	0.29 ± 0.01	0.40 ± 0.02
AS2UDS 0109.0	0.45 ± 0.03	0.62 ± 0.02	0.38 ± 0.02	0.61 ± 0.03
AS2UDS 0109.1[a]	1.41 ± 0.14	0.97 ± 0.09	0.27 ± 0.04	0.36 ± 0.07
AS2UDS 0535.0	0.29 ± 0.03	0.43 ± 0.03	0.35 ± 0.03	0.52 ± 0.10
AS2UDS 0568.0	0.39 ± 0.05	0.52 ± 0.05	0.39 ± 0.04	0.38 ± 0.08

[a] AS2UDS 0109.1 is at the edge of the image in Band 7 and thus has low SNR making measurements unreliable.

To extract the *uv*-amplitude information we first use the CASA task 'fixvis' to re-centre the visibilities to align with the peak position of each emission type as determined in Section 4.2. We then use the CASA task 'visstat' to measure the detected flux in 40 kλ bins across the full range of available baselines. These measurements are taken over the same frequency range determined from the region finding process described in Section 2.6. The resulting *uv*-amplitude plots are presented in Figure 4.3.

We verify that changing the binning does not affect the measured sizes of the emission regions in most galaxies and dust/gas tracers. The two exceptions are the Band 7 [C II] and continuum for AS2UDS 0109.1, where results are inconsistent if binning of < 40 kλ, measuring larger [C II] and continuum sizes, and the Band 6 continuum for AS2UDS 0568.0 where the measured size doubles with < 40 kλ binning. Both have consistent values with binning $\gtrsim 40$ kλ and so we use 40 kλ binning going forward. AS2UDS 0109.1 is situated 11″ from the centre of the observations where the primary beam coverage is low and the noise high. It is likely that the inconsistencies in the *uv*-amplitude information for AS2UDS 0109.1 are due to noise and we therefore excluded AS2UDS 0109.1 from further analyses.

To calculate source sizes from these measurements we fit a single Gaussian centred on 0 kλ to the *uv*-amplitude plots. For all sources except AS2UDS 0051.0 we force the Gaussian to have a zero baseline. For AS2UDS 0051.0 we fit a Gaus-

sian curve with a constant y-axis offset to account for an unresolved component in the emission. The best-fit uv-amplitude curves and the inferred source sizes are shown in Figure 4.3. We measure the full width at half max (FWHM) of the fitted Gaussian and convert it to a source-plane size using Equation 4.1

$$\theta_{\rm lm} = \frac{4\ln 2}{\pi\theta_{\rm uv}} \frac{3600\pi}{180} \tag{4.1}$$

where θ_{lm} is the FWHM of the image and θ_{uv} is the FWHM of the Gaussian fit to the uv-amplitude data.

To verify that we are able to reliably resolve the source sizes using this method we also tested the removal of long baselines (which are sensitive to smaller angular sizes) prior to fitting. Our size measurements are not affected by the removal of this long baseline information, which indicates that the sample is well constrained by the available data. This assertion holds despite the amplitude data not reaching zero in all cases. Furthermore, in all cases, the [C II] emission region (the most extended tracer) is smaller than the largest angular scale of the Band 7 observations. In Band 6 the most extended emission is also smaller than the largest angular scale of the observations, in all cases, except for the B6 continuum of the western component of AS2UDS 0051.0. Thus, we may miss a small fraction of the flux in the Band 6 observation of AS2UDS 0051.0, although (as described above) the parameterisation of the uv-amplitude data and resulting source size are robust. A more detailed discussion of AS2UDS 0051.0 is presented in Section 4.3.1. Table 4.1 gives a summary of all measured sizes.

Figure 4.4 compares the size of the emission regions of the different gas/dust tracers for each galaxy. The mean emission region sizes are $0.47'' \pm 0.10''$ for [C II], $0.48'' \pm 0.14''$ for [N II], and $0.32'' \pm 0.08''$ and $0.44'' \pm 0.20''$ for the Band 7 and Band 6 continuum, respectively. On a galaxy-by-galaxy basis the sizes of the Band 6, Band 7 and [N II] emission regions are broadly consistent with each other. However, the [C II] is emitted from a region that is on average a factor of 1.47 ± 0.13 larger than the Band 7 continuum. This result is in agreement with Gullberg et al. (2018), which found [C II] to rest-frame 160 μm size ratio of 1.6 ± 0.4 for a sample of four SMGs (including ALESS 65.1, which is included in our study), and results from the CRISTAL survey (Herrara-Camus et al. in prep)

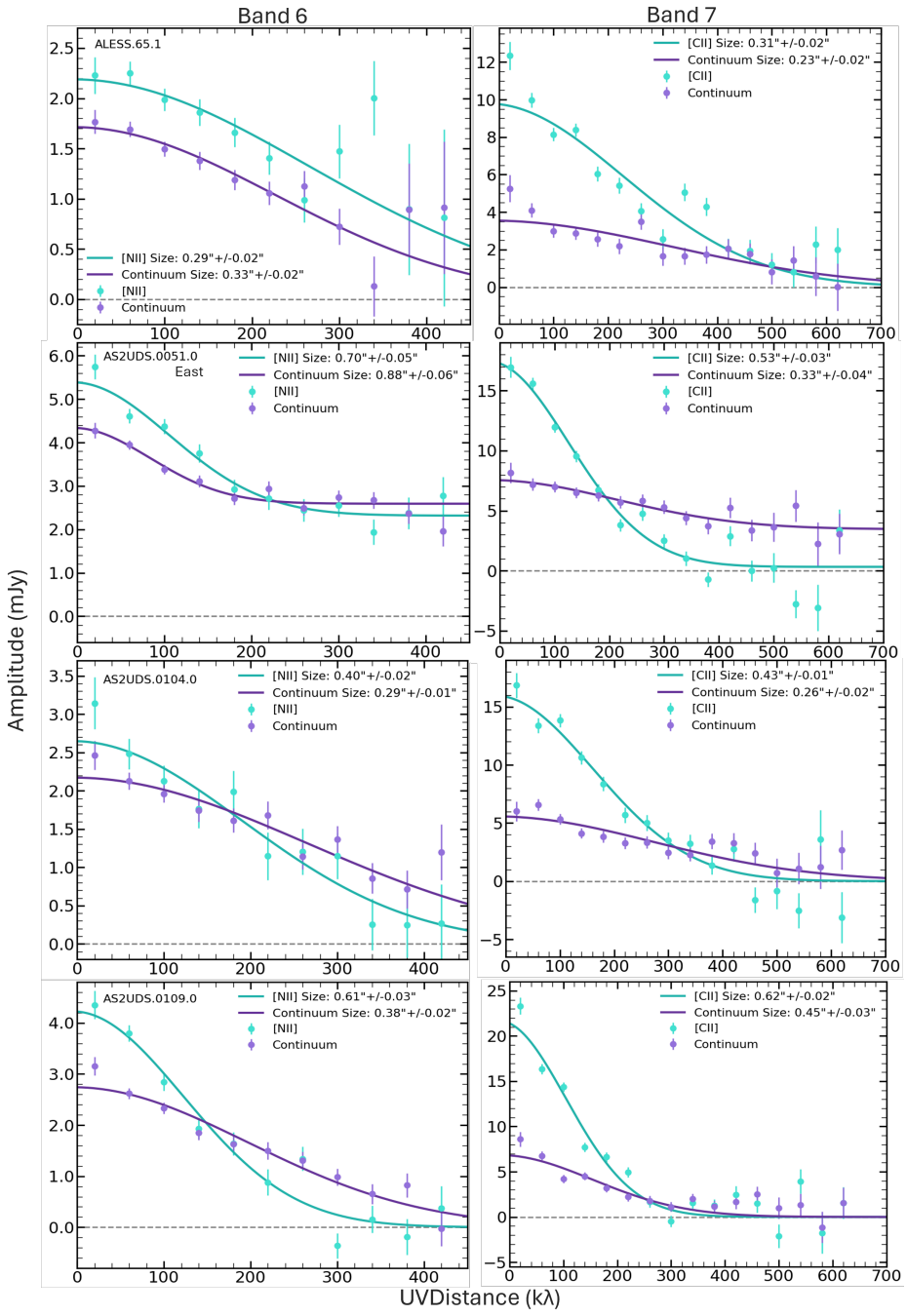

Figure 4.3: *uv*-amplitude plots showing the signal strength at different baselines for the Band 6 (*left*) and Band 7 (*right*) data. Each row shows the data for a single $z \sim 4.5$ SMG. The continuum emission in each band is shown in purple and the line emission ([N II] in Band 6, [C II] in Band 7) is shown in cyan. Curves show the best-fit Gaussian functions from which the size of each dust/gas component is derived as discussed in Section 4.3. For all galaxies with reliable measurements, the [C II] emission is more extended than the continuum (i.e. more extended emission has a smaller FWHM), which is consistent with previous studies of [C II] and dust continuum.

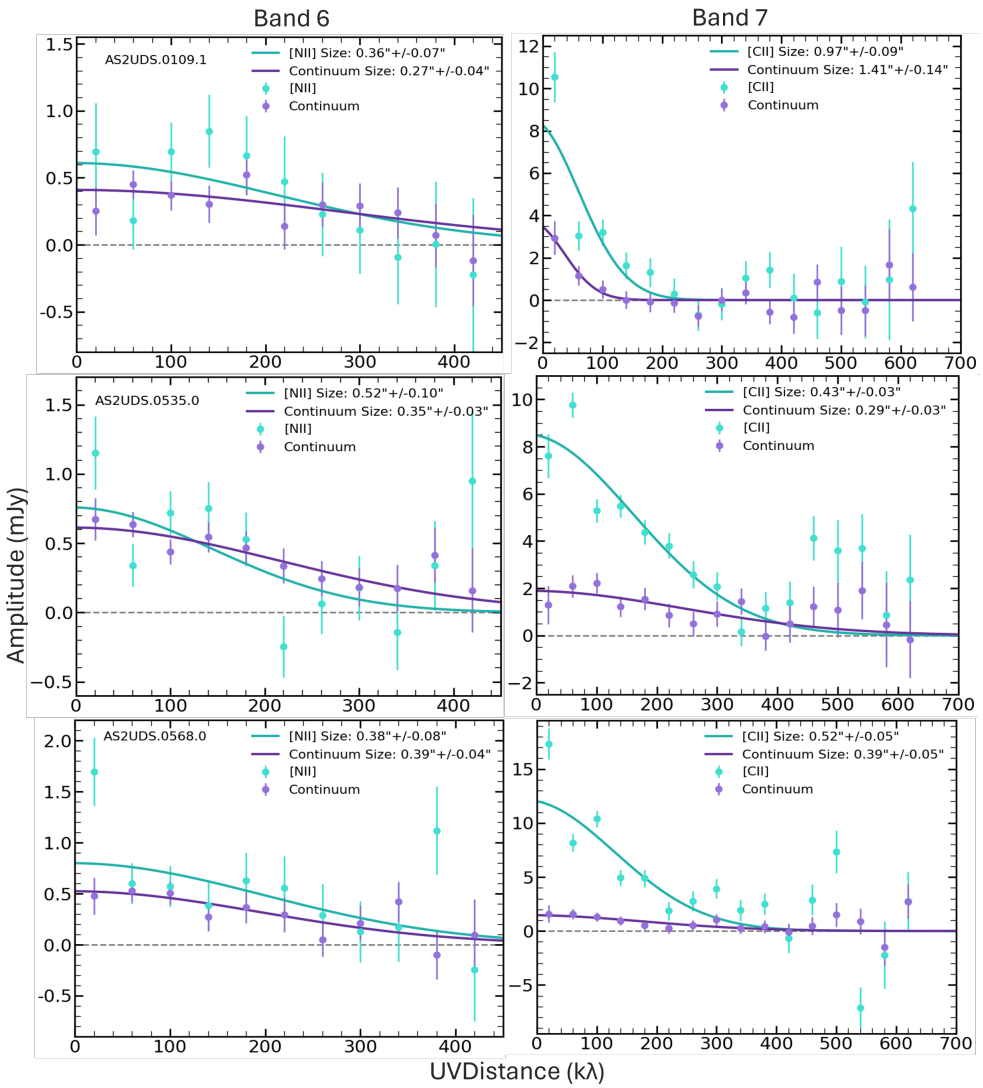

Figure 4.3 (Continued)

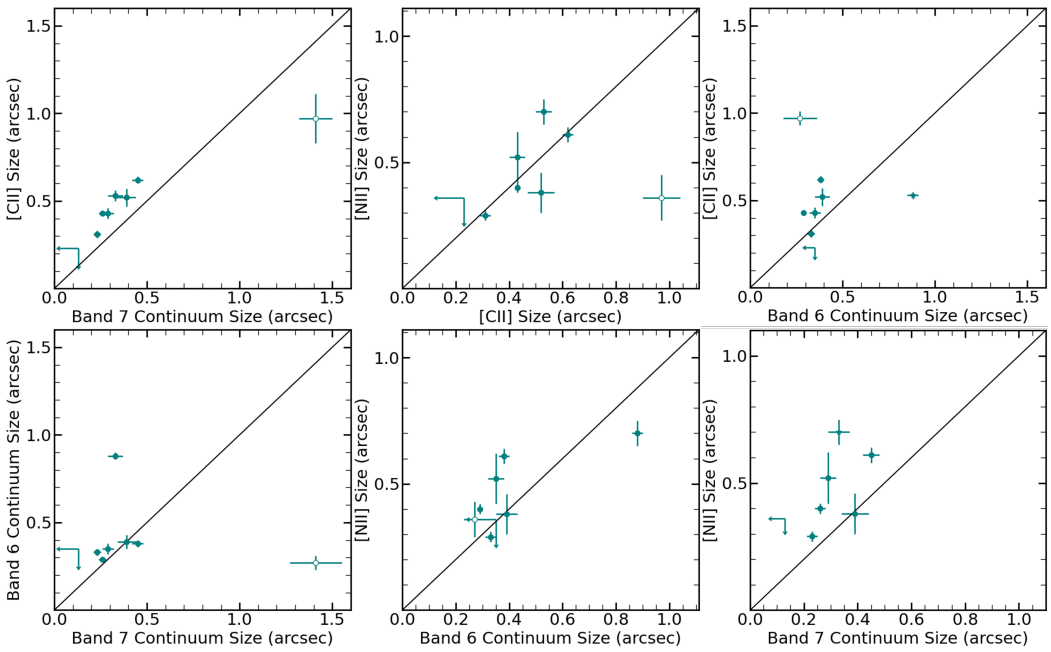

Figure 4.4: Comparison of the sizes of different emission regimes detected in our targets. The open point represents AS2UDS 0109.1 which resides in the noisy edge of the FOV and is thus unreliable. The measured upper limits on the unresolved component of AS2UDS 0051.0 are shown with arrows (Section 4.3.1). The black line shows the one-to-one relation. The top left plot shows that the [C II] emission is more spatially extended than the Band 7 continuum by a factor of 1.47 ± 0.13, and the bottom right panel shows that the [N II] emission region is 1.38 ± 0.27 larger than the Band 7 continuum while all other emission types are of comparable sizes.

which find an average $R_{e,[CII]}/R_{e,FIR}$ ratio of 1.54 ± 0.63 for star-forming galaxies at $z = 4 - 6$ (Ikeda et al., 2024) They however measure an average [C II] size of 1.9 ± 0.77 kpc, i.e. significantly smaller than our results. We note their higher average redshift ($z \sim 5.2$) than ours and difference in targeted population, both of which could be cause for a difference in measured physical sizes. Results from other galaxy types including QSOs and LBGs across the redshift range $3 < z < 6$ also show this (Wang et al., 2013a; Capak et al., 2015; Kimball et al., 2015; Díaz-Santos et al., 2016; Nesvadba et al., 2016; Jones et al., 2017; Umehata et al., 2017; Venemans et al., 2017).

[C II] traces multiple gas phases (e.g. Wolfire et al. 2022) as measured in Chapter 3, whereas [N II] can only be excited in ionised regions (e.g.Oberst et al. 2006; Decarli et al. 2014) and most far-IR continuum flux from SMGs typically traces compact star-forming regions (Hodge & da Cunha, 2020). Thus, the [C II] emission (which traces both ionised and neutral gas) is expected to be more extended than the dust emission, which is consistent with our results. The average ratio of the [N II] size to the Band 7 continuum size is 1.38 ± 0.27, which indicates that both the ionised and neutral gas is more spatially extended than the regions of dusty of star-formation in $z \sim 4.5$ SMGs.

4.3.1 Size measurements in AS2UDS 0051.0

AS2UDS 0051.0 is a complex source, comprised of two components (east and west; Figure 4.1). Analysis of the *uv*-plane shows that the eastern component contains both a point-like source and an extended object. This can be seen in Figure 4.3, where both continuum and the [N II] emission require a Gaussian (extended) component with a y-axis offset (point source) to fit the data.

To investigate the size of the point-like component we first subtract the amplitude of the point source (i.e. the y-axis offset) from the *uv*-amplitude data. We then individually add Gaussians of widths from 0.4″decreasing in steps of 0.05″(and then fine tuning in steps of 0.1″) and with amplitudes equal to that of the removed point source. In the *uv*-plane spatially small sources appear as broad signals (or a flat, horizontal line for point-like sources). Therefore, the upper limit on the size of the point-like component is given by the narrowest Gaussian that

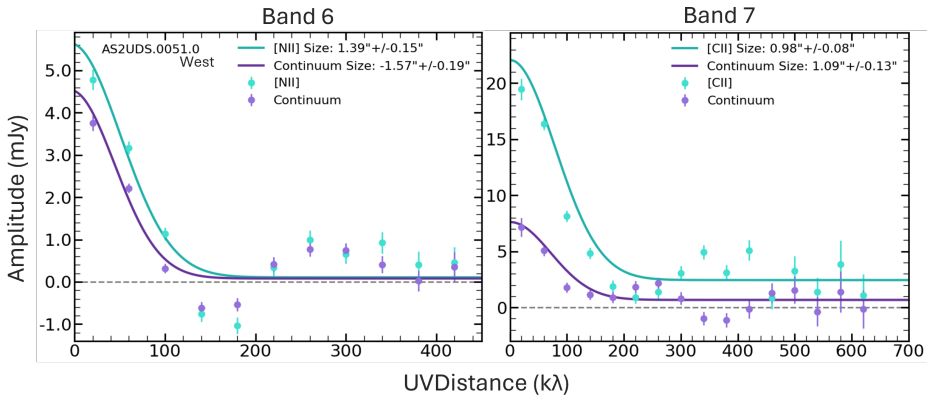

Figure 4.5: *uv*-amplitude plot for the western component of AS2UDS 0051.0.

is consistent with the subtracted data being fit by a single non-offset Gaussian. i.e. the limit wherein the added component would appear to be point-like when fitting the *uv*-amplitude data. These measurements show that the point-like component in AS2UDS 0051.0 is $< 0.36''$ (< 2.4 kpc) and $< 0.35''$ (< 2.4 kpc) in size in the [N II] emission and Band 6 continuum, respectively. Our Band 7 data are higher resolution and therefore more tightly contstrain the size of this component to be $< 0.23''$ (1.6 kpc) and $< 0.13''$ (0.9 kpc) in [C II] and the Band 7 continuum, respectively.

Gullberg et al. (2019) performed *uv*-plane analyses of significantly higher-resolution [C II] data in 153 $z \sim 3$ SMGs and identified similar features in 119 of their sources, whereby the *uv*-amplitude plots do not reach zero at large *uv* baselines. Gullberg et al. (2019) found that these systems were better fit by Sérsic functions with $n = 1$ than Gaussians, which results in smaller measured sizes. However, in this study we are primarily interested in the relative sizes of the different dust and gas tracers and therefore we do not perform Sérsic fits for AS2UDS 0051.0.

We also generate *uv*-amplitude plots (Figure 4.5) that are centred on the western component of AS2UDS 0051.0. However, the amplitude of the signal at small *uv* distances (i.e. the total flux) indicates that emission from both components is included in such an analysis. Since the eastern component is significantly brighter than the western (Figure 4.1) this makes it challenging to disentangle the emission from each component in such an analysis. We therefore do not consider

the western component separately hereafter. Additionally we note is that the amplitude of the the [C II] when measured from the west component is higher than when measured from the east, despite the east being brighter in the image plane. The amplitudes do agree with each other within their uncertainties and with the flux measured in Chapter 3 indicating that the measured flux is across both components. This is explained by the fact that the amplitude peaks at the shortest *uv*-distances (i.e. the left hand side of the plot) which are sensitive to the most extended emission. This makes disentangling the emission coming from each component, and any connecting material, difficult in these plots. As such we only show the *uv*-amplitude plot from the east component as this contains the peak emission location across all types measured.

4.4 [C II] dynamics

We next explore the three dimensional dynamical information that is included in spectral observations with ALMA. The SNR of the [N II] lines in our sample are too low to reliably measure and model dynamics, so we focus on the [C II] information in this section.

4.4.1 Modelling

We begin by creating moment 1 maps of the [C II] emission for the six our targets with high SNR (excluding AS2UDS 0109.1) and visually confirm that many exhibit smooth velocity gradients reminiscent of rotating disks (Figure 4.6). To quantify any rotation and investigate dynamical masses and rotational support we extract slices from this velocity map along the axis of the largest velocity gradient. These slices are the length of the beam ($\sim 0.4''$) and are 1 pixel ($\sim 0.04''$) wide. We fit as many slits across the length of the galaxy as possible.

We calculate the average velocity within each slit and plot it as a function of its distance in arcseconds from the centre of rotation. Where slits overlap masked regions (areas with pixel values $> 3\sigma$, white areas in left panel of Figure 4.6) the average is calculated from unmasked pixels only. We then fit the resulting rotation

curves with a tanh function and measure the value of v_2 from the model (where v_2 is the rotational velocity at twice the effective radius). We use the value of r_e measured in Section 4.3.

Figure 4.6 shows the moment 1 maps overlaid with the positions of the slices from which velocity was measured, next to the resulting rotation curve. Where galaxies have no tanh function plotted on their rotation curve, a fit was not found and the source is likely dispersion dominated. We are unable to measure the velocity dispersion in the rotationally supported galaxies as there are insufficient points lying on the flat parts of the roataion curve to get a reliable measure. This is because the velocity dispersion measurement is affected by beam smearing in the steep part of the rotation curve.

For AS2UDS 0051.0, which is comprised of two galaxies (see Section 4.2), we measure the velocity of each component individually finding one to be rotating and the other to be likely dispersion dominated.

4.5 Masses of the different components of $z \sim 4.5$ SMGs

We next use our measured velocities to constrain the dynamical masses of our $z \sim 4.5$ SMGs and compare these to the gas, dust and stellar masses. Stellar masses from Birkin et al. (2021) are used for ALESS 65.1 and from Dudzevičiūtė et al. (2020) for the AS2UDS sources; all other masses are calculated as described below. Table 4.2 summarises the gas, dust, stellar, and dynamical masses of each of the seven $z \sim 4.5$ SMGs studied here.

Gas masses are calculated using Equation 2 in Vizgan et al. (2022), which uses the [C II] luminosity and is given as:

$$\log(\mathrm{L_{[CII]}}) = (1 \pm 0.01)\log(\mathrm{M_{gas}}) - (1.35 \pm 0.1) \tag{4.2}$$

and we rearrange for $\mathrm{M_{gas}}$. This gas mas calibration is calculated using data from the ALPINE survey (Le Fèvre et al., 2020; Dessauges-Zavadsky et al., 2020), which targets galaxies at $4 < z < 6$, i.e. similar to our targets.

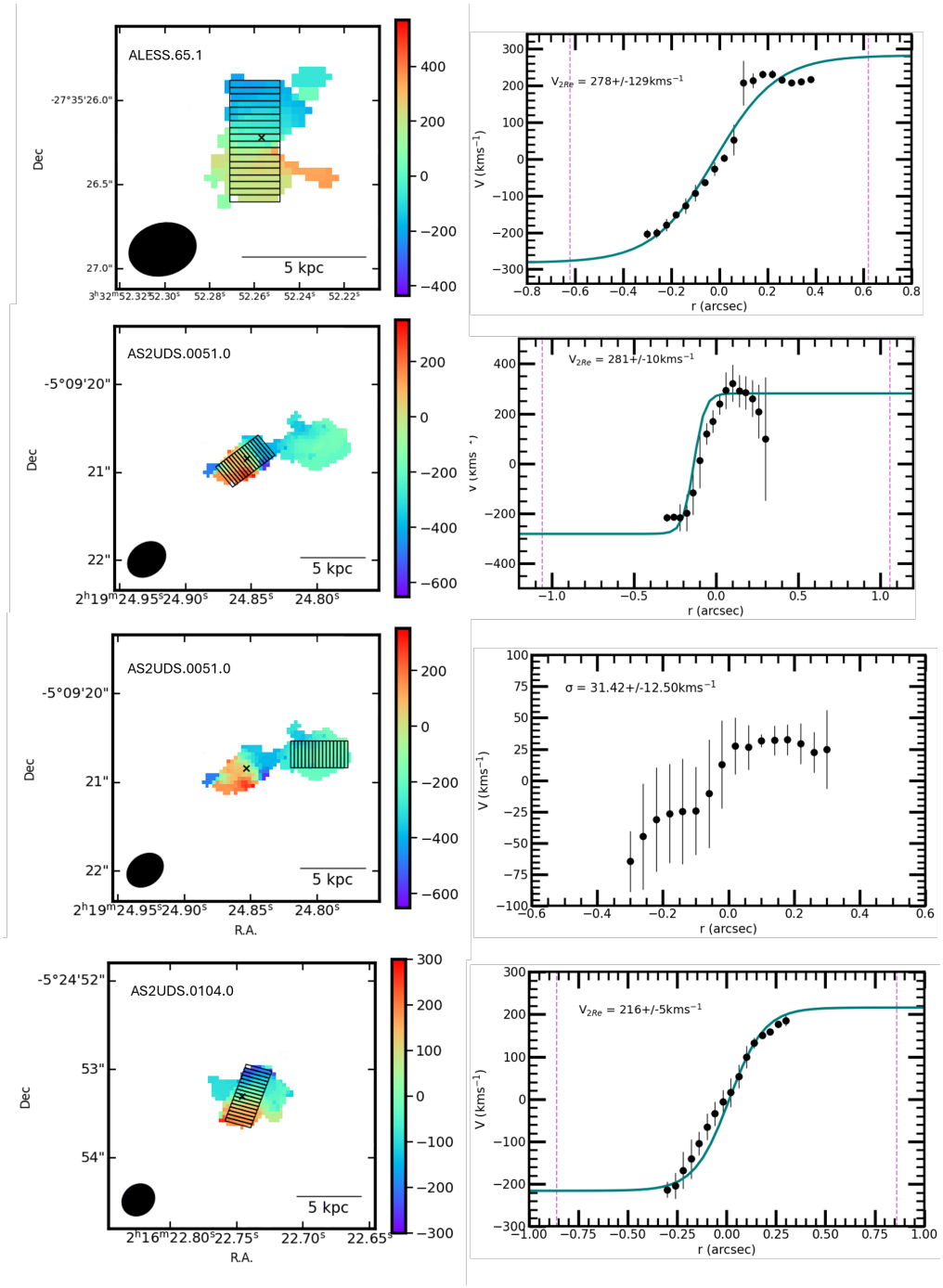

Figure 4.6: *Left:* Moment 1 maps generated by CASA where only pixels with values $\geq 3\times$ the RMS noise level are shown. Overlaid are the slits used for extracting average velocity slices. *Right:* Rotation curve from extracted data with tanh fit (solid teal line). The pink dashed line marks $2r_e$, where v_2 is measured from the tanh fit. All cutouts are $5\times$ the measured [C II] size from Section 4.3 and are centred on the centre of the Band 7 observations. In each map the black 'x' shows the position of the peak [C II] emission, and the beam size is shown by the black ellipse in the bottom left.

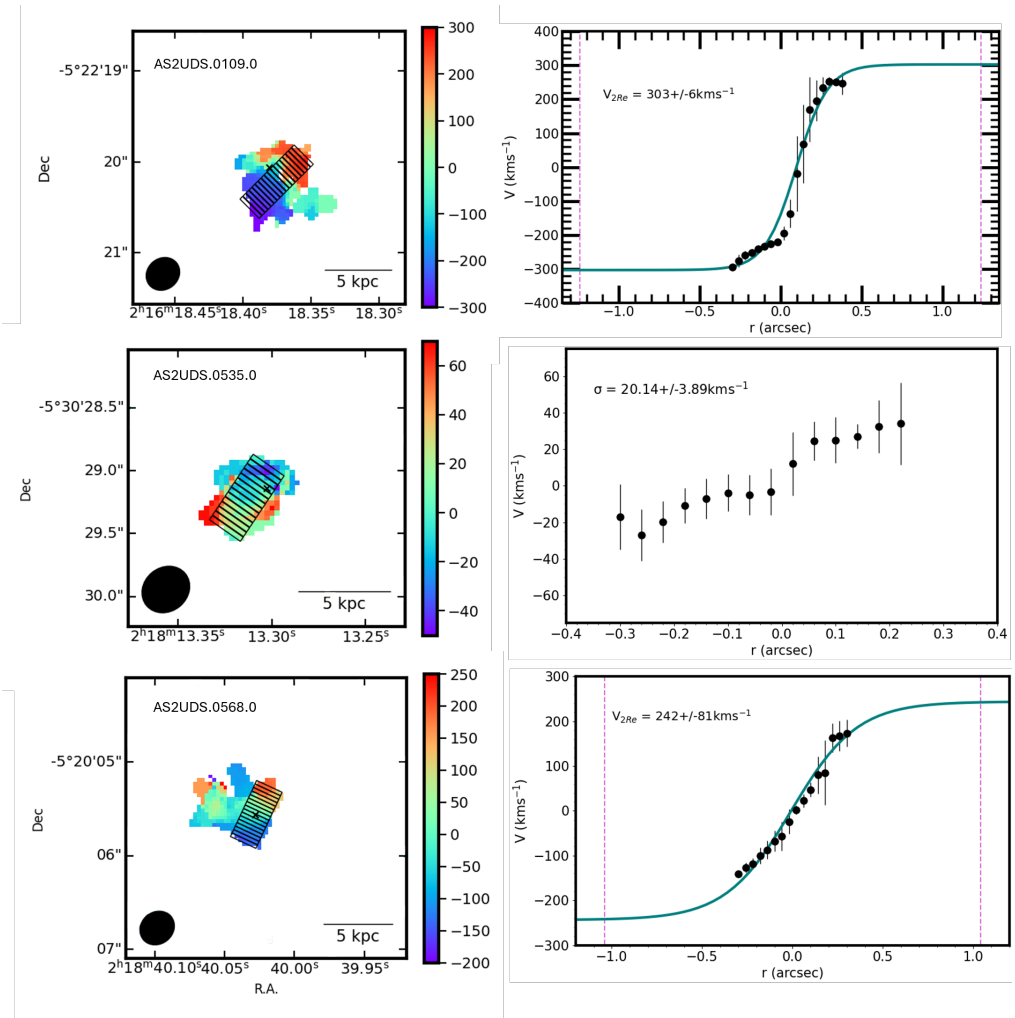

Figure 4.6 (Continued)

To calculate dust masses (M_d) we use Equation 1 in Cooke et al. (2018), which is given by:

$$M_d = \frac{S_{870} D_L^2}{\kappa B_v (1+z)} \tag{4.3}$$

where S_{870} is the rest frame 870 μm flux, D_L is the galaxy's luminosity distance and B_v is the Planck function. The dust temperatures that we use for this calculations are taken from Cooke et al. (2018) for the AS2UDS sources and da Cunha et al. (2015) for ALESS 65.1. Rest-frame 870 μm fluxes are calculated using measurements of the Band 7 continuum fluxes 2.1 and $\beta = 1.8$. We also assume $\kappa = 0.077\,\mathrm{m^2 kg^{-1}}$ (Dunne et al., 2000) for the purposes of calculating the dust masses.

Dynamical masses M_{dyn} are calculated using Equation 4 in Stott et al. (2016) but substituting $v_{2.2}$ and $r_{2.2}$ for the values we measure from moment 1 maps, v_2 and r_2 respectively, after correcting for inclination angle. We correct our observed rotational velocities for the effect of inclination angle using

$$V_2 = \frac{v_2}{\sin(i)} \tag{4.4}$$

Where i is calculated using Equation 1 in Harrison et al. (2016) using the average value of $\frac{b}{a}$ from Gillman et al. (2023) (~ 0.55). This provides an estimated inclination angle of 58 deg.

The new equation for dynamical mass is then given by:

$$M_{dyn}(< r_2) = \frac{V_2^2 r_2}{G} \tag{4.5}$$

where G is the gravitational constant and V^2 is the corrected rotational velocity from Equation 4.4.

For galaxies assumed to be dispersion dominated we calculate their mass using:

$$M_{dyn}(< r_2) = \frac{\alpha \sigma^2 r_2}{G} \tag{4.6}$$

where σ is the velocity dispersion and α is a constant.

The masses of the different components of each $z \sim 4.5$ SMG are presented in Table 4.2. The median gas-to-dust mass ratio is 102±71, which is consistent with values from Swinbank et al. (2014) and Scoville et al. (2016).

We can also use the results of Amvrosiadis et al. (2023) to verify our measurements. Amvrosiadis et al. (2023) performed a kinematic analysis of CO emission from 12 SMGs, including ALESS 65.1 using the CO(4–3) line and modelling the data directly in the *uv*-plane. Our results for ALESS 65.1 are in agreement with those from Amvrosiadis et al. (2023) in terms of both rotational velocity and dynamical mass, though we note the large uncertainty on this galaxies rotational velocity and thus dynamical mass as a result of a poorly constrained tanh fit.

Having calculated the dynamical masses (i.e. total mass) and the masses of all the baryonic components of the galaxies we next calculate the dark matter fractions.

To calculate the dark matter fraction ($f_{\rm DM}$) we use equation 7 from Birkin et al. (2021), which can be rearranged to give:

$$f_{\rm DM} = 1 - \frac{\rm M_* + M_{gas}}{\rm M_{dyn}} \tag{4.7}$$

where $\rm M_*$ is the stellar mass, $\rm M_{gas}$ is the gas mass and $\rm M_{dyn}$ is the dynamical mass. We measure $f_{\rm DM} = 0.507$ for ALESS 65.1 and $f_{\rm DM} = 0.28$ for AS2UDS 0568.0, in agreement with results from e.g. Price et al. (2016); Wuyts et al. (2016); Genzel et al. (2017); Smith et al. (2020) and Lovell et al. (2018). For the rest of our galaxies however we obtain unphysical (negative) values of $f_{\rm DM}$. There are a number of reasons that could explain this, firstly is that for some sources (e.g. AS2UDS 104.0 and AS2UDS 109.0) we may be underestimating the inclination angle and thus a bigger correction is needed. This is plausable given their less elliptical appearance on the moment 1 maps. Secondly, for the 'dispersion dominated' galaxies the dynamical masses appear to be underestimated, given that the calculated values are less than their gas masses, indicating that more data could be needed to truly measure the extent of the velocity dispersion within them, or that additional fine tuning is needed of the α parameter in Equation 4.6. For AS2UDS 0051.0 we sum the masses of the two components.

Table 4.2: Masses of the different galaxy components for the $z \sim 4.5$ SMGs, calculated as described in Section 4.5.

Source	Gas Mass $10^{11}\,M_\odot$	Dust Mass $10^{9}\,M_\odot$	Stellar Mass $10^{10}\,M_\odot$	Dynamical Mass $10^{11}\,M_\odot$	Gas/Dust Ratio	T_{depl} Myr	μ_{gas}
ALESS 65.1	0.66 ± 0.16	1.90 ± 0.09	$3.02^{+1.66}_{-0.78}$	1.95 ± 1.81	34.6	63.3	2.19
AS2UDS 0051[a].0	2.53 ± 0.60	2.36 ± 0.35	$5.50^{+2.63}_{-1.42}$	2.76 ± 0.20	107	225	4.60
AS2UDS 0104.0	1.63 ± 0.39	2.17 ± 0.10	$6.76^{+6.42}_{-3.29}$	1.07 ± 0.05	75.1	152	2.41
AS2UDS 0109.0	2.09 ± 0.50	2.16 ± 0.17	$1.00^{+0.17}_{-0.18}$	1.87 ± 0.07	97.0	175	20.9
AS2UDS 0109.1[b]	0.23 ± 0.29	0.65 ± 0.14	$5.37^{+4.63}_{-2.42}$	...	34.9	48.7	0.43
AS2UDS 0535.0	0.99 ± 0.24	0.37 ± 0.07	$0.23^{+2.22}_{-0.00}$	0.02 ± 0.007	269	271	43.0
AS2UDS 0568.0	1.21 ± 0.29	0.31 ± 0.07	$2.88^{+1.38}_{-0.66}$	1.72 ± 1.15	329	329	4.20

[a] Dynamical mass is the sum of both components.s [b] AS2UDS 0109.1 is not detected with high enough SNR to perform dynamical modelling.

4.6 Evolutionary views on SMGs

4.6.1 SMGs at different epochs

We next compare our results with studies of SMGs at different epochs. We have measured median sizes for all sources as follows; [C II] sizes of $0.48'' \pm 0.05''$ (3.2 ± 0.7 kpc), [N II] sizes of $0.46'' \pm 0.08''$ (3.2 ± 0.94 kpc), Band 7 continuum sizes of $0.31'' \pm 0.04''$ (2.2 ± 0.5 kpc), and Band 6 continuum sizes of $0.37'' \pm 0.08''$ (3.0 ± 1.4 kpc), where physical sizes are calculated at $z = 4.5$ and uncertainties are calculated by bootstrapping. The dust continuum sizes for our $z \sim 4.5$ SMGs are consistent with the observed-frame 870μm (Band 7) continuum sizes of 0.5″measured by Gullberg et al. (2019) (extended component, see paper) for a sample of SMGs at median $z = 2.9 \pm 0.1$. Our sizes are also consistent with [C II] and Band 7 continuum sizes of $0.65'' \pm 0.15''$ and $0.32'' \pm 0.03''$, respectively, measured by Gullberg et al. (2018) for in a sample of four $z = 4.5$ SMGs with 0.03″resolution observations. We therefore support the conclusion from Gullberg et al. (2018) that there is no significant size evolution in SMGs between $z \sim 4.5$ and $z \sim 2$.

Our sample has a median gas fraction (μ_{gas}=M$_{gas}$/M$_{stellar}$) of $4.2^{+43.0}_{-0.43}$ where the stated error is the uncertainty on the median, which is calculated by bootstrapping. This value is significantly larger than the result from Birkin et al. (2021) ($\sim$ 1.5 for SMGs at $z \sim 4.5$) although we note the large upper uncertainty. This may be caused by a large measured μ_{gas} from AS2UDS 0535.0 as seen in Table 4.2. The z_{phot} in Dudzevičiūtė et al. (2020) is poorly constrained which may lead to an inaccurate value of M$_{stellar}$. Even still these systems appear to be very gas rich compared to other SMGs at this epoch.

By assuming 100% star formation efficiency and no regeneration of gas we calculate that the $z \sim 4.5$ SMGs have median gas depletion timescales of 176 ± 59 Myr, which is consistent with the results from Birkin et al. (2021) (210 ± 40 Myr) who also find a moderate decline from $z \sim 2.5 - 5$.

4.6.2 The origin of SMGs

The gas depletion timescales calculated for our $z \sim 4.5$ SMGs (Section 4.6.1) are also consistent with the 'normal' star forming galaxies detected in [C II] by the ALPINE survey (Le Fèvre et al., 2020). This is consistent with the result from Scoville et al. (2016) that gas depletion times are similar for galaxies that are both on and above the main sequence at $z > 1$, which is indicative that the mode of star formation at high redshifts is different than that at low redshift, in that star formation is generally more rapid for all galaxies at $z < 1$.

Conversely, if SMGs do represent a short-lived phase of starburst activity, then a trigger for their high star-formation rates is required, for which observational evidence is discussed in Section 1.5.2. Predictions from simulations differ. For instance, Hayward et al. (2013) identify mergers as the predominant cause, but Hopkins et al. (2013) and Cowley et al. (2015) predict that SMGs are driven by secular processes, wherein gas flows inwards to a central high density star forming region where high gas densities fuel rapid star formation. The Hopkins et al. (2013) scenario takes place in the late stages of a merger where the gas has relaxed back into a disk. It is particularly efficient in galaxies with high gas fractions (and few pre-existing stars) as these galaxies are inefficient at losing angular momentum and so are able to reform into larger disks post-merger (Hopkins et al., 2013).

The secular evolution or post-merger scenario is supported by our measurements of of [C II] and [N II] sizes (tracing both ionised and neutral, and ionised only gas, respectively) being a factor of $\sim 1.5\times$ and $\sim 1.4\times$ larger than the measured dust continuum size, which traces recent star formation (Section 4.3). In addition, the dust appears less morphologically complex than the gas (Figure 4.1) and there are offsets in the peak positions of the different gas and dust tracers (Figure 4.2), which could be explained by the gas being channelled into compact star forming regions. Therefore, it is plausible that our $z \sim 4.5$ SMGs may have been subject to recent major or minor mergers (e.g.Hernquist & Mihos 1995; Naab & Burkert 2003; Cox et al. 2008; Younger et al. 2008, even though only AS2UDS 0051.0 appears to be currently undergoing a major merger (Section 4.3.1).

However, as pointed out by Gullberg et al. (2019), the merger scenario requires galaxies with large gas reservoirs to have already assembled and have undergone a merger ~ 1 Gyr prior to observe a starbursting nucleus and gas envelope. At $z \sim 4.5$ the Universe is only ~ 1.3 Gyr old, so for galaxies like our targets the required speed of mass build up is significant. As such it is unlikely that prior major mergers such as those described in Hopkins et al. (2013) is the cause of the elevated star formation in these sources.

We note that similar features of centrally compacted star formation can be caused by tidal interactions (e.g. Barnes & Hernquist 1992 and references therein; Gnedin 2003), and spontaneously or tidally induced bars (e.g. Sakamoto et al. 1999; Peschken & Łokas 2019), and thus we cannot distinguish between secular and dynamical processes here, but our data are consistent with both scenarios.

4.6.3 The fate of SMGs

Hodge et al. (2016) undertook high resolution observations of the dust continuum in a sample of SMGs with median $z = 2.6 \pm 0.5$. The SMGs in Hodge et al. (2013) have effective radii and stellar masses that are consistent with local elliptical galaxies from ATLAS^{3D}. The mean dust continuum radius and stellar mass of our sample of $z \sim 4.5$ is also located centrally within the scatter of the ATLAS^{3D} galaxies at their current time and will remain so if they follow the path along the M_* - R_e plane predicted in Hodge et al. (2016).

Our $z \sim 4.5$ SMGs have a median gas depletion timescale of 176 ± 59 Myr (Section 4.6.1). Sherman et al. (2020) show that at high redshifts, massive galaxies have less accretion of cool gas from the IGM and those that reside in turbulent environments are likely to have their SFR enhanced, and subsequently deplete their gas reservoirs leading to a sharper cutoff into quiescence producing the massive quenched galaxies we observe at high z. As such, if we assume their depletion timescales to be a true representation of their lifespans, these sources will have depleted their gas reservoirs and reached quiescence by $z \sim 4$ (see also Rizzo et al., 2021). While populations of quiescent galaxies do exist at that epoch (e.g. Glazebrook et al. 2017; Tanaka et al. 2019; Valentino et al. 2020) they appear to be rare. Far more populous are quiescent galaxies around cosmic noon, many of

which are characterised by being massive, compact and having had their stellar mass build up in a short rapid burst (e.g. Toft et al. 2014; van Dokkum et al. 2015; Stockmann et al. 2021). To assess links between the $z > 4$ SMGs and $z \sim 2$ quiescent galaxies we measure the internal stellar mass surface densities, given by

$$\Sigma = 0.5 M_* / \pi r_e^2 \tag{4.8}$$

and compare the value for our sample to that for $z = 2$ compact quiescent galaxies (CQGs). Toft et al. (2014) measure a mean $\log(\Sigma)_{CQG} \sim 9.8 \pm 0.1\,\mathrm{M}_\odot\,\mathrm{kpc}^{-2}$ at $z \sim 2$. We use our measured Band 7 continuum sizes for this analysis, as in Toft et al. (2014). For this sample of $z \sim 4.5$ SMGs we measure a mean $\log(\Sigma)_{SMG} = 9.98^{+0.9}_{-0.12}\,\mathrm{M}_\odot\,\mathrm{kpc}^{-2}$ placing our results in agreement with both results for $z > 3$ SMGs and $z \sim 2$ CQGs from Toft et al. (2014), supporting a theory of passive evolution from starbursting to quiescent. Additionally the number density of [C II] detected SMGs that we measure in Section 3.3 (which we can treat as a lower limit for both [C II] emitters and $z \sim 4.5$ SMGs) places the number density of SMGs in agreement with the measured number density of CQGs at $z \sim 2$ ($\gtrsim 0.7 \times 10^{-6}\,\mathrm{Mpc}^3$ for SMGs and $6.0 \pm 2.1 \times 10^{-5}\,\mathrm{Mpc}^3$ for CQGs (Toft et al., 2014). It is also expected that the measured number density of SMGs will be less than that of CQGs as the SMG phase is short lived and thus galaxies only meet the selection criteria for a short amount of time (Toft et al., 2014). This effect can be corrected for by considering the difference in the lifetime of an SMG and the timespan over which the comparison sample exists. The comparison sample spans a range of $\sim 500\,\mathrm{Myr}$ (Krogager et al., 2014) and the duty cycle of an SMG is measured to be $\sim 42^{+33}_{-15}\mathrm{Myr}$ (Toft et al., 2014). This gives the number density a correction factor of ~ 12 giving a corrected number density of $\gtrsim 8.4 \times 10^{-5}\,\mathrm{Mpc}^3$, placing it in agreement with the number density of $z \sim 2$ CQGs.

4.7 Conclusions

In this Chapter we have analysed the resolved properties of a sample of seven SMGs detected in both [C II] and [N II] using Band 7 and Band 6 ALMA data. We processed the data to enhance the sensitivity to extended emission to reach

resolutions of 0.4″(Section 2.4). We identified the peak positions of different gas and dust tracers ([C II], [N II], and dust continuum) using moment 0 maps and measured their sizes in the *uv*-plane. We also performed a kinematic analysis and investigated the potential origins and evolutionary pathways of the extreme star formation in SMGs. Our main findings are:

- The size of the [C II] emission is a factor of 1.47 ± 0.13 larger than the continuum, and the [N II] also extends beyond the dust emission by a factor of 1.38 ± 0.27. This supports theories of compact star formation within SMGs being a result of large gas disks channelling fuel for star formation into a more central nucleus. Offsets in the peak position of the [C II] and [N II] from the centrally located dust continuum also support this theory.

- Measured sizes, μ_{gas} and gas depletion timescales are consistent with results from SMGs at later epochs, and with predictions for μ_{gas} and gas depletion timescales at $z = 4.5$, indicating that this sample is likely representative of the SMG population at this redshift.

- If the galaxies that we target are late stage mergers that have reformed their gas disks then this would require gas rich, low stellar mass progenitors to exist ~ 1 Gyr prior (at $z \sim 12$). Given that this is unlikely so early in the Universe it is more likely that environmental effects are the cause of enhanced star formation in high-z SMGs that exhibit rotating disks.

- The measured number densities and mass-size relations are in agreement with the properties of $z \sim 2$ quiescent galaxies, providing additional evidence for an evolutionary link between these two populations.

Chapter 5

Conclusions

In this thesis we used Band 6 and 7 ALMA observations to investigate a sample of 12 SMGs with the aim of investigating their triggering mechanisms, assessing links between them and lower redshift massive elliptical galaxies, and also the properties of their [C II] emission with respect to the [C II] deficit, using the [N II] 205μm line. This chapter summarises our conclusions and outlines possible future work in this area.

We performed a custom data reduction on the observations outlined in Chapter 2, with the aim of robustly measuring the flux. We created an algorithm to identify individualised regions from which to extract line flux to optimise trade-offs between flux and SNR for our sample. Out of the 12 galaxies observed, six of the targets are detected in both [C II] and [N II] and are confirmed as being at $z \sim 4.5$. We detect [C II] and [N II] serendipitously in one additional SMG which was not targeted by our observations but was within the field of view of one of the targets, physically associating the pair as being at the same redshift (these are AS2UDS 109.0 and AS2UDS 0109.1). Of the targeted SMGs that were not detected in [C II] and [N II] AS2UDS 0243.0 has a detection in Band 7 at the expected frequency for [C II] at $z \sim 4.5$ but no corresponding [N II] detection. This lack of [N II], paired with its multiwavelength data leads us to believe this source is at $z = 1.63 \pm 0.01$ and the line we detect is CO(8–7). Another, AS2UDS 0643.0, has a line detection in Band 6, but it is offset in frequency from that which we

expected for [N II] at $z \sim 4.5$. An assessment of potential line identities in combination with its photometric redshift leads us to identify the detected line as [N II] 205 μm, but at a redshift of $z = 4.98 \pm 0.01$. We would not detect [C II] in this source as the line is redshifted out of the frequency coverage of Band 7. For the remaining four sources we detect no line emission and conclude that the original detections were spurious. Finally, we detect another five additional sources (excluding the one mentioned above detected in [C II] and [N II]), of which two have line detections (243B, detected CO(3–2) at $z = 0.348$ and 568B, detected [C I] 609 μm at $z = 0.93$) and the other three (AS2UDS 0002.0, 535C1 and 535C2) are continuum only.

In Chapter 3 we use the catalogue of seven SMGs to study the nature of the [C II] 158 μm line in $z \sim 4.5$ SMGs. We constrain the [C II] luminosity function using our updated number counts at this redshift finding results that are in agreement with observations from the ALPINE survey (Yan et al., 2020; Loiacono et al., 2021) and simulations from Lagache et al. (2018). We investigate the origin of the [C II] line within the ISM of our sources, finding that it originated mostly from PDRs, with $[\mathrm{C\,II}]_{\mathrm{PDR}}$ ranging from $\sim$ 70–95% in our sources, in agreement with results from other high redshift SMGs (Cunningham et al., 2020; Reuter et al., 2020). We observe deficits in the [C II] and [N II] luminosities with increasing L_{IR} consistent with previous results (Díaz-Santos et al., 2017; Cunningham et al., 2020; Reuter et al., 2020) and go onto find a significant correlation between the [C II] deficit and the [C II]/[N II] ratio across our sources and sources from the literature that span a range of galaxy types. We examine these relationships to determine that the deficit is most likely driven by a reduction in the amount of [C II] emission from PDRs, in agreement with theories from Narayanan & Krumholz (2017). We use the relationship between the [C II] deficit and the [C II]/[N II] ratio to calibrate a correction to the observed [C II] luminosity to correct for the effect of the deficit by using the [N II] luminosity. This corrected value allows for a more accurate SFR, preventing the SFR from being underestimated if the [C II] luminosity is in the deficited regime (i.e. has $L_{\mathrm{IR}} > 10^{11} \mathrm{L}_{\odot}$).

In Chapter 4 we use higher-resolution reprocessed data ($\sim 0.4''$) with increased weighting to extended emission (as described in Chapter 2) to investigate the composition of the seven SMGs, as well as their gas kinematics to investigate

the triggering mechanisms and evolution of $z \sim 4.5$ SMGs. We find that when measuring the sizes of emission types using *uv*-amplitude plots, the size of the [C II] emission is 1.47 ± 0.13 times larger than the Band 7 continuum, in agreement with previous results (Gullberg et al., 2018) and that the [N II] emission is also 1.38 ± 0.27 times larger than the Band 7 continuum. We further find that the location of the [C II] and [N II] emission is offset from the Band 6 and 7 continuum. We find that the measured sizes, gas mass fractions and gas depletion timescales are consistent with results from lower redshift SMGs (Gullberg et al., 2019; Birkin et al., 2021; Amvrosiadis et al., 2023) and that there is little evolution between the populations. We deduce that given the prevalence of rotationally supported gas disks in our sample (with the exception of one source appearing to be undergoing a major merger, AS2UDS 0051.0) that it is unlikely that our sources are late stage mergers given the large timescales involved with reforming a disk after such an event (Hopkins et al., 2013). Finally we conclude that the mass-size relations, number densities and gas depletion timescales measured for our sources are consistent with them being the progenitors of high-redshift massive elliptical galaxies.

5.1 Future Work

The work presented in this thesis aids in understanding a number of ongoing questions in galaxy evolution. Mechanisms behind the [C II] deficit are constrained and a correction provided to account for the deficit. The triggering of the high SFRs seen in SMGs is explored and links drawn between SMGs at high redshift and massive elliptical galaxies. However there is scope for this work to be improved and built upon. In this section we will detail some possible avenues for future research to further the results presented here.

The methodology of combining [C II] and [N II] observations described in Chapter 3 can be expanded to any galaxy for which both lines are accessible, and increasing the number of galaxies with detections of both lines would not only allow the corrections calibrated in Section 3.6 to be improved and constrained further, but also individual corrections specialised to galaxy type or redshift could

be found. However this method is not without caveats, and measurements of the electron density would remove some uncertainty in the expected [C II]/[N II] ratio. As such, observations of the [N II] 122 μm line in these sources (or indeed other SMGs at which the [N II] 122 μm is more accessible, as it happens to fall in a window of atmospheric opacity for these galaxies) would allow the electron density to be constrained (e.g. Oberst et al. 2006) and thus the expected [C II]/[N II] ratio to be more accurately determined.

Within these sources, ALMA observations of additional far-IR emission lines would allow further investigation on the origin of the [C II] deficit. For example, by combining these [C II] and [N II] observations with measurements of [O I] 63 μm the gas density (n) and far UV field strength (G_0) can be constrained (e.g. Wolfire et al. 1990; Kaufman et al. 1999) as well as constraining the electron and hydrogen column densities within PDRs and H II regions using observations of [O I] 146 μm and [N II] 122 μm respectively (e.g. Oberst et al. 2006; Goldsmith 2019). By determining the far UV field strength we would be able to assess theories such as thermal saturation of the [C II] line (e.g. Kaufman et al. 1999; Rybak et al. 2019; Bisbas et al. 2022).

For a more complete account of the ISM in these sources, [C I](2-1) and [C I](1-0) can be used to trace molecular gas and gas density (Popping et al., 2017; Valentino et al., 2020; Papadopoulos et al., 2022), which we could not only perform the cospatiality investigation described in Section 4.2 to assess the location of the molecular gas in relation to dust (and thus star formation) but also compare gas densities with $z \sim 2$ SMGs to begin to search for evolution between the populations in the properties of their ISMs. The power of ALMA data cubes would mean that if we had these line measurements we would also be able to measure the dust continuum at each frequency, allowing the dust temperature to be measured for each source which can be used to improve estimations of $L_{\rm IR}$ and dust masses as described in sections 2.10 and 4.5 respectively.

Since the launch of the James Webb Space Telescope (JWST), its unparalleled resolution at near-IR wavelengths has allowed the rest frame optical and UV counterparts of SMGs to be studied and resolved (Birkin et al., 2023; Gillman et al., 2023). The NIRSpec instrument is able to spatially and spectrally resolve emission lines of $z \sim 4$ SMGs (Birkin et al., 2023) and for the first time measure

optical lines in these sources. Observations of Hα, Hβ, [O III]and [N II]would allow multiple science results that would build on what is presented in this thesis. Kinematics of the Hα line at the 0.1″resolution provided by NIRSpec would allow us to assess the clumpiness and turbulence of the ionised gas and thus sites of star formation in a way that we cannot achieve with the dust continuum. This would build on our analysis of triggering mechanisms, by being able to identify the presence of bars or star formation clumps, aiding us in distinguishing between secular and dynamical triggering mechanisms as discussed in Section 4.6.2.

These data would also allow us to place our sources on a Baldwin, Phillips and Terlevich (BPT; Baldwin et al. 1981) diagram and assess the presence of AGN in these sources. Knowing the AGN content of high redshift SMGs has multiple benefits; first the AGN fraction in SMGs is not agreed upon, with measurements ranging from $\sim 15\%$ (Stach et al., 2019) and $\sim 60\%$ (Birkin et al., 2023). Knowing the AGN content of our sources allows us to identify the dominant source of ionising radiation. Additionally, the presence of AGN would imply the presence of X-rays, which are able to ionise carbon into higher excited states than C+ which would have implications for the C+/N+ ratio which affects the measured [C II]/[N II] ratio. As such constraining the AGN population within these sources would not only improve our knowledge of SMGs in the scheme of black hole co-evolution, but also reduce uncertainty on results presented in this thesis.

Finally observations of these lines from JWST would allow the metallicity of the sources to be measured. Knowing the metalicity allows a more accurate understanding of the C/N abundance ratio (Zhang et al., 2018) which can also affect the [C II]/[N II] ratio, further reducing systematics in our measurements.

Future work that doesn't require new data include performing a stacking analyses to search for even fainter extended emission such as that seen in Gullberg et al. (2019). Stacking the sources with a disk dominated morphology would further allow detection of even fainter, more extended dust and [C II] emission allowing for a more in depth assessment of the morphology of $z \sim 4.5$ SMGs. Our combined observation could also have an SNR high enough that the [N II] can be fit to provide an averaged view of the motion of the ionised gas and thus the sites of star formation.

Future facilities such as the Atacama Large Aperture Sub-mm/mm Telescope (AtLAST; Klaassen et al. 2020; Ramasawmy et al. 2022) promise to revolutionise SMG research by providing spectral analysis over a wide field of view ($\sim 2\,\mathrm{deg}^2$) which will allow analyses such as these to be performed for large samples of galaxies as opposed to small followup samples which suffer from a lack of spectroscopic redshifts.

References

Algera H. S. B., et al., 2020, ApJ, 903, 138

Álvarez Crespo N., Smolić V., Finoguenov A., Barrufet L., Aravena M., 2021, A&A, 646, A174

Amvrosiadis A., et al., 2023, arXiv e-prints, p. arXiv:2312.08959

Arumugam V., 2013, PhD thesis, University of Edinburgh, UK

Astropy Collaboration et al., 2022, ApJ, 935, 167

Baldwin J. A., Phillips M. M., Terlevich R., 1981, PASP, 93, 5

Barger A. J., Cowie L. L., Sanders D. B., Fulton E., Taniguchi Y., Sato Y., Kawara K., Okuda H., 1998, Nature, 394, 248

Barger A. J., Wang W. H., Cowie L. L., Owen F. N., Chen C. C., Williams J. P., 2012, ApJ, 761, 89

Barnes J. E., Hernquist L., 1992, Nature, 360, 715

Behrens C., Pallottini A., Ferrara A., Gallerani S., Vallini L., 2018, MNRAS, 477, 552

Behroozi P. S., Wechsler R. H., Conroy C., 2013, ApJ, 770, 57

Bell E. F., et al., 2004, ApJ, 608, 752

Bellocchi E., Arribas S., Colina L., 2016, A&A, 591, A85

Biggs A. D., et al., 2011, MNRAS, 413, 2314

Birkin J. E., et al., 2021, MNRAS, 501, 3926

Birkin J. E., et al., 2023, ApJ, 958, 64

Bisbas T. G., et al., 2022, ApJ, 934, 115

Blain A. W., Smail I., Ivison R. J., Kneib J. P., 1999, MNRAS, 302, 632

Bothwell M. S., et al., 2013, MNRAS, 429, 3047

Bournaud F., Elmegreen B. G., 2009, ApJ, 694, L158

Bourne N., et al., 2017, MNRAS, 467, 1360

Bower R. G., Benson A. J., Malbon R., Helly J. C., Frenk C. S., Baugh C. M., Cole S., Lacey C. G., 2006, MNRAS, 370, 645

Bowler R. A. A., Cullen F., McLure R. J., Dunlop J. S., Avison A., 2022, MNRAS, 510, 5088

Brauher J. R., Dale D. A., Helou G., 2008, ApJS, 178, 280

Briggs D. S., 1995, PhD thesis, New Mexico Institute of Mining and Technology

Brinchmann J., Charlot S., White S. D. M., Tremonti C., Kauffmann G., Heckman T., Brinkmann J., 2004, MNRAS, 351, 1151

Bromm V., Coppi P. S., Larson R. B., 2002, ApJ, 564, 23

Bundy K., et al., 2015, ApJ, 798, 7

Calzetti D., 1997, AJ, 113, 162

Calzetti D., 2013, in Falcón-Barroso J., Knapen J. H., eds, , Secular Evolution of Galaxies. p. 419, doi:10.48550/arXiv.1208.2997

Calzetti D., Armus L., Bohlin R. C., Kinney A. L., Koornneef J., Storchi-Bergmann T., 2000, ApJ, 533, 682

Capak P. L., et al., 2011, Nature, 470, 233

Capak P. L., et al., 2015, Nature, 522, 455

Cappellari M., et al., 2007, MNRAS, 379, 418

Carilli C. L., Walter F., 2013, ARAA, 51, 105

Carniani S., et al., 2020, MNRAS, 499, 5136

Casey C. M., et al., 2012, ApJ, 761, 140

Casey C. M., et al., 2013, MNRAS, 436, 1919

Casey C. M., Narayanan D., Cooray A., 2014, Phys. Rep., 541, 45

Chapman S. C., Blain A., Ibata R., Ivison R. J., Smail I., Morrison G., 2009, ApJ, 691, 560

Chary R., Elbaz D., 2001, ApJ, 556, 562

Chen C.-C., et al., 2015, ApJ, 799, 194

Chen C.-C., et al., 2016, ApJ, 820, 82

Clements D. L., Baker A. C., 1996, A&A, 314, L5

Cole S., Lacey C. G., Baugh C. M., Frenk C. S., 2000, MNRAS, 319, 168

Conroy C., 2013, ARAA, 51, 393

Conroy C., Gunn J. E., White M., 2009, ApJ, 699, 486

Conselice C. J., 2014, ARAA, 52, 291

Conselice C. J., Rajgor S., Myers R., 2008, MNRAS, 386, 909

Cooke E. A., et al., 2018, ApJ, 861, 100

Cooray A., Sheth R., 2002, Phys. Rep., 372, 1

Cowley W. I., Lacey C. G., Baugh C. M., Cole S., 2015, MNRAS, 446, 1784

Cox T. J., Jonsson P., Primack J. R., Somerville R. S., 2006, MNRAS, 373, 1013

Cox T. J., Jonsson P., Somerville R. S., Primack J. R., Dekel A., 2008, MNRAS, 384, 386

Crespo Gómez A., et al., 2024, arXiv e-prints, p. arXiv:2402.18672

Croton D. J., et al., 2006, MNRAS, 365, 11

Cui J., Gu Q., Shi Y., 2024, MNRAS, 528, 2391

Cunningham D. J. M., et al., 2020, MNRAS, 494, 4090

Daddi E., et al., 2007, ApJ, 670, 156

Daddi E., et al., 2009, ApJ, 694, 1517

Dale D. A., Helou G., 2002, ApJ, 576, 159

Dasyra K. M., et al., 2006, ApJ, 651, 835

Davé R., Finlator K., Oppenheimer B. D., Fardal M., Katz N., Kereš D., Weinberg D. H., 2010, MNRAS, 404, 1355

Davé R., Anglés-Alcázar D., Narayanan D., Li Q., Rafieferantsoa M. H., Appleby S., 2019, MNRAS, 486, 2827

De Looze I., et al., 2014, A&A, 568, A62

Decarli R., et al., 2014, ApJ, 782, L17

Dekel A., Sari R., Ceverino D., 2009, ApJ, 703, 785

Dessauges-Zavadsky M., et al., 2020, A&A, 643, A5

Díaz-Santos T., et al., 2016, ApJ, 816, L6

Díaz-Santos T., et al., 2017, ApJ, 846, 32

Dole H., et al., 2006, A&A, 451, 417

Downes D., Solomon P. M., 1998, ApJ, 507, 615

Drory N., et al., 2015, AJ, 149, 77

Dudzevičiūtė U., et al., 2020, MNRAS, 494, 3828

Dunne L., Eales S., Edmunds M., Ivison R., Alexander P., Clements D. L., 2000, MNRAS, 315, 115

Engel H., et al., 2010, ApJ, 724, 233

Espino-Briones N., Pérez-González P. G., Zamorano J., Rodríguez-Muñoz L., 2022, MNRAS, 513, 1175

Faber S. M., et al., 2007, ApJ, 665, 265

Farrah D., et al., 2001, MNRAS, 326, 1333

Farrah D., et al., 2013, ApJ, 776, 38

Freedman W. L., et al., 2001, ApJ, 553, 47

Fudamoto Y., et al., 2022, ApJ, 934, 144

Fujimoto S., et al., 2024, ApJ, 964, 146

Gallego J., Zamorano J., Aragon-Salamanca A., Rego M., 1995, ApJ, 455, L1

García-Vergara C., Hodge J., Hennawi J. F., Weiss A., Wardlow J., Myers A. D., Hickox R., 2020, ApJ, 904, 2

Geach J. E., et al., 2017, MNRAS, 465, 1789

Genzel R., et al., 2017, Nature, 543, 397

Gillman S., et al., 2023, A&A, 676, A26

Glazebrook K., et al., 2017, Nature, 544, 71

Gnedin O. Y., 2003, ApJ, 582, 141

Goldsmith P. F., 2019, ApJ, 887, 54

González Delgado R. M., et al., 2016, A&A, 590, A44

Graciá-Carpio J., et al., 2011, ApJ, 728, L7

Granato G. L., De Zotti G., Silva L., Bressan A., Danese L., 2004, ApJ, 600, 580

Gruppioni C., et al., 2020, A&A, 643, A8

Gullberg B., et al., 2018, ApJ, 859, 12

Gullberg B., et al., 2019, MNRAS, 490, 4956

Guth A. H., 1981, Phys. Rev. D, 23, 347

Harikane Y., et al., 2020, ApJ, 896, 93

Harrison C. M., et al., 2016, MNRAS, 456, 1195

Hashimoto T., et al., 2019, PASJ, 71, 71

Hayward C. C., Kereš D., Jonsson P., Narayanan D., Cox T. J., Hernquist L., 2011, ApJ, 743, 159

Hayward C. C., Narayanan D., Kereš D., Jonsson P., Hopkins P. F., Cox T. J., Hernquist L., 2013, MNRAS, 428, 2529

Hayward C. C., et al., 2018, MNRAS, 476, 2278

Hayward C. C., et al., 2021, MNRAS, 502, 2922

Heckman T. M., Armus L., Miley G. K., 1990, ApJS, 74, 833

Hemmati S., Yan L., Diaz-Santos T., Armus L., Capak P., Faisst A., Masters D., 2017, ApJ, 834, 36

Hernquist L., Mihos J. C., 1995, ApJ, 448, 41

Herrera-Camus R., et al., 2018, ApJ, 861, 94

Hickox R. C., et al., 2012, MNRAS, 421, 284

Hinshaw G., et al., 2013, ApJS, 208, 19

Hodge J. A., da Cunha E., 2020, Royal Society Open Science, 7, 200556

Hodge J. A., et al., 2013, ApJ, 768, 91

Hodge J. A., et al., 2016, ApJ, 833, 103

Högbom J. A., 1974, A&AS, 15, 417

Hopkins P. F., Hernquist L., Cox T. J., Kereš D., 2008a, ApJS, 175, 356

Hopkins A. M., McClure-Griffiths N. M., Gaensler B. M., 2008b, ApJ, 682, L13

Hopkins P. F., Cox T. J., Hernquist L., Narayanan D., Hayward C. C., Murray N., 2013, MNRAS, 430, 1901

Houston T., Croton D. J., Sinha M., 2023, MNRAS, 522, L11

Hubble E. P., 1926, ApJ, 64, 321

Hubble E., 1929, Proceedings of the National Academy of Science, 15, 168

Hughes D. H., et al., 1998, Nature, 394, 241

Hygate A. P. S., et al., 2023, MNRAS, 524, 1775

Ikeda R., et al., 2024, arXiv e-prints, p. arXiv:2408.03374

Iono D., et al., 2006, ApJ, 645, L97

Ivison R. J., et al., 2016, ApJ, 832, 78

Jenkins A., Frenk C. S., White S. D. M., Colberg J. M., Cole S., Evrard A. E., Couchman H. M. P., Yoshida N., 2001, MNRAS, 321, 372

Jones G. C., et al., 2017, ApJ, 850, 180

Ju M., et al., 2024, Research in Astronomy and Astrophysics, 24, 025008

Karim A., et al., 2011, ApJ, 730, 61

Kaufman M. J., Wolfire M. G., Hollenbach D. J., Luhman M. L., 1999, ApJ, 527, 795

Kennicutt Robert C. J., 1998, ApJ, 498, 541

Kennicutt R. C., Evans N. J., 2012, ARAA, 50, 531

Kereš D., Katz N., Weinberg D. H., Davé R., 2005, MNRAS, 363, 2

Kewley L. J., Geller M. J., Jansen R. A., Dopita M. A., 2002, AJ, 124, 3135

Kimball A. E., Lacy M., Lonsdale C. J., Macquart J. P., 2015, MNRAS, 452, 88

Klaassen P. D., et al., 2020, in Marshall H. K., Spyromilio J., Usuda T., eds, Society of Photo-Optical Instrumentation Engineers (SPIE) Conference Series Vol. 11445, Ground-based and Airborne Telescopes VIII. p. 114452F (arXiv:2011.07974), doi:10.1117/12.2561315

Kormendy J., Ho L. C., 2013, ARAA, 51, 511

Krogager J. K., Zirm A. W., Toft S., Man A., Brammer G., 2014, ApJ, 797, 17

Lacey C., Cole S., 1993, MNRAS, 262, 627

Lagache G., Cousin M., Chatzikos M., 2018, A&A, 609, A130

Langer W. D., Goldsmith P. F., Pineda J. L., 2016, A&A, 590, A43

Le Fèvre O., et al., 2020, A&A, 643, A1

Lemaux B. C., et al., 2014, A&A, 572, A90

Li A., Fraternali F., Marasco A., Trager S. C., Pezzulli G., Mancera Piña P. E., Verheijen M. A. W., 2023, MNRAS, 520, 147

Liang L., et al., 2024, MNRAS, 528, 499

Loiacono F., et al., 2021, A&A, 646, A76

Long A. S., Casey C. M., del P. Lagos C., Lambrides E. L., Zavala J. A., Champagne J., Cooper O. R., Cooray A. R., 2023, ApJ, 953, 11

Lovell M. R., et al., 2018, MNRAS, 481, 1950

Lower S., Narayanan D., Hu C.-Y., Privon G. C., 2024, ApJ, 965, 123

Lu N., et al., 2017, ApJ, 842, L16

Luhman M. L., Satyapal S., Fischer J., Wolfire M. G., Sturm E., Dudley C. C., Lutz D., Genzel R., 2003, ApJ, 594, 758

Madau P., Dickinson M., 2014, ARAA, 52, 415

Madau P., Pozzetti L., Dickinson M., 1998, ApJ, 498, 106

Magnelli B., et al., 2013, A&A, 553, A132

Maiolino R., et al., 2015, MNRAS, 452, 54

Malhotra S., et al., 1997, ApJ, 491, L27

Malhotra S., et al., 2001, ApJ, 561, 766

Mancini M., Schneider R., Graziani L., Valiante R., Dayal P., Maio U., Ciardi B., 2016, MNRAS, 462, 3130

Martig M., Bournaud F., Teyssier R., Dekel A., 2009, ApJ, 707, 250

McAlpine S., et al., 2019, MNRAS, 488, 2440

McMullin J. P., Waters B., Schiebel D., Young W., Golap K., 2007, in Shaw R. A., Hill F., Bell D. J., eds, Astronomical Society of the Pacific Conference Series Vol. 376, Astronomical Data Analysis Software and Systems XVI. p. 127

Melso N., Bryan G. L., Li M., 2019, ApJ, 872, 47

Meurer G. R., Heckman T. M., Leitherer C., Kinney A., Robert C., Garnett D. R., 1995, AJ, 110, 2665

Millard J. S., Diemer B., Eales S. A., Gomez H. L., Beeston R., Smith M. W. L., 2021, MNRAS, 500, 871

Mitsuhashi I., et al., 2021, ApJ, 907, 122

Mo H. J., Mao S., White S. D. M., 1998, MNRAS, 295, 319

Naab T., Burkert A., 2003, ApJ, 597, 893

Narayanan D., Krumholz M. R., 2017, MNRAS, 467, 50

Navarro J. F., Frenk C. S., White S. D. M., 1996, ApJ, 462, 563

Nesvadba N., et al., 2016, A&A, 593, L2

Neugebauer G., et al., 1984, Science, 224, 14

Ntormousi E., Burkert A., Fierlinger K., Heitsch F., 2011, ApJ, 731, 13

Oberst T. E., et al., 2006, ApJ, 652, L125

Ono Y., et al., 2023, ApJ, 951, 72

Oteo I., et al., 2018, ApJ, 856, 72

Papadopoulos P., Dunne L., Maddox S., 2022, MNRAS, 510, 725

Pavesi R., Riechers D. A., Faisst A. L., Stacey G. J., Capak P. L., 2019, ApJ, 882, 168

Pensabene A., et al., 2021, A&A, 652, A66

Perez J., Valenzuela O., Tissera P. B., Michel-Dansac L., 2013, MNRAS, 436, 259

Perlmutter S., et al., 1999, ApJ, 517, 565

Perrotta S., et al., 2023, ApJ, 949, 9

Peschken N., Łokas E. L., 2019, MNRAS, 483, 2721

Planck Collaboration et al., 2020, A&A, 641, A6

Polletta M., et al., 2024, arXiv e-prints, p. arXiv:2405.07986

Popping G., van Kampen E., Decarli R., Spaans M., Somerville R. S., Trager S. C., 2016, MNRAS, 461, 93

Popping G., et al., 2017, A&A, 602, A11

Popping G., Narayanan D., Somerville R. S., Faisst A. L., Krumholz M. R., 2019, MNRAS, 482, 4906

Price S. H., et al., 2016, ApJ, 819, 80

Psychogyios A., et al., 2016, A&A, 591, A1

Puglisi A., et al., 2019, ApJ, 877, L23

Rafieferantsoa M., Davé R., Anglés-Alcázar D., Katz N., Kollmeier J. A., Oppenheimer B. D., 2015, MNRAS, 453, 3980

Ramasawmy J., et al., 2022, in Zmuidzinas J., Gao J.-R., eds, Society of Photo-Optical Instrumentation Engineers (SPIE) Conference Series Vol. 12190, Millimeter, Submillimeter, and Far-Infrared Detectors and Instrumentation for Astronomy XI. p. 1219007 (arXiv:2207.03914), doi:10.1117/12.2627505

Ramos Padilla A. F., Wang L., van der Tak F. F. S., Trager S. C., 2023, A&A, 679, A131

Rawle T. D., et al., 2014, ApJ, 783, 59

Reuter C., et al., 2020, ApJ, 902, 78

Riess A. G., et al., 1998, AJ, 116, 1009

Rizzo F., Vegetti S., Fraternali F., Stacey H. R., Powell D., 2021, MNRAS, 507, 3952

Rodighiero G., et al., 2011, ApJ, 739, L40

Rybak M., et al., 2019, ApJ, 876, 112

Sakamoto K., Okumura S. K., Ishizuki S., Scoville N. Z., 1999, ApJ, 525, 691

Salvador D., Cerulo P., Valenzuela K., Demarco R., Oyarzo F., Gatica C., 2024, A&A, 684, A166

Sánchez S. F., et al., 2014, A&A, 563, A49

Sanders D. B., Mirabel I. F., 1996, ARAA, 34, 749

Santini P., et al., 2009, A&A, 504, 751

Savage B. D., Sembach K. R., 1996, ApJ, 470, 893

Schaerer D., et al., 2020, A&A, 643, A3

Schaye J., et al., 2010, MNRAS, 402, 1536

Schechter P., 1976, ApJ, 203, 297

Schreiber C., et al., 2021, A&A, 646, A68

Scoville N., et al., 2016, ApJ, 820, 83

Shen X., Vogelsberger M., Nelson D., Tacchella S., Hernquist L., Springel V., Marinacci F., Torrey P., 2022, MNRAS, 510, 5560

Sherman S., et al., 2020, MNRAS, 499, 4239

Shibuya T., et al., 2024, arXiv e-prints, p. arXiv:2403.06729

Simpson J. M., et al., 2014, ApJ, 788, 125

Simpson J. M., et al., 2015, ApJ, 799, 81

Smail I., Ivison R. J., Blain A. W., 1997, ApJ, 490, L5

Smit R., et al., 2018, Nature, 553, 178

Smith J. D. T., et al., 2017, ApJ, 834, 5

Smith R. J., Collier W. P., Ozaki S., Lucey J. R., 2020, MNRAS, 493, L33

Smolčić V., et al., 2015, A&A, 576, A127

Sobral D., Best P. N., Smail I., Mobasher B., Stott J., Nisbet D., 2014, MNRAS, 437, 3516

Soifer B. T., Neugebauer G., Houck J. R., 1987, ARAA, 25, 187

Speagle J. S., Steinhardt C. L., Capak P. L., Silverman J. D., 2014, ApJS, 214, 15

Springel V., et al., 2005, Nature, 435, 629

Stacey G. J., Geis N., Genzel R., Lugten J. B., Poglitsch A., Sternberg A., Townes C. H., 1991, ApJ, 373, 423

Stach S. M., et al., 2019, MNRAS, 487, 4648

Stach S. M., et al., 2021, MNRAS, 504, 172

Stockmann M., et al., 2021, ApJ, 908, 135

Stott J. P., et al., 2016, MNRAS, 457, 1888

Strandet M. L., et al., 2017, ApJ, 842, L15

Sturm E., Genzel R., Lutz D., Rigopoulou D., Tran D., Dannerbauer H., Moorwood A. F. M., Spoon H. W. W., 1999, Ap&SS, 269, 399

Sugahara Y., et al., 2024, arXiv e-prints, p. arXiv:2403.17133

Surace J. A., Sanders D. B., Evans A. S., 2001, AJ, 122, 2791

Sutter J., et al., 2019, ApJ, 886, 60

Swinbank A. M., et al., 2012, MNRAS, 427, 1066

Swinbank A. M., et al., 2014, MNRAS, 438, 1267

Tacconi L. J., et al., 2013, ApJ, 768, 74

Tanaka M., et al., 2019, ApJ, 885, L34

Thomas D., Maraston C., Bender R., Mendes de Oliveira C., 2005, ApJ, 621, 673

Toft S., et al., 2014, ApJ, 782, 68

Traina A., et al., 2024, A&A, 681, A118

Uematsu R., et al., 2024, arXiv e-prints, p. arXiv:2402.05849

Umehata H., et al., 2017, ApJ, 834, L16

Valentino F., et al., 2020, ApJ, 889, 93

Veilleux S., Kim D. C., Sanders D. B., 2002, ApJS, 143, 315

Venemans B. P., et al., 2017, ApJ, 851, L8

Vizgan D., et al., 2022, ApJ, 929, 92

Vogelsberger M., et al., 2014, MNRAS, 444, 1518

Wake D. A., et al., 2017, AJ, 154, 86

Walter F., et al., 2012, Nature, 486, 233

Walter F., et al., 2020, ApJ, 902, 111

Wang R., et al., 2013a, ApJ, 773, 44

Wang S. X., et al., 2013b, ApJ, 778, 179

Wardlow J. L., et al., 2011, MNRAS, 415, 1479

Weiß A., et al., 2009, ApJ, 707, 1201

White S. D. M., Frenk C. S., 1991, ApJ, 379, 52

White S. D. M., Rees M. J., 1978, MNRAS, 183, 341

Willett K. W., et al., 2017, MNRAS, 464, 4176

Williams R. J., Quadri R. F., Franx M., van Dokkum P., Labbé I., 2009, ApJ, 691, 1879

Wolfire M. G., Tielens A. G. G. M., Hollenbach D., 1990, ApJ, 358, 116

Wolfire M. G., Vallini L., Chevance M., 2022, ARAA, 60, 247

Wuyts S., et al., 2011, ApJ, 742, 96

Wuyts S., et al., 2016, ApJ, 831, 149

Xie L., et al., 2024, ApJ, 966, L2

Yan R., et al., 2016, AJ, 152, 197

Yan L., et al., 2020, ApJ, 905, 147

Yang S., Popping G., Somerville R. S., Pullen A. R., Breysse P. C., Maniyar A. S., 2022, ApJ, 929, 140

Yoon Y., Park C., Chung H., Zhang K., 2021, ApJ, 922, 249

Younger J. D., et al., 2008, ApJ, 688, 59

Zavala J. A., et al., 2017, MNRAS, 464, 3369

Zavala J. A., et al., 2018, Nature Astronomy, 2, 56

Zavala J. A., et al., 2021, ApJ, 909, 165

Zhang Z.-Y., et al., 2018, MNRAS, 481, 59

da Cunha E., et al., 2015, ApJ, 806, 110

van Dokkum P. G., et al., 2015, ApJ, 813, 23